Proceedings of the Department of Civil and Structural Engineering
University of Sheffield, UK

The Annual Postgraduate Research Student Conference - 2015

Edited by Harm Askes, Matthew Gilbert and Luca Susmel

The
University
Of
Sheffield.

ESIS

Table of Contents

Foreword

The ten papers which appear in this proceedings were contributed by current research students studying in the Department of Civil & Structural Engineering at the University of Sheffield. The papers which have been included provide a flavour of the breadth of the research currently being undertaken in the Department.

The Department has a long history of undertaking research in the field of structural engineering and mechanics, and the area is represented in the proceedings by five papers. Two of the contributions focus on cold-formed steel sections, popular in the U.S. for many years and now attracting increasing interest in Europe, whilst a further two contributions consider the seismic response of structures. The final contribution in the area appraises the efficacy of a sophisticated constitutive model used to predict fatigue damage when complex loading regimes are involved.

The Department is also strong in the fields of water engineering and fluid mechanics, with recent staff appointments further enhancing our capability in these areas. The proceedings include a paper on green roofs (which can contribute to biodiversity and stormwater management) and a paper on the flow patterns and mixing processes in vegetated ponds.

For many years the Department has had significant expertise in the field of geotechnical engineering. One paper in this field considers the potential for the piled foundations used to support buildings to be used as heat exchangers, to reduce energy use, whilst a further paper focuses on numerical modelling of the experimental apparatus used to establish the dynamic characteristics of sand.

The Department is now also active in the area of building simulation, and a paper in the proceedings considers the use of a data driven, neural network based, approach to predicting temperature in naturally ventilated buildings.

Producing the present volume of papers marks a positive new development for the Department. We are confident that the research students involved will have benefited from the experience of writing up their work in the form of a conference paper, and sincerely hope that this volume will be the first of many.

Lastly, we would like to express our heartfelt gratitude to the European Structural Integrity Society (http://www.structuralintegrity.eu) and to the Italian Group of Fracture (www.gruppofrattura.it) for supporting the publication of these proceedings.

Harm Askes
Head of Department

Matthew Gilbert
Director of Research

Luca Susmel
Postgraduate Research Tutor

Sheffield, 31 March 2015

Cold-formed steel channel beams:
From optimal design to development of a novel section

Jun Ye, Iman Hajirasouliha, Jurgen Becque
University of Sheffield
jye2@sheffield.ac.uk, i.hajirasouliha@sheffield.ac.uk, j.becque@sheffield.ac.uk

Primary Supervisor:	Dr **I. Hajirasouliha** – e-mail: i.hajirasouliha@sheffield.ac.uk
Secondary Supervisor:	Dr **J. Becque** – e-mail: j.becque@sheffield.ac.uk

ABSTRACT. Optimal design of cold-formed steel (CFS) cross-sections can significantly increase their ultimate load carrying capacity leading to a more economical and efficient structural system. This paper reports on the result of an investigation on optimisation of CFS channel beams subjected to their bending capacity. The optimisation was aimed at maximize strength complying with the manufacturing and constructional restraints. As a result, the selected prototypes and optimisation process met the requirements suggested in Eurocode 3 (EC3). In total, ten CFS channel cross-sections including one novel channel section with the folded flange were considered in the optimisation process. The cross-sectional properties and flexural strength of the sections were determined based on the effective width method suggested in EC3, while the optimisation process was performed using particle swarm optimisation method. The flexural strength of the optimised sections were also obtained using the nonlinear finite element (FE) analysis and the results were compared with those of effective width method suggested in EC3. For the newly-developed folded-flange section, it was observed that the suggested model can predict the bending capacity with reliable accuracy. In addition, compared to their commonly-used standard counterpart and other optimised cross-sections with the same material, this new prototype possesses the highest bending capacity. The bending capacity can also be significantly enhanced by adding edge stiffeners while the effect of incorporating the intermediate stiffeners is negligible and even negative in some cases.

INTRODUCTION

The flexibility of profile shapes allows more choices for designers. However, CFS members are inherently vulnerable to the multitude buckling behaviours which make the design procedure complex and time-consuming. Recent experimental and analytical research [1] has demonstrated that increasing the number of flange bends in CFS channel sections can enhance both the elastic and inelastic behavior. Consequently, the highest strength, stiffness, and ductility were observed in beams with an infinite number of bends (curved flanges) as shown in Fig. 1(a). Nevertheless, this type of cross-section is hard to manufacture and difficult to connect with floor systems. By considering the construction and manufacture restraints, the curved flange can be substituted with a folded flange as shown in Fig. 1(b). This folded flange section along with nine other conventional channel sections were considered as the prototypes in the current study. A constant total coil width and thickness were considered for all section during the optimisation process. The flexural properties of the sections were determined in accordance to the Effective Width Method suggested in EC3 [2]. The optimised solutions were arrived using Particle Swarm Optimisation (PSO) Algorithm [3].
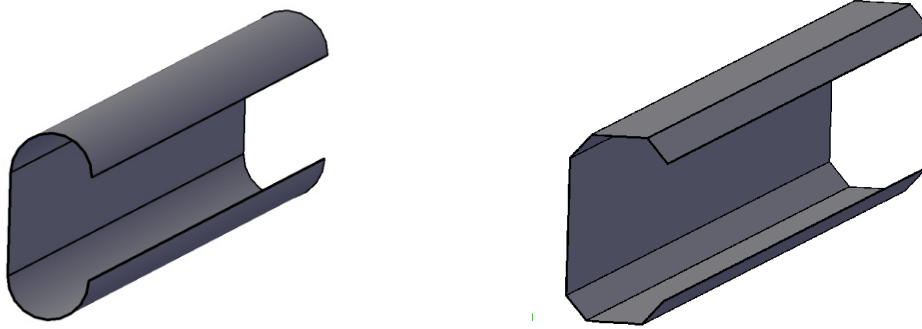
Figure 1. CFS channel sections with curved flange and folded flange.

DESIGN OF CFS MEMBERS BASED ON EC3

The optimal design of the selected prototypes followed the stability and strength provisions suggested based on the Effective Width Method in EC3. EC3 uses the notional flat width of the plate assemblies to determine the cross-sectional properties and these properties are reduced by a factor (δ) to account for the round corner effects.

Design for local buckling

In EC3, the effect of local buckling is considered through the effective width concept, first proposed by Von Karman [4]. It recognizes the fact that local buckling of the plates constituting the cross-section has the effect of shifting the load-bearing stresses towards the corner zones, while the central parts of the plates become less effective in carrying load. This effective area is assumed to carry the full compressive load applied to the section. According to EC3, the effective width of a plate is given by

$$\frac{b_e}{b} = \frac{1}{\lambda_l}\left(1 - \frac{0.055(3+\psi)}{\lambda_l}\right) \tag{1}$$

where b and b_e are the total and the effective width of the plate, respectively. Also, the slenderness against local buckling, $\lambda_l = \sqrt{f_y / \sigma_{cr}}$, relates to the material yield stress, f_y, and the elastic local buckling stress of the plate, σ_{cr}. ψ is the stress ratio of the plates.

Design for Distortional buckling

In EC3, the design of distortional buckling is based on the assumption that the stiffeners of compressive flange behave as a strut with springs along the centroid axis. The elastic critical buckling stress for stiffened elements is then defined by

$$\sigma_{cr,s} = \frac{2\sqrt{KEI_s}}{A_s} \tag{2}$$

where $\sigma_{cr,s}$ is the elastic critical buckling stress, E is the modulus of elasticity, I_s is the second moment of the effective area of the stiffener about the axis parallel to flange, K is the spring stiffness per unit length, and A_s is the effective area of the edge stiffener. For the folded flange cross-section, two distortional buckling modes are probable depending on the length of flange parts. As demonstrated Figs. 2(a) and 2(b), where the length of flange 2 is relatively larger than flange 1, buckling of sub-assembly of flange 2 and lip may occur, while the second buckling modes will be expected when flange 1 is much longer than flange 2. The deflections δ_1 and δ_2 produced by concentrated forces u_1 and u_2, respectively, are defined by

$$\delta_1 = \frac{u_1}{3D}\left[e^3 + e^2 b + b(e - b\cos\theta_1)(2e - b\cos\theta_1) + \frac{3}{2}b(e - b\cos\theta_1)^2\right] \tag{3}$$

$$\delta_2 = \frac{u_2}{3D}\left[e^3 + \frac{3}{2}he^2\right] \tag{4}$$

where the bending rigidity of the plate $D = Et^3/12(1-v^2)$, e is the distance between the gravity centre of the edge stiffener to the web-to-flange junction, h is the height of web, b is the length of flange 1 and θ_1 is the angle between flange 1 and flange 2, as shown in Figs. 2, t is the thickness, E and v are the modulus of elasticity and Poisson's ratio, respectively. The distortional buckling is taken into account by using a reduced thickness at the stiffeners.
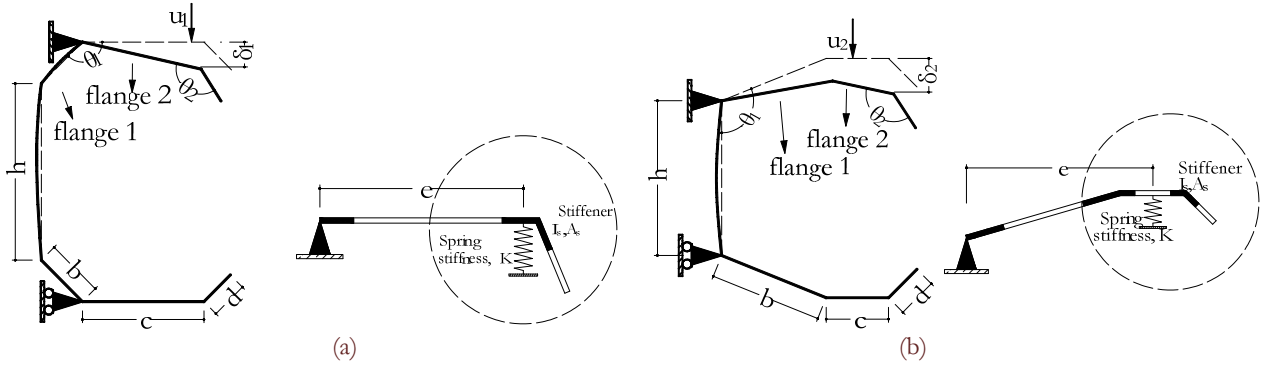

Figure. 2: Analytical model (a) to analyse distortional buckling-type 1 and (b) to analyse distortional buckling-type 2.

OPTIMISATION PROCEDURE

Problem definition

The optimisation procedure was aimed at optimising the each CFS cross-section with regard to its bending capacity. In order to take the manufacturing and construction issues into consideration, the optimal design formulation of CFS beams was derived based on the provisions suggested in EC3. In total, 10 different prototypes, including 9 prototypes predefined by EC3 and the newly-developed folded flange channel section were considered with the same thickness of $t = 1.5\ mm$ and total coil width of $l = 415\ mm$. Since the beams are always laterally supported by the floor system, only local/distortional buckling are considered in the optimisation process. Tab. 1 shows the selected prototypes along with the design variables and optimisation constraints. The yield strength of the CFS plate was considered to be $f_y = 450\ MPa$.

In the optimisation process, the length of intermediate stiffeners is 10 mm and the angle between the intermediate stiffeners is set to be 60°. The optimisation problem can be formulated as a minimization problem defined by

$$\min\ f(x) = -W_{eff}f_y/\gamma_{M_0} \qquad u_{\min} \le x_i \le u_{\max} \quad \text{for } i = 1, \cdots, N \tag{6}$$

where $f(x)$ is the design moment resistance of a cross-section about the major axis and . W_{eff} is the effective section modulus which can be calculated based on the effective width of plates and the reduced thickness for distortional buckling. Also, γ_{M_0} is the partial factor of ultimate limit state. It is worth mentioning that the inelastic reserve capacity is always taken into account according to EC3. For each variable x_i, the lower and upper bounds, $u_{\min}$ and $u_{\max}$, respectively, are considered according to EC3 and summarised in Tab. 2.

Optimisation solutions

The optimisation procedures were formulated in Matlab software [5] using the Particle Swarm Optimisation Algorithm. The population of particle swam was taken as 100, and the same number was also used for iterations to obtain the optimum value. For optimisation, each of the prototypes was run for 3 times and the result with maximum bending capacity was chosen as the optimum section. Tab. 2 summarise the geometrical details and bending capacity of the optimised cross-sections and Tab. 3 listed all the effective cross-sections of the optimised prototypes from Matlab which are drawn at the same scale.
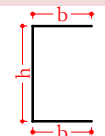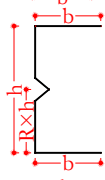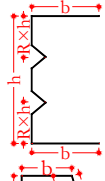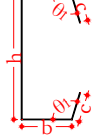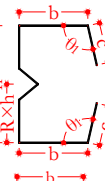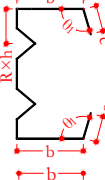
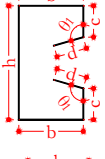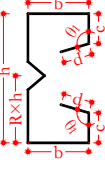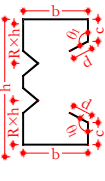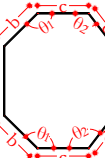| Prototype	Prototype section	Design variables	Constraints based on EC3	Comments
①		$x=b/l$	$b/t\leq50$ $h/t\leq500$	EN1993-1-3 Clause 5.2
②		$x_1=b/l$ $x_2=R$	$b/t\leq50$ $h/t\leq500$ $0.1\leq R\leq0.9$	EN1993-1-3 Clause 5.2
③		$x_1=b/l$ $x_2=R$	$b/t\leq50$ $h/t\leq500$ $0.1\leq R\leq0.9$	EN1993-1-3 Clause 5.2
④		$x_1=c/b$ $x_2=b/l$ $x_3=\theta_1$	$0.2\leq c/b\leq0.6$ $b/t\leq60$ $c/t\leq50$ $h/t\leq500$ $\pi/4\leq\theta_1\leq3/4\pi$	EN1993-1-3 Clause 5.2
⑤		$x_1=c/b$ $x_2=b/l$ $x_3=R$ $x_4=\theta_1$	$0.2\leq c/b\leq0.6$ $b/t\leq60$ $c/t\leq50$ $h/t\leq500$ $\pi/4\leq\theta_1\leq3/4\pi$ $0.1\leq R\leq0.9$	EN1993-1-3 Clause 5.2
⑥		$x_1=c/b$ $x_2=b/l$ $x_3=R$ $x_4=\theta_1$	$0.2\leq c/b\leq0.6$ $b/t\leq60$ $c/t\leq50$ $h/t\leq500$ $\pi/4\leq\theta_1\leq3/4\pi$ $0.1\leq R\leq0.4$	EN1993-1-3 Clause 5.2
⑦		$x_1=c/b$ $x_2=d/b$ $x_3=b/l$ $x_4=\theta_1$	$0.2\leq c/b\leq0.6$ $0.1\leq d/b\leq0.3$ $b/t\leq90$ $c/t\leq60\ d/t\leq50$ $h/t\leq500$ $\pi/4\leq\theta_1\leq3/4\pi$	EN1993-1-3 Clause 5.2
⑧		$x_1=c/b$ $x_2=d/b$ $x_3=b/l$ $x_4=R$ $x_5=\theta_1$	$0.2\leq c/b\leq0.6$ $0.1\leq d/b\leq0.3$ $b/t\leq90$ $c/t\leq60\ d/t\leq50$ $h/t\leq500$ $\pi/4\leq\theta_1\leq3/4\pi$ $0.1\leq R\leq0.9$	EN1993-1-3 Clause 5.2
⑨		$x_1=c/b$ $x_2=d/b$ $x_3=b/l$ $x_4=R$ $x_5=\theta_1$	$0.2\leq c/b\leq0.6$ $0.1\leq d/b\leq0.3$ $b/t\leq90$ $c/t\leq60\ d/t\leq50$ $h/t\leq500$ $\pi/4\leq\theta_1\leq3/4\pi$ $0.1\leq R\leq0.4$	EN1993-1-3 Clause 5.2
⑩		$x_1=\theta_1$ $x_2=\theta_2$ $x_3=b$ $x_4=c$ $x_5=d$	$h/t\leq500$ $7/12\pi\leq\theta_1\leq5/6\pi$ $\pi/4\leq\theta_2\leq3/4\pi$ $30\leq b\leq48$ $50\leq c\leq60$ $15\leq d\leq60$	Newly developed shape

Table 1: Selected prototypes, design variables and constraints.

It is clearly from Tab. 3 that all the cross-sections have the high height-to-width ratio. While the bending moments of the cross-sections are mainly determined by the effective portions of the plate assemblies and the web height, prototype 1-3 are still with low relatively bending strength though they have the biggest height. This is due to the fact that the flanges without edge stiffeners are susceptible to local buckling though the strength is slightly enhanced by adding intermediate stiffeners to the web. Comparing prototype 4 with prototypes 5 and 6 in Tab. 2 and 3 indicates that the introduction of edge stiffeners can significantly improve the bending capacities while it is not significant for the case of intermediate stiffeners. This is due to the fact: 1. the stiffeners are prone to distortional buckling with the high web dimension, leading to the loss of thickness of the intermediate stiffeners (as shown in Tab. 2), and 2. The folding of the intermediate stiffeners causes reduction of the height which is important to the effective sectional modulus.

Section	h (mm)	b (mm)	c (mm)	d (mm)	θ_1 (rad)	θ_2 (rad)	R	Capacity (kN·m)
①	315	50	-	-	-	-	-	9.84
②	305	50	-	-	-	-	0.856	11.08
③	295	50				-	0.186	9.92
④	269.8	50	22.6	-	1.579	-	-	13.38
⑤	263	50	21	-	1.61	-	0.79	13.66
⑥	234.4	50	20.3	-	1.576	-	0.223	12.69
⑦	242	50	29.3	7.2	1.574	-	-	15.11
⑧	240.6	50	25.3	6.9	2.356	-	0.9	14.62
⑨	231.8	50	25.2	6.4	2.356	-	0.1	13.41
⑩	184.6	48	50	17.2	1.83	1.66	-	16.12

Table 2: Geometrical details and bending capacities of the optimised sections.
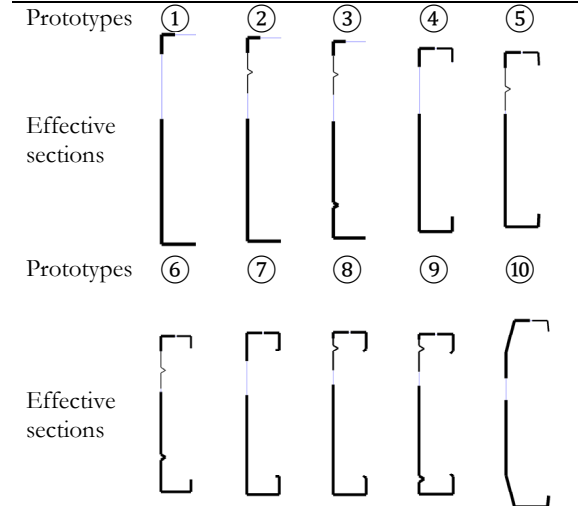
Table 3: Effective cross-sections of the beams.

Section	FE length (mm)	Bending moment (kN·m)		EC3/FE
		EC3	FEM	
Standard	1800	10.3	10.4	0.99
①	600	9.84	9.11	1.08
②	600	11.08	11.22	0.99
③	600	9.92	9.41	1.05
④	1800	13.38	12.73	1.05
⑤	1800	13.66	12.08	1.13
⑥	1800	12.69	11.15	1.14
⑦	2400	15.11	14.09	1.07
⑧	2400	14.62	12.99	1.13
⑨	2400	13.41	12.33	1.09
⑩	2400	16.12	15.52	1.04

Table 4: Comparison of the bending moment capacities of the optimised and standard sections obtained from EC3
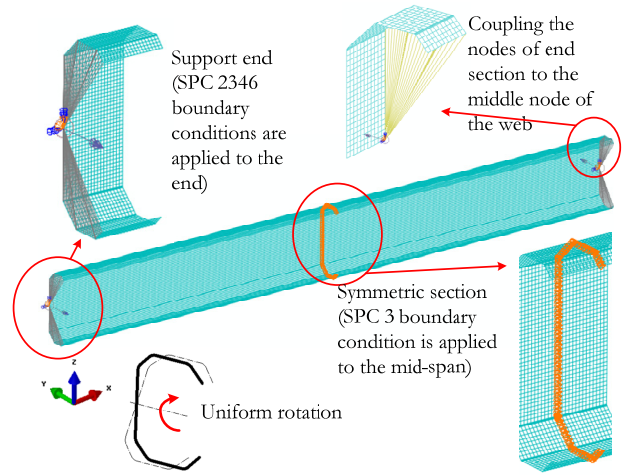
Figure 3: FE analysis and FE models of the beams subjected to local/distortional buckling.

NONLINEAR FE RESULTS OF THE STANDARD AND OPTIMISED CROSS-SECTIONS

The bending moment capacities of the optimised and standard cross-sections were also obtained using the nonlinear FE analysis with ABAQUS [6] and the results were compared with those determined according to the effective width method suggested in EC3. The adopted boundary conditions, material properties and imperfections were the same as the FE models in reference [7-9], accordingly and the load was applied in the form of

uniform rotations at both ends with a displacement control regime, as shown in Fig. 3. Also, the length of the beam models were selected as three times of distortional buckling half-wave length, as shown in Tab. 4. The FE modelling has been verified through the experimental results from [10, 11], good agreement has been achieved where the average error is around 10%.

Tab. 4 compares the bending capacities of the optimal and standard cross-sections obtained from the FE analysis with those determined based on the effective width method suggested in EC3. Despite that the results obtained from EC3 are unconservative compared to the FE bending capacities, it can be concluded that the Effective Width Method suggested in EC3 provides a reasonable prediction for bending moment capacities.

COMPARISON OF THE RESULTS AND DISCUSSION

Fig. 4 compares the bending moment capacities of optimised sections with that of the standard section. As observed in the prototypes, the following conclusions can be drawn:

- The newly-developed folded-flange section offers the highest bending moment capacity with 57% increase compared to the standard section.
- Adding edge stiffeners can result in a significant increase in the bending moment capacity of the section with a fix total coil width. This can be due to the effect of the edge stiffeners in preventing the distortional failure modes by increasing the elastic critical stress and the less reduction of the thickness.
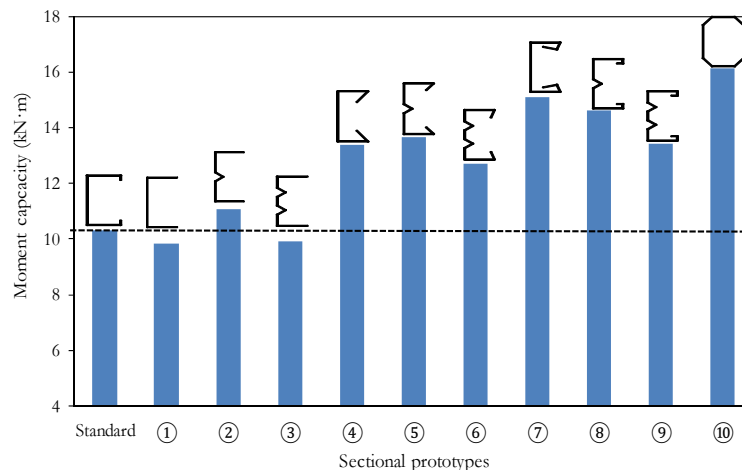
Figure 4: Comparison of the moment capacity of prototypes

- Providing intermediate stiffeners in the web cannot essentially increase the optimal bending capacity. Although, intermediate stiffeners can significantly increase the effective width of the web, it reduces the total height of the cross-section with constant coil length which may cause a decrease in the effective sectional modulus.
- The plain channel cross-sections cannot be considered as effective and economical cross-section in term of bending capacity.

REFERENCES

[1] Sabbagh, A.B., Petkovski, M., Pilakoutas K., Mirghaderi R., Ductile moment-resisting frames using cold-formed steel sections: An analytical investigation. J. Constr. Steel. Res., 67(2011) 634-646.

[2] Eurocode 3: design of steel structures: Part 1.1: General rules and rules for buildings. EN 1993-1-1; (2005).

[3] Perez, R.E., Behdinan, K., Particle swarm approach for structural design optimisation. Comput Struct., 85(2007)1579-1688.

[4] Von Karman, T., Sechler, E.E., Donnell, L., The strength of thin plates in compression. Trans ASME., 54(1932) 53-57.

[5] Mathworks. Matlab R2011a. Mathworks, Inc; (2011).

[6] ABAQUS. Version 6.7 ed. Pawtucket, USA: Hibbitt, Karlsson & Sorensen, Inc; (2007).

[7] Shifferaw, Y., Schafer, B.W., Inelastic Bending Capacity of Cold-Formed Steel Members. J Struct Eng-ASCE., 138 (2012) 468-480.

[8] Haidarali, M.R., Nethercot, D.A., Finite element modelling of cold-formed steel beams under local buckling or combined local/distortional buckling. Thin Wall Struct., 49 (2011) 1554-62.

[9] Schafer, B.W., Pekoz, T., Computational modeling of cold-formed steel: characterizing geometric imperfections and residual stresses, J Constr Steel Res., 47 (1998) 193-210.

[10] Yu, C., Schafer, B.W., Distortional buckling tests on cold-formed steel beams. J Struct Eng-ASCE, 132 (2006) 515-528.

[11] Yu, C., Schafer, B.W., Local buckling tests on cold-formed steel beams, J Struct Eng-ASCE., 129 (2003) 1596-1606.

Using X-ray microtomography to identify physical changes in green roof substrates as a result of ageing

Simon De-Ville, Manoj Menon, Virginia Stovin

Department of Civil & Structural Engineering, University of Sheffield
sde-ville1@sheffield.ac.uk, m.menon@sheffield.ac.uk, v.stovin@sheffield.ac.uk

Primary Supervisor:	Dr. **V. Stovin** – e-mail: v.stovin@sheffield.ac.uk
Secondary Supervisor:	Dr. **M. Menon** – e-mail: m.menon@sheffield.ac.uk

ABSTRACT. Green roofs are complex engineered structures that can provide significant benefits to biodiversity, the thermal performance of buildings and stormwater management, amongst others. As such, there are guidelines that dictate the composition and properties of green roof substrates to ensure that these benefits can be realised. However, a green roof's position exposes it to several natural processes that may alter the properties of the substrate beyond their allowed limits. There is currently little understanding of the presence and magnitude of changes to substrate properties as a result of influencing processes over time. This paper uses techniques not used before in a green roof context to non-invasively explore the internal structure of two green roof substrates in both aged and virgin forms. Using X-ray microtomography and image processing techniques, particle size distributions and porosity values are determined for selected 2D planes. It is found that the X-ray microtomography technique is a good method to non-destructively assess the properties of green roof substrates. The particle size distribution and porosity of the two substrates was found to be different between the aged and virgin samples. However, the uncertainties surrounding substrate heterogeneity mean these quantitative changes in properties should be considered to be indicative rather than absolute.

KEYWORDS. Green Roof; Substrate; X-Ray Microtomography; Temporal Changes; Porosity.

INTRODUCTION

There are two main active elements of a green roof, the vegetation and the substrate. Both of these elements are subject to a number of processes that have the potential to alter their characterised physical properties over time. On the surface the most visible of these processes is plant growth, and this is relatively straightforward to quantify. However, the subsequent root growth beneath the surface is more difficult to evaluate, as it is not readily visible in its intact form. The substrate may also be subject to organic matter turnover, consolidation and chemical alteration from polluted rainwaters, all of which have the potential to alter the substrates properties. Yet, similarly, observations of such changes are difficult to undertake without destructive sampling.

There is currently a lack of research within the field of green roof ageing [1]. However, existing research has found that the levels of organic matter within a green roof can change with time, and both increases [2] and decreases [3] have been identified. Getter and Rowe [2], who briefly discuss changes in the properties of a mature substrate, found an increase in pore space values from 41 to 82% alongside a 294% increase in water holding capacity. All of these studies used

destructive testing means to determine the substrate properties and so the green roofs were decommissioned in these cases.

Therefore, there is clearly a need to further explore green roof ageing in a way that allows for continued green roof operation to maximise green roof lifespan. X-Ray microtomography (XMT) is an X-Ray imaging technique that allows for the non-destructive characterisation of material properties. Images with high resolutions can be obtained and analysed to show the spatial arrangement of solid particles and pore spaces in a soil-like matrix [4]. XMT is an established technique within the soil science field, where the main application has been for the characterisation of soil physical properties [5]. Other studies have used XMT to examine: plant roots and their interactions with the soils; earthworm burrows; soil insects; and other soil microorganisms. However, there has been no use of XMT to image green roof substrates and assess any property changes as a result of ageing.

Hence, this study has the following objectives:

- to determine the usefulness of non-invasive X-ray microtomography (XMT) in evaluating changes to properties of green roof substrates as a result of ageing;
- to qualitatively describe any observed changes in substrate properties and the impacts upon the substrate's ability to meet its design criteria.

METHODOLOGY

Sample Collection and Preparation

Four substrate cores were prepared for non-invasive analysis. The core holders were 68 mm in height with an internal diameter of 46 mm, these sizes were restricted by the loading gauge of the XMT machine. The core holders were constructed from *Poly(methyl methacrylate)* (PMMA, commercially known as *Perspex*). A non-metallic material is required for the XMT imaging process in order to prevent poor image quality.

Two distinct types of substrate were used to compare the potential changes in properties. One of the substrates is Brick based and was used extensively as part of the 'Marie Curie Green Roof Project' and is referred to as Marie Curie Substrate (MCS). In addition to the crushed brick component, MCS also contains bark and coir (combined 15% by weight). The second substrate mix is based on Light Expanded Clay Aggregate (LECA) (80% by weight) and also includes compost (20% by weight). Both substrates have been characterised previously, LECA by Poë *et al.* [6] and the mineral component of MCS by Yio *et al.* [7].

From each type of substrate, an aged and a virgin core was created. The virgin cores (MCS_V and $LECA_V$) were formed from material that was part of the same batch as that used in two active green roof test beds, the same beds from which the aged cores were taken. The aged MCS core (MCS_A) was taken from the Mappin Test Bed (a full description of the roof configuration can be found in Kasmin *et al.* [8]). The aged LECA core ($LECA_A$) was taken from one of the Hadfield Green Roof Test Beds (a full description of the roof configuration can be found in Beretta *et al.* [9]). Both of the aged substrate cores were also vegetated with mixed *Sedum spp.* vegetation.

X-Ray Microtomography Image Capture and Analysis

For this study the cores were imaged using a *General Electric v|tome|x M* CT scanner at the University of Nottingham's Hounsfield Facility. Each core was scanned at a resolution of 30 μm.

Image analysis was undertaken using the open-source image editor ImageJ [10]. The scan data from each core was divided into three sections each of 740 slices: lower; middle and upper (This was due to computer RAM limitations). A single slice from the centre of each section was taken forward for further analysis, Fig. 1 illustrates the location in the vertical plane where the slices were taken.

Porosity and particle size distribution were both identified using the particle analyser tool in ImageJ. The particle analyser tool identifies individual particles within an image by first locating particle edges, then outlining the remaining particle using the wand tool of ImageJ, the selection is then filled and the area and Feret diameter of this shape is determined. The Feret diameter is the distance between two parallel tangents on opposite sides of the identified particle, and provides an indication of 3D particle diameters when projected onto a 2D plane. These particle diameters were used to construct particle size distributions. Porosity values were determined from the particle areas. The area of the circular core less the particle area indicates a total void area. Filling of intra-pores, the pore spaces within aggregate pieces, using binary image processing, allows for a closed pore area to be determined.

RESULTS AND DISCUSSION

Visual Observations

Fig. 2 shows the physical differences between the compositions of the two substrate mixes, with LECA having a much less dense particle matrix compared to MCS. Closer examination of Fig. 1 and 2 show the aged cores have considerably greater variation in their particle distributions with depth, compared to the virgin pair. The upper regions of both the MCS_A and $LECA_A$ have an increased number of smaller particles. The softer levels of grey within the image (Fig. 2) correspond with areas of organic matter, and show root masses along with entrained organic content. The central region of $LECA_A$ includes some identifiable roots and other organic matter. The central region of MCS_A shows no sign of root activity, which when looking at Fig. 1 is not unexpected due to its denser particle matrix. This increased packing may have prevented the breakthrough of roots to lower levels within the substrate. In the lower region of both substrates there is little evidence of a build up of fines; something that may have been expected. This could potentially be because the analysed horizontal slice is not at the very bottom of the core. Alternatively, the core depth of 68 mm is shallower than the original substrate depth of 80 mm and so the very bottom layer has not been captured as part of the scan.

Characterised Observations

The particle size distributions (PSD) in Fig. 3 show that for MCS_V the PSD is relatively uniform throughout the entire depth. This is to be expected in a newly constructed core. MCS_A has an increased variation between the upper and middle/lower layers compared to the virgin MCS_V. The shift in the upper section PSD indicates that there are more small particles than in either of the other two sections. This is possibly a result of root growth and weathering processes that have caused the larger aggregate pieces to degrade into smaller ones, alongside atmospheric particle deposition and organic matter turnover.
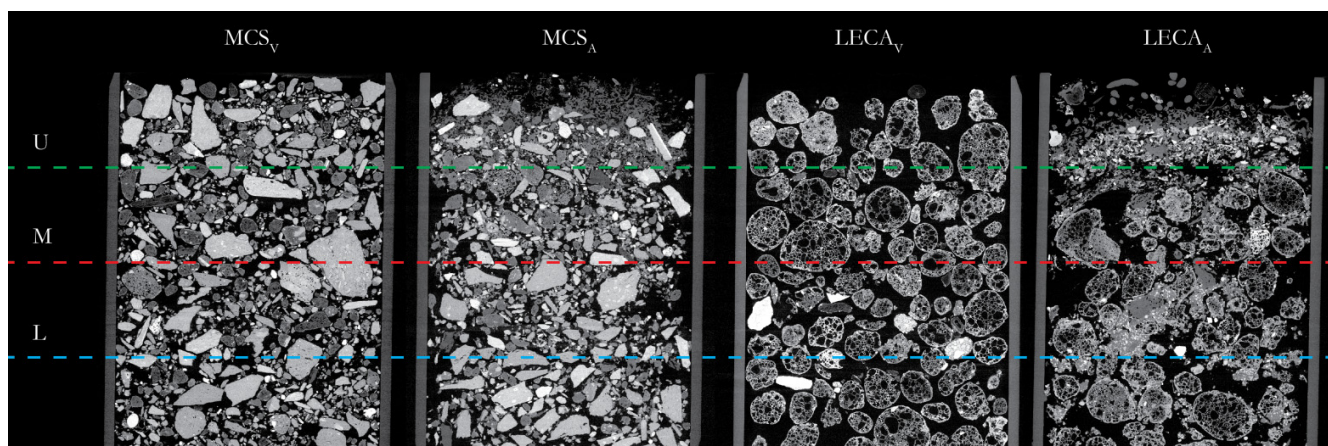

Figure 1: Reconstructed XMT slices in the vertical plane of the four substrate cores. The green line represents the centre of the upper third of the sample (U), the red line represents the centre of the middle third of the sample (M) and the blue line represents the centre of the lower third of the sample (L). Horizontal plane slices at these points can be seen in Fig. 2.

The virgin $LECA_V$ exhibits a large difference in the PSD of its upper and middle layers compared to the lower layer. The increased number of smaller particles in the lower layer would suggest that the core has undergone a degree of granular convection, with the smaller particles making their way to the bottom of the core. $LECA_A$ has a PSD that is more similar to MCS_A, than to $LECA_V$. The upper layer sees a large shift in the PSD from the virgin to aged cores, with $LECA_A$ having considerably more small particles in the upper layer than in either the middle or lower layer. As seen for MCS_A, this could again be a result of aggregate degradation due to root growth and/or weathering.

Both the virgin MCS_V and $LECA_V$ have a more uniform distribution of open, closed and total porosity with depth when compared to their aged counterparts (Fig. 4). The slight differences in porosity between the layers of MCS_V and $LECA_V$ are to be expected, and are more than likely a facet of the heterogeneous nature of the substrate mixes. MCS_A displays considerable variation in porosity across the three layers. In the upper layer overall total porosity is only slightly reduced compared to MCS_V. However, there is a large increase in closed porosity and a subsequent decrease in open porosity. This is likely a result of the shift in the particle size distribution, associated with smaller particles are smaller pores, which can

more easily become separated from the wider pore matrix. Alternatively the presence of roots and stems could be misidentified closed pores (as these display as pore-like holes in XMT images), which may be influencing the overall porosity values.
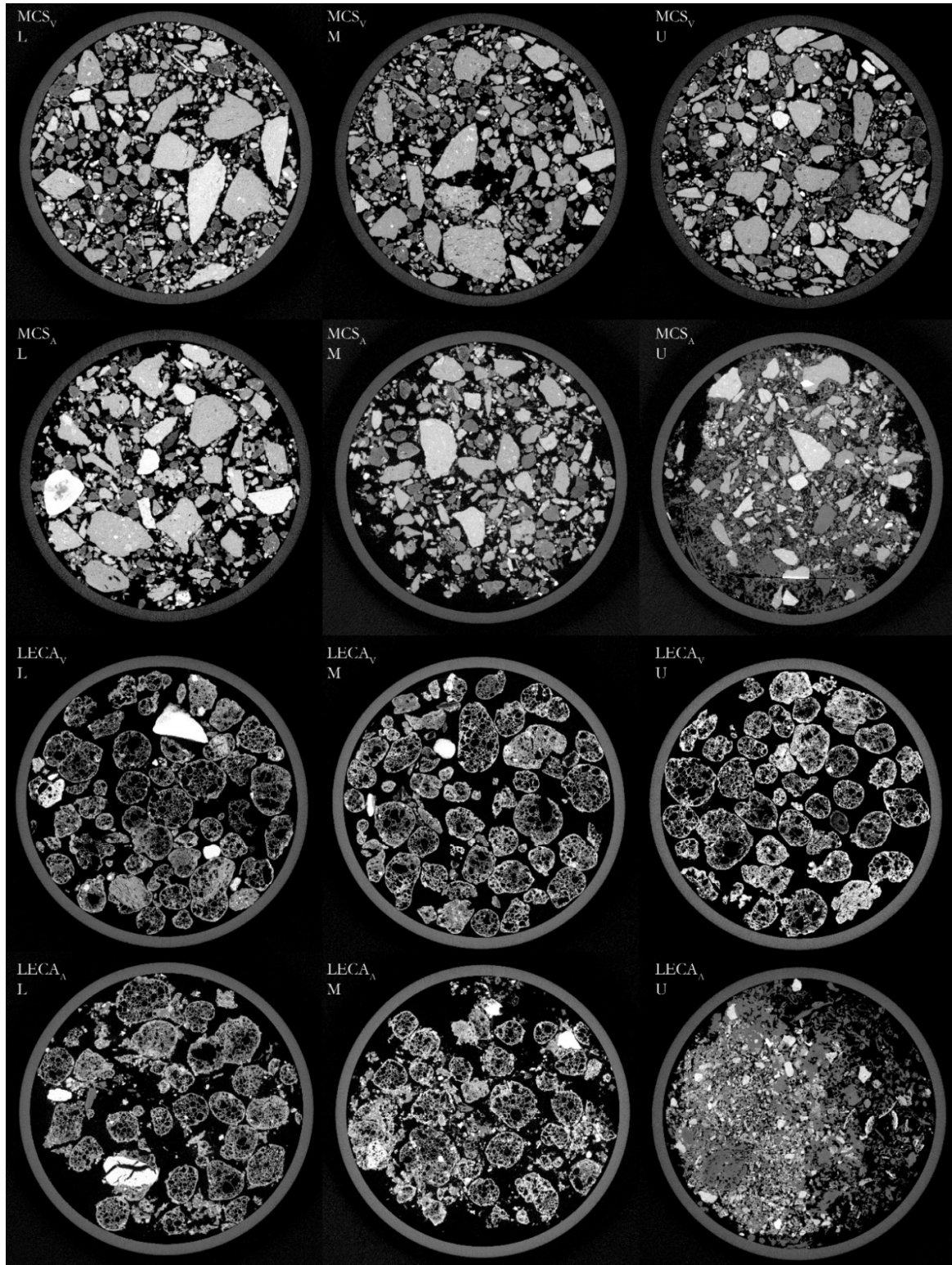

Figure 2: Reconstructed XMT slices (horizontal plane) from the lower, middle and upper layers (as illustrated in Fig. 1) of the four substrate cores.
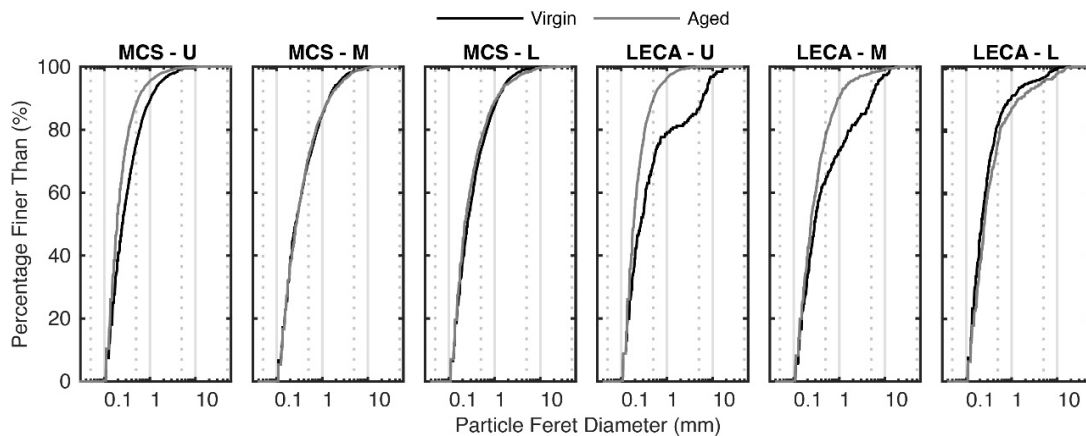
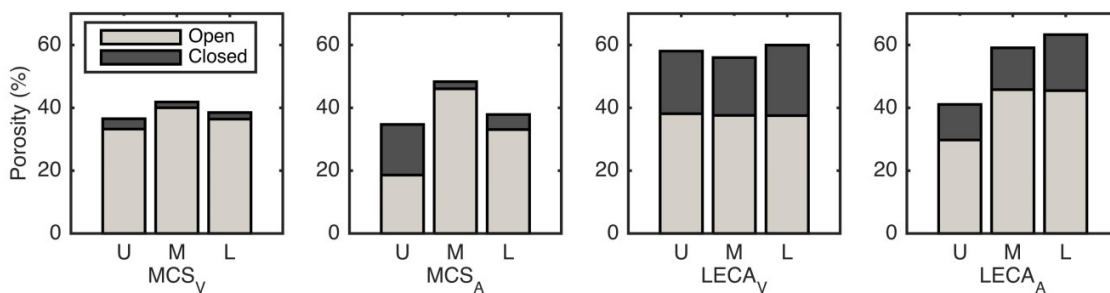Figure 3: Particle size distributions as computed from the XMT slices of Fig. 2.

Figure 4: Calculated open and closed porosity of the four substrate cores.

LECA$_A$ has a reduced total porosity compared to that of LECA$_V$ for the upper layer. This is largely due to material from the Sedum planting, something that is not present in the LECA$_V$. The lower two layers of LECA$_A$ retain a similar total porosity to that of LECA$_V$. However, there is a reduction in the ratio of closed to open pore space. This indicates that the previously closed internal pore networks of the LECA particles have broken open, potentially as a result of root action, and have now become connected to the wider open pore network.

Implications of Altered Properties

The change in properties, i.e. the shift in PSD and altered porosity, for the aged substrate cores compared with the virgin cores, could have detrimental impacts on their abilities to meet their initial design criteria. A reduced porosity will reduce the air and water holding capacities of the substrate. Plants need an adequate air supply to their roots in order to survive, if the porosity continues to fall oxygen levels in the soil could become so low as to prevent sustained vegetative cover. Not only would a die-off of vegetation lead to a reduction in the bio-diversity benefits of a green roof, it would also impact on hydrological, acoustic and thermal performance. The shift in PSD to more small particles may result in clogging of green roof filter sheets if these fines leach through to the lower layers, preventing free-draining conditions causing water volumes to build up within the roof system. Additionally, the smaller lighter particles will be more susceptible to wind erosion and scouring.

CONCLUSIONS

The non-invasive nature of XMT makes it an ideal tool for the examination of green roof substrate properties in a non-destructive fashion. This permits the preservation of the core and allows for further tests (e.g. permeability tests, hydraulic conductivity tests) to be conducted on an intact sample, something that could not be undertaken using existing destructive methods.

This study provides evidence that the properties of green roof substrates do change as a result of ageing. It can be seen that ageing processes lead to a reduced porosity and smaller particle sizes in the upper layers of the green roof substrate. However, because the aged and virgin cores are different samples of a heterogeneous substrate, the properties of the

virgin core analysed here cannot be assumed to correspond exactly with the original properties of the aged sample. Hence, the quantitative changes identified here should be considered indicative rather than absolute.

Further Research

To eliminate the uncertainty seen between aged and virgin samples of the substrate, new green roof microcosms will be developed. These microcosms will be imaged using XMT at regular intervals to determine the changes in physical substrate properties over time. In conjunction a full 3D image analysis will be undertaken. This will provide a more complete picture of key properties throughout the entire microcosm, compared to a 2D slice analysis.

ACKNOWLEDGEMENTS

REFERENCES

[1] Li, Y., Babcock Jr, R., Green roof hydrologic performance and modeling: a review, Wat. Sci. Tech., (2013) 1–12.

[2] Getter, K.L., Rowe, D.B., Andresen, J. a., Quantifying the effect of slope on extensive green roof stormwater retention, Ecol. Eng., 31 (2007) 225–231.

[3] Emilsson, T., Rolf, K., Comparison of establishment methods for extensive green roofs in southern Sweden, Urban Forestry & Urban Greening, 3 (2005) 103–111

[4] Menon, M., Yuan, Q., Jia, X., Dougill, J., Hoon, S.R., Thomas, D., Williams, R., Assessment of physical and hydro-logical properties of biological soil crusts using X-ray microtomography and modeling, J Hydrol, 397 (2011) 47–54.

[5] Taina, I.A., Heck, R.J., Elliot, T.R., Application of X-ray computed tomography to soil science: A literature review, Canadian Journal of Soil Science, 88 (2008) 1–19.

[6] Poë, S., Stovin, V., Beretta, C., Parameters influencing the regeneration of a green roof's retention capacity via evapotranspiration, J Hydrol., 523 (2015) 356–367.

[7] Yio, M.H.N., Stovin, V., Werdin, J., Vesuviano, G., Experimental analysis of green roof substrate detention characteristics, Wat. Sci. Tech., 68 (2013) 1477–86.

[8] Kasmin, H., Stovin, V., Hathway, E.A., Towards a generic rainfall- runoff model for green roofs, Wat. Sci. Tech., 62 (2010) 898–905.

[9] Berretta, C, Poë, S, Stovin, V., Moisture content behaviour in extensive green roofs during dry periods: The influence of vegetation and substrate characteristics, J Hydrol, 511 (2014) 374–386.

[10] Schneider, C.A., Rasband, W.S., Eliceiri, K.W. NIH Image to ImageJ: 25 years of image analysis, Nature Methods, 9 (2012) 671-675.

Geotechnical challenges in providing ground source cooling through pile foundations

N. Lazenby

E-Futures DTC - University of Sheffield
Nicola.lazenby@sheffield.ac.uk

Primary Supervisor:	Dr **P. Shepley** – e-mail: paul.shepley@sheffield.ac.uk
Secondary Supervisor:	Dr **C. C. Smith** – e-mail: colin.smith@sheffield.ac.uk

ABSTRACT. Pile foundation heat exchangers (PFHX) have the potential to significantly reduce the carbon emissions associated with air conditioning for commercial buildings. UK adoption of PFHX, although increasing, is still very low due to the uncertainty about their performance and structural integrity. This study aims to highlight the areas of research that have been conducted and the scope of the work carried out in this area alongside further research on the effect of cyclic temperature variation in clays. This research is recommended in order to produce a framework for responses to a pile foundation operating as a heat exchanger. This is one of the areas identified for further investigation to improve the confidence and reliability of PFHX in order to become a more broadly adopted technology.

KEYWORDS. Clay; Cyclic temperature; Heating; Cooling; Microstructure.

INTRODUCTION

Pile foundation heat exchangers (PFHX) have the potential to significantly reduce the carbon emissions produced by air conditioning in large commercial and public buildings. By 2020 it is expected that around 40% of commercial floor spaces will be air-conditioned. This is at a time when the Energy Performance of Buildings Directive (EPBD) is influencing the UK building regulations, providing challenging targets for the conservation of fuel and power [1]. A change in refrigerant legislation is also forcing companies to look towards alternative cooling strategies [2].

PFHX require a heat exchanger loop to be incorporated into the pile foundation, however installation follows that of traditional piles; driven and cast in-situ piles can both be utilised as heat exchangers. The heat exchanger loop works in combination with a heat pump to allow for heat energy in the building to be transferred into a refrigerant that circulates within the heat exchanger loops and into the ground surrounding the foundation [3]. This poses the potential for a long-term build up in the ground temperature surrounding a PFHX, especially if many are used across several congested city sites. Given the UK climate, stakeholders predict that in the future 60% of a year there will be a demand for cooling which would cause thermal cycling of the ground around a PFHX [2]. Such thermal cyclic effects have the potential to be significantly damaging to long-term foundation performance in certain soil types.

This paper summarises the main areas that pile foundation heat exchangers have been studied and the areas of further research required in order for industry to further invest in this technology as a valid solution to low emission air conditioning in commercial buildings.

FIELD STUDIES

Across Europe there have been a limited number of field studies carried out to identify the potential of pile foundation heat exchangers and the problems that may arise. A successful PFHX would be one which performers within the tolerances of a standard pile foundation whilst allowing for efficient heat exchange into the surrounding ground. Across the case studies, information and varying operational use has been omitted, such as ground properties, meaning accurate interpretation of outcomes cannot be reliably determined. The most extensive field studies have been carried out at Swiss Federal Institute of Technology (EPFL), Lausanne, Switzerland and Lambeth College, London, UK.

The study at EPFL [4] considered a 4 storey building, 30 m by 100 m founded on 97 PFHX. The test pile had a given diameter of 0.88 m and length of 25.8 m. Installed in predominately moraine, the pile was subject a 15 °C temperature increases following an initial temperature increase of 21 °C with a maximum structural load of 1300 kN. Thermal loading and structural loading of the pile, as the buildings construction progressed, were not carried out simultaneously. An alternating sequence was carried out upon completion of a structural section. The testing at EPFL aimed to provide validation for finite element modelling to simulate the behaviour of PFHX during operation. During the test period of 28 days, a net displacement of 1 mm at the pile head was witnessed, however a maximum displacement of 4 mm was observed in the middle of the test period. Conclusions of the testing reported thermo-elastic strains within the pile, with their intensity dependant on the type of surrounding soil. Due to the difference in directional movement, uplift for thermal loading and settlement for static loading, the friction resistance of the pile was deemed not to be impacted, however relief of side friction mobilisation was observed during heating. As the induced thermal strains are limited, it is thought by Laloui et al. [4] that there is no affect on the pore water pressure or the effective stress. The EPFL study provides evidence that temperature load cycles contribute to vertical movement of a pile foundation, however Laloui et al. does not provide evidence for the nature of the movements; this could be due to the expansion and contraction of the pile itself or the surrounding ground, or a combination of both.

The study at Lambeth College [5] the authors aimed to address the thermo-dynamic behaviour of an energy pile during heating and cooling cycles. Testing was carried out during the construction of a 5-storey building founded on 143 pile foundations, installed in London Clay, with a diameter of 0.6 m and lengths ranging between 19 m and 24 m. An average structural load of 1025 kN was applied to the piles, with a heating load imposed on the piles ranging from -6 °C and 56 °C. Following a periods of pile cooling and heating, daily heating and cooling cycles were carried out. The net pile head displacement over the duration of testing was 3 mm, with a maximum displacement of 10 mm. Similarly to the EPFL field study; it is not possible to determine the nature of this displacement. The displacement could be attributed to the expansion and contraction of the concrete, the surrounding ground or a combination of both elements.

PILE DESIGN

Design guides produced by the Ground Source Heat Pump Association [6] for the installation of PHFX consider only the temperature effects of PFHX systems rather than the long-term cyclic temperature effects which would replicate actual PFHX operation. Bourne-Webb et al. [7] has produced a descriptive framework following on from the Lambeth College field study [5]. The framework developed analyses the strains that occur within the pile foundation during heating and cooling. The pile is considered as a free body, a perfectly restrained body and a PFHX with mechanical head load, during both heating and cooling. The framework produced by Bourne-Webb et al. [7] is comparable, to certain degree, with the observed field study results by the same author, however the results provided do not take into consideration variations in ground properties and the progressive responses to thermal cycles. Bourne-Webb et al. [7] consider the soil-structure interaction comparable to that of excavation heave or negative skin friction with the addition of the soil deformation resulting from the internal deformation of the pile with temperature variation. Bourne-Webb et al. [7] do not consider the deformation in the soil as a response to the thermal variation as part of their framework of pile behaviour. Loveridge & Powrie [3] have identified that during PFHX operations heat will be transferred to the soil, by means of conduction through the pile concrete, to surrounding the pile foundation. Experimental studies have identified that a significant response to thermal variation can be witnessed in soil behaviour; in addition to the interactions detailed by Bourne-Webb et al. [7], a soils response to change in temperature will be present and influence the piles behaviour.

EXPERIMENTAL STUDIES

Current literature presents very little information on the influence of cyclic temperature variation imposed on the pile to soil interface. In early studies, the response of clay to temperature was considered with regard to the shear strength [8] volume change and pore pressure variation [9]. A recent study by Abuel-Naga et al. [10] has considered the impact of temperature on a range of general engineering properties. These include permeability, compressibility and shear strength through a study on soft clay with low plasticity. Other studies have addressed individual engineering properties including the effect on overconsolidation ratio [11] and plasticity [12]. However, these studies have been carried out for individual clay types and discrete temperature increases. Results from these studies have yet to be unified into a single framework for pile design.

Campanella & Mitchell [9] identified that during heating, a change in sample height occurred. What is not known from the investigation is whether the change in height of the sample was attributed to a change in diameter of the sample i.e. barrelling or isotropic expansion. It is possible that radial expansion of the sample may occur due to the isotropic expansion of the sample during heating followed by anisotropic contraction of the sample during cooling, with axial contraction dominating.

Abuel-Naga et al. [10] and Cekerevac & Laloui [11] both concluded that the stress history of a sample influences the degree of thermal expansion or contraction produced through heating. Normally consolidated and lightly overconsolidated samples were found to contract, with heavily overconsolidated samples dilating upon heating. Although not evidenced, Campanella & Mitchell [9], Abuel-Naga et al. [10] and Cekerevac & Laloui [11] stipulate that the change in sample temperature produced an effect on fabric of the clay with interparticle forces and the viscous shear resistance of the absorbed water being affected. The understanding of these changes will significantly aid the future interpretation of thermal effects.

With regard to the effect of temperature on the stiffness and shear strength of a clay, Abuel-Naga et al. [10] identified that higher temperatures increased the shear strength and stiffness of Bangkok clay. However, evidence of this in current literature relating to other clay types has not been identified. Towhata et al. [12] conducted tests on kaolin and bentonite samples within a temperature controlled oedometer. Samples were incrementally heated whilst their void ratio was monitored. Testing showed that during heating a reduction in void ratio of 3% for kaolin and 12% for bentonite was observed. As testing was for heating only the effect of cyclic void ratio change during the cooling stages require further investigation.

In the current literature there is a consensus that the clay in which the PFHX is situated will function in an undrained condition during a change in temperature. The drainage state of the clay is dependent upon its permeability. Testing clays with varying plasticities over multiple cycles will build upon the work of Towhata et al. [12] whilst identifying thermal trends allowing for verification of previous studies such as Abuel-Naga et al. [10], Towhata et al. [12] and Cekerevac & Laloui [11] in order to produce a frame work for pile design incorporating temperature variations.

FUTURE RESEARCH

To further develop the PFHX industry, reliable yet broad guidance on the variation in strength and stiffness of clay following multiple cycles of temperature variation is required. As highlighted, one of the areas of weakness is an understanding of clays response to cyclic temperature variation and the impact this has on foundation design. Testing to address the long term effects of PFHX on the clay surrounding the soil-pile interface is to be carried out using a modified triaxial system influenced by the system developed by Laloui et al. [4]. The triaxial system simulates infield conditions by allowing control of both stress and temperature simultaneously within the cell. The system developed at the University of Sheffield (Fig. 1) incorporates a copper-heating coil installed to allow for temperature of the water within the triaxial.

An expansion ring at the base of the cell was commissioned for the installation of thermocouples within the cell. These thermocouples are used in the calibration of the test system and monitoring of the temperatures during testing. To regulate the temperature of the cell a bespoke heating system was manufactured. This included a regulated heated water bath and central heating pump with a maximum pressure of 6 bar and a maximum flow rate of $3.5 m^3/h$, in order to circulate water at a high enough pressure to enable efficient heating. Staged heating and cooling is carried out using a program developed in Labview. This operates as a thermostat, with the desired temperatures being input. In order to further identify the changes that occur within the sample during the thermal cycles, local linear variable differential

transformer (LVDT) will be installed on the sample. The pressure and volumes within the cell, sample and loading ram will be controlled using GDS Instruments pressure transducers. These will allow for an automatic maintenance of pressures independent of volume change.
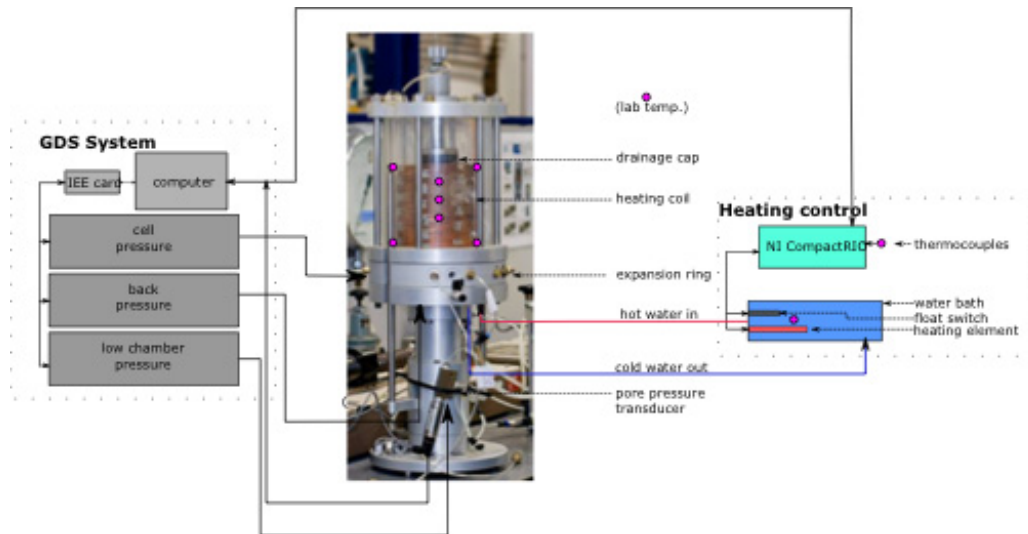

Figure 1: University of Sheffield triaxial system with temperature regulating modifications.

This study will primarily be performed on two clays with varying plasticity. One sample will be produced purely from a kaolin slurry, whilst the other will be formed from a combination of kaolin and bentonite mix at a ratio of 60:40 kaolin:bentonite by mass to provide a higher plasticity sample to that of purely kaolin [13]. Varying the plasticity of test samples will aid the understanding of the influence that plasticity and permeability contributes to a sample's response to thermal cycles. Samples will be produced by consolidating clay slurry to 500 kPa within a 250 mm diameter Rowe Cell, maintained at 20 °C. From the large Rowe Cell sample, samples of 50 mm diameter and 100 mm in height will be cut for tested. By consolidating samples to 500kPa, the samples produced will be significantly stiff, this will allow for minimal impact of the local LVDT on the samples deformation.

Following saturation, samples will be isotropically consolidated to 600 kPa within the triaxial system, at 20 °C, laboratory temperature. During shearing a mean effective stress of 500 kPa is to be applied to the sample. During the heating phase the sample will be in a drained condition. This allows for excess pore water pressure to dissipate as found by Campanella & Mitchell [9], Burghignoli et al. [14] and Cekerevac & Laloui [11]. Undrained shearing will be carried out after reaching thermal equilibrium.

Calibration of the system was initially carried out with the installation of an incompressible sample. This allowed for the local LVDT's to be tested with varying temperature to verify the manufacturer's temperature guidelines. An instrumented clay sample was then used in the calibration of heating and cooling rates (Fig. 2). This will allow testing to be carried out without the inclusion of thermocouples within actual test samples. The temperature of the top cap and base cap will be used to indicate the temperature of the sample and the heating periods required. A sinusoidal curve will be used for the heating and cooling to provide repeatability in the temperature cycles. Providing consistent and replicable heating and cooling is one of the major challenges within the study. In order to determine the time taken for the sample to reach the desired temperature, thermocouples were embedded within a consolidated kaolin sample and monitored during a staged heating phase (Fig. 2 (a)). At the time of testing, no insulation of the cell was present. This provided a baseline result for the minimum achievable temperatures within the system. It can be noted that the thermocouple embedded in the bottom of the sample is significantly cooler than the top and middle thermocouples. This was found to be due to an imperfect seal around the base cap.

Results shown in Fig. 2, indicate that it takes ~1-2 hours to achieve a temperature increment of 10-20 °C. The rate at which heating occurs within the sample is important to consider with regard to the prevention of excess pore pressures building up within the sample. Plum & Esrig [15] found that for Newfield Clay with an initial void ratio of 0.462, an increase in 20 °C produced an increase pore pressure of 100kPa on average of 5 cycles. Excess pore pressures have the potential to impact the fabric and mechanical properties of the sample, which may overshadow the impact of heating on these properties in the case of drained heating.
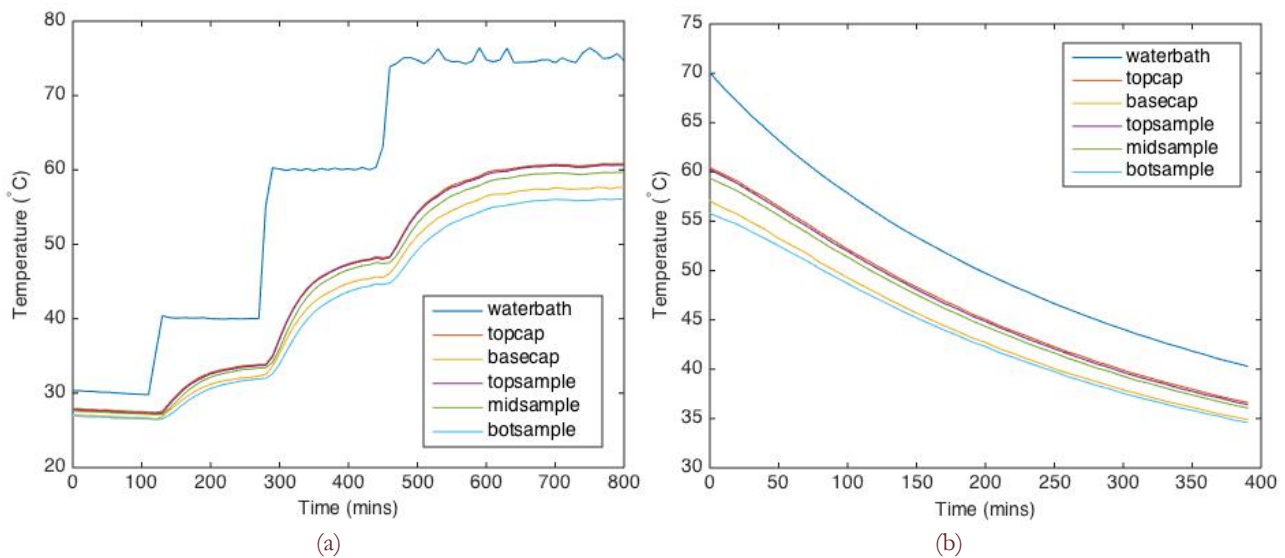
Figure 2: Triaxial calibration curves for: (a) sample heating; (b) sample cooling.

Cooling is carried out at the rate of heat loss from the cell within a temperature-controlled 20 °C laboratory, with the pump switched off. This is the quickest method of reducing the sample temperature. Fig. 2 (b) shows the time taken for the sample to decrease in temperature.

One of the challenges is achieving staged cooling. In order to provide staged cooling, the drop in temperature must be monitored in order for the water bath heating system to be engaged to maintain a given temperature. An alternative is to decrease the water bath temperature whilst water is still circulating. However, this does increase the duration required for cooling of the sample but allows for drainage of the sample to be maintained.

The modified triaxial system will be used to investigate the shear strength of 2 clays of different plasticity (kaolin and kaolin/bentonite mixed samples), at fixed temperatures and following multiple temperature cycles. Shear strength tests at constant temperature will be carried out at 20°C, 40°C and 60°C in order to determine the differences that a direct increase in temperature has on the mechanical properties of a clay.

To build on the work carried out by Abuel-Naga et al. [10] the influence of cyclic temperature variation will be investigated on an isotropically consolidated sample. The temperature of the sample will be cycled between 25°C and 60°C for 5 and 10 repetitions, prior to shearing. This will allow an assessment of shear strength and stiffness post cyclic temperature variation to be identified in addition to any accumulated cyclic thermal deformation.

The study aims to more thoroughly understand the performance of clays under temperature changes – either through a permanent increase or through cyclic changes. The effect of cyclic temperature variation has the potential to change the shear strength and stiffness of clay. This study aims to unite an array of previous studies into one theory for predicting clay performance under temperature change, which should ultimately help guide future PFHX design.

REFERENCES

[1] Carbon Trust, Air Conditioning. Maximising comfort, minimising energy consumption, UK, (2007).

[2] Evidence Directorate, Ground source heating and cooling pumps – state of play and future trends, (2009).

[3] Loveridge, F., Powrie, W., Pile heat exchangers: thermal behaviour and interactions, In: Proceedings of the Institution of Civil Engineers, (2012).

[4] Laloui, L., Nuth, M., Vulliet, L., Experimental and numerical investigations of the behaviour of a heat exchanger pile, Int. J. Numer. Anal. Methods Geomech, 30(8) (2006) 763–781.

[5] Bourne-Webb, P. J., Amis, T., Soga, K., Davidson, C., Payne, P., Amatya, B., Energy pile test at Lambeth College, London: geotechnical and thermodynamic aspects of pile response to heat cycles, Géotechnique, 59(3) (2009) 237–248.

[6] Ground Source Heat Pump Association, Thermal Pile Design, Installation & Materials Standards, (2012).

[7] Bourne-webb, P. J., Soga, K., Amatya, B., A framework for understanding energy pile behaviour, In: Proc. ICE - Geotech. Eng., 2009 (2011) 1–8.

[8] Mitchell, J. K., Fundamentals of soil behaviour. New York, USA: John Wiley & Sons Inc., (1993).

[9] Campanella, R. G., Mitchell, J. K., Influence of temperature variations on soil behaviour, ASCE, 94(3) (1968).

[10] Abuel-Naga, H. M., Bergado, D. T., Bouazza, A., Ramana, G. V., Volume change behaviour of saturated clays under drained heating conditions : experimental results and constitutive modeling, c (2007) 942–956.

[11] Cekerevac, C., Laloui, L., Experimental study of thermal effects on the mechanical behaviour of a clay, Int. J. Numer. Anal. Methods Geomech., 28(3) (2004) 209–228.

[12] Towhata, I., Kuntiwattanaku, P., Seko, I., Ohishi, K., Volume change of clays indued by heating as observed in consolidation tests, Japanese Geotech. Soc. NII-Electronic Libr. Serv., 33(4) (1993) 170–183.

[13] Karunaratne, G. P., Chew, S. H., Lee, S. L., Sinha, A., Bentonite: Kaolinite Clay Liner, Geosynth. Int., 8(2) (2001) 113–133.

[14] Burghignoli, A., Desideri, A., Miliziano, S., A laboratory study on the thermomechanical behaviour of clayey soils, Can. Geotech. J., 37(4) (2000) 764–780.

[15] Plum R. L., Esrig, M. L., Some temperature effects on soil compressibility and pore water pressure, Highw. Res. Board, Spec. Rep. 103, Conf. Eff. Temp. Heat Eng. Behav. Soils, (1969) 231–242.

Pounding response of structures under earthquake motions

N. Farhadzadeh
University of Sheffield
Nfarhadzadeh1@sheffield.ac.uk

ABSTRACT. Pounding of structures is a common phenomenon between adjacent structures with out-of phase response which is caused by lateral seismic motions. Before the introduction of earthquake resistant design many buildings were built without any gaps between them and sometimes connected with one or two structural members. During pounding events, contact forces with high amplitude and short duration are generated which could lead to damage or total collapse of buildings. Over the past two decades, the study of building pounding and precise estimation of these contact forces has been studied by adopting several contact models. However there are still uncertainties with the adequacy of these models as different models produce different results for predicting the response of a single structure. The aim of this research is to develop/expand a contact model which can overcome the disadvantages and uncertaintaies of the existing contact models in predicting the contact forces to model seismic pounding.

KEYWORDS. Structural pounding; Hopkinson pressure bar; Contact model; Coefficient of restitution

INTRODUCTION

Pounding frequently occurs between adjacent structures with insufficient distances during earthquake where the distance between structures is not adequate to accommodate the relative movements. The relative displacements are caused by several factors such as dynamic characteristics of structure, its soil foundation and the ground motion spatial variation [1]. The most severe structural pounding reported was in the Mexico City earthquake in 1985 and Loma Prieta 1989 which resulted in the collapse of 3% to 4.5% of the buildings [2]. A survey of Loma Prieta earthquake was carried out in 1997 by Maison & Kasaei [3] who reported that mainly old adjusted structures, those structures located on soft soil and also the structures without vertical reinforcements built before 1930 were subjected to pounding.

Folz & Perion [4] investigated structural pounding caused by Saguenay earthquake in Canada. Pounding was observed in several adjacent buildings as well as the Shipshaw bridge deck against its abutments. One of the main reasons for damage/collapse of the buildings in Saguenay earthquake was pounding of structures with different heights and storey levels. The pounding forces caused by the ground motions resulted in an excessive shear forces above the buildings contact point.

The best possible way of estimating the structural responses during pounding events is through an accurate prediction of the expected force-displacement response of the adjacent buildings where the application of contact models becomes important. Over the past two decades several contact models have been adopted to estimate these forces caused by structural impact. Despite the extensive research conducted on contact behavior of structures, there is still a significant

issue with the choice of a precise contact model. In the analysis of structures even if a model adequately determines the contact forces in a single situation, defining the contact parameters can be complicated [5].

EXISTING CONTACT MODEL

Hertz contact model

All of the primary/ expanded contact models are based on Hertz law of contact which was originally proposed to estimate the contact forces resulted from an elastic impact between a sphere and a flat surface as shown in Eq. 1-3 [6].

$$F = K_{(t)} \times Z_{(t)}^{3/2} \tag{1}$$

$$K_h = \frac{4}{3} \sqrt{RE^*} \tag{2}$$

where Z, K and R are the relative displacement, contact stiffness and the diameter of the spheres.

$$\frac{1}{E^*} = \frac{1 - v_1^2}{E1} + \frac{1 - v_2^2}{E2} \tag{3}$$

where E, E* and v are the young modulus, effective modulus of elasticity and the Poisson ratios of the contacting bodies. The Hertz contact law is not adequate enough to estimate the contact forces for every structure as mentioned it is only limited to elastic impacts and it also does not account for energy dissipation during contact. The Hertz law of contact is the raw model of linear and non-linear elastic models which have been slightly modified. The updated Hertz law of contact, the linear viscoelastic model is a usual method of determining the pounding forces as shown in Eq. 4-6. In the linear viscoelastic model the K values are determined based on force-displacement histories obtained from experimental tests [7] and it is stated to be in the range of 1.30×10^{10} to 5.44×10^{10} for steel-steel impact and 7.90×10^9 to 10.45×10^9 for concrete-concrete collision.

Linear viscoelastic model

$$F(t) = K\delta(t) + C\dot{\delta}(t) \tag{4}$$

$$C = 2\zeta \sqrt{\left(K \frac{m_1 m_2}{m_1 + m_2} \right)} \tag{5}$$

where K is the element stiffness, δ is the structural member deformation, $\dot{\delta}$ is the relative velocity and C is the damping coefficient. The damping ratio (ζ) is calculated using the coefficient of restitution (e) value as shown in Eq. 6.

$$\zeta = \frac{-Ln\, e}{\sqrt{\pi^2 + \sqrt{(\ln e)^2}}} \tag{6}$$

The disadvantage of this contact model is that it assumes uniform energy dissipation during the loading stage and in the restitution period of contact. Later on the linear viscoelastic model was updated [7] which could estimate the energy dissipation during just for the contact approach period. For simplicity, this model neglects the energy dissipation in the restitution period as shown in Eq. 7-9.

Updated linear viscoelastic model

$$F(t) = K\delta(t) + C\dot{\delta}(t); \quad \dot{\delta} \geq 0 \tag{7}$$

$$F(t) = K\delta(t); \quad \dot{\delta} < 0 \tag{8}$$

$$\zeta = \frac{1}{\pi} \frac{1 - e^2}{e} \tag{9}$$

There is also the non-linear viscoelastic model which is the non-linear form of the modified linear viscoelastic model but accounts for energy dissipation using different equation however this parameter is still obtained using the coefficient of restitution. The equations of this model are 10-13.

Non- linear viscoelastic model

$$F(t) = K\delta^{3/2}(t) + C\dot{\delta}(t); \quad \dot{\delta} \geq 0 \tag{10}$$

$$F(t) = K\delta^{3/2}(t); \quad \dot{\delta} < 0 \tag{11}$$

$$C = 2\zeta\sqrt{k\sqrt{\delta}\left(\frac{m_1 m_2}{m_1 + m_2}\right)} \tag{12}$$

$$\zeta = \frac{9\sqrt{5}}{2} \frac{1 - e^2}{e\left(e\left(9\pi - 16\right) + 16\right)} \tag{13}$$

As it can be observed that the mentioned primary contact models estimate the energy dissipation based on an indirect parameter which is the coefficient of restitution (e). It is worth mentioning that the oldest contact model which was used to model impact forces directly from the coefficient of restitution was the stereo-mechanics model. This model is no longer recommended to be used for estimating the contact forces as it is only based on the pre-impact and post-impact velocities and does not directly consider the forces. This model is unable to account for deformation of the impacted bodies as it assumes that the impact takes a very short time [7].

Stereomechanics model

$$V'_1 = v_1 - (1+e)\frac{m_1 v_1 - m_2 v_2}{m_1 + m_2} \tag{14}$$

$$V'_2 = v_2 - (1+e)\frac{m_1 v_1 - m_2 v_2}{m_1 + m_2} \tag{15}$$

$$(1) \quad e = \frac{v'_2 - v'_1}{v_1 - v_2} \quad \text{OR} \quad (2) \; e = \frac{h_2}{h_1} \tag{16}$$

where m_1, m_2, v_1, v_2 are the masses and the velocities of the structural elements. The second part of the Eq. (16) can be obtained by dropping a ball on a plate from a certain height (h_1) over its rebound height (h_2). In this model for a fully elastic impact the restitution coefficient value is equal to 1, and for a fully plastic impact e is 0. The value of restitution coefficient is assessed to be ranging from 0.50 to 0.75 for simulation of real structural pounding [7]. In addition to the primary contact models mentioned above, two other models, the modified hertz-damped model and the Hunt-Crossley model are presented in Tab. 1 [8]. The Hunt-Crossley model is also based on the Hertz contact law.

THE CURRENT RESEARCH

The current research focuses on comparing the existing contact models using numerical and experimental data for a possible expansion of an existing contact model which can precisely determine the contact forces during structural pounding. For this purpose a series of preliminary numerical simulations was conducted using ANSYS-LSDYNA. A 2D axi-symmetric Hopkinson pressure bar test setup was modelled as shown in Fig. 1 to have a precise estimation of the experimental setup parameters such as the impact velocity, the size of the samples, etc. The model was constructed in 3 parts; hopkinson pressure bar, striker and the specimen. Convergence analysis was conducted to determine the best mesh size for the finite element analysis of the model which was found to be 1 mm. Impact was modelled between concrete- concrete, steel-concrete and steel-steel materials. In the case of concrete-concrete impact the specimen was placed at the front of the Hopkinson bar whereas for steel- steel and concrete -steel impacts the specimens were placed at the front of the striker. The arrangement of the bar and the specimen is due to the restriction with the laboratory apparatus as well as simplifying the investigation of the results as shown in Fig. 2.

Hertz-damped model	$F(t) = K\delta^{3/2} + \zeta\,\delta^{3/2}\,\dot{\delta}$, $(1+e)=\dfrac{k}{\zeta\dot{\delta}}\ \ln\ \dfrac{\frac{k}{\zeta\dot{\delta}0}+1}{\frac{k}{\zeta\dot{\delta}0}-e}$
Linear Hunt-Crossley model	$F(t) = K\delta + \zeta\,\delta\,\dot{\delta}$ where ζ for both Hertz-damped model and the linear Hunt-Crossley model is obtained from the implicit equation

Table 1: Contact force models.
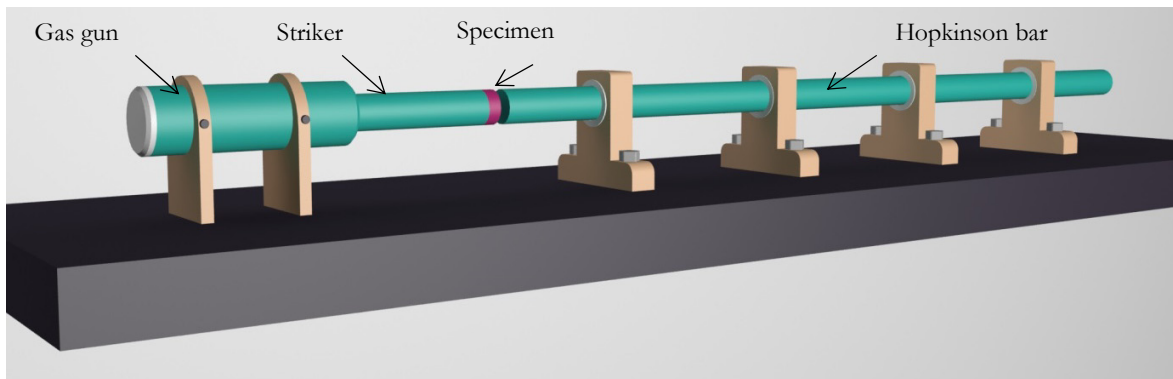
Figure 1: Hopkinson pressure bar set up.

Fig. 2 shows the contact force-time histories of steel to steel, concrete to concrete and concrete to steel impacts with the velocity of 25 m/s. The mentioned graph is one small part of the preliminary numerical simulation which was done to determine the precise laboratory setup to be conducted on the same procedure for verification of the numerical results. In LS-DYNA, for modelling steel- steel collision simplified Johnson-Cook material model was used and for concrete-concrete impact material model 72R3- damage concrete was used. All the force-time histories were obtained at the strain gauge location which is 494 mm away from the face of the Hopkinson bar.
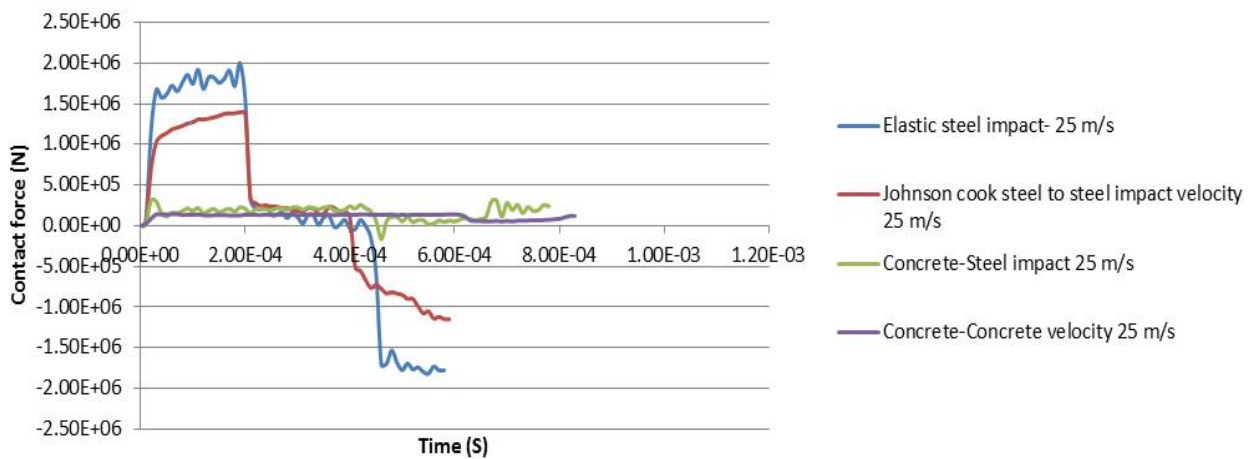
Figure 2: Force-time history of steel-steel impact with velocity of 25 m/s.

Once the experimental tests on a limited number of samples are carried out, the experimental results will be verified by the numerical models then it would be possible to model more collision numerically with more detailed data. Having the numerical and experimental results will give the possibility of comparing and applying the existing contact models to these data. Achieving precise information will make the comparison of the contact models possible therefore an existing contact model could be updated. The latter step would be to use the modified/novel contact model in pounding analysis of a

Single degree of freedom system. To accomplish the project, the novel contact model will be compared to the results obtained from the existing contact models for the same structural system.

CONCLUSION

Structural pounding is a severe event which can lead to damage/collapse of structures. In order to determine the contact forces caused by buildings' collisions several contact models have been adopted. For over two decades researchers investigated the adequacy of these contact models however there are still uncertainties with the existing contact models and their parameters as each contact model can give different result for a single case. This research aims at developing an adequate contact model which would be more reliable in estimating the structural responses than the existing ones. For this purpose an extensive preliminary numerical simulations are carried out for determining the experimental setup of the samples parameters however for the sake of brevity only the force-time history of a few impact models are presented in this paper. The variables in the numerical simulations are the structural material, the geometry and the applied velocity to the striker. Once these results are confirmed by the experimental tests, the force-displacement data will be implemented in the contact models for comparison. After verification is completed, accurate analysis will be conducted to obtain more precise data for more impact models. The accomplished numerical results will be used to compare and expand of the existing contact models. The expanded contact model will be tested against the rest of the existing contact models on pounding analysis of a single degree of freedom model.

REFERENCES

[1] Khatiwada, S., Nawawi, C., Limitation in simulation of building pounding in earthquakes. International journal of protective structures, 5 (2) (2014) 123-150.
[2] Goltabar, A.M., Kami, R.S., Ebadi, A., Analyzing the effective parameters in pounding phenomenon between adjacent structure due to earthquake, In: The 14th world conference on earthquake engineering, 1 (2008) 1-8.
[3] Kasai, K., Maison, B.F., Building pounding damage during the 1989 Loma Prieta earthquake, Engineering structures, 19 (1997) 195-207.
[4] Folz, B., Prion, H., Pounding of buildings during earthquakes: a canadian perspective, 1 (1993) 251-265.
[5] Yigit, A.S., Christofou, A.P., Majeed, M.A., A non-linear visco-elastoplastic impact model and the coefficient of restituition, Non-linear dynamics, 66 (2011), 509-521.
[6] Goldsmith, W., Impact: The Theory and Physical Behavior of Colliding Solids, 1st ed., Edward Arnold, London, (1960).
[7] Jankowski, R., non-linear viscoelastic modelling of earthquake-induced structural pounding, Earthquake engineering and structural dynamics, 34 (2005) 595-611.
[8] Khatiwada, S., Chouw, N., Butterworth, J.W., Development of pounding model for adjacent structures in earthquakes, In: Proceedings of the ninth pacific conference on earthquake engineering, 1 (2011) 1-8.

An elastoplastic model simulation to calculate local stress-strain sequences under uniaxial/multiaxial constant/variable amplitude cyclic loading

N. Zuhair Faruq

University of Sheffield, Department of Civil and Structural Engineering
Zfnamiq1@sheffield.ac.uk

Primary Supervisor:	Prof. **L. Susmel** – e-mail: l.susmel@sheffield.ac.uk
Secondary Supervisor:	Prof. **H. Askes** – e-mail: h.askes@sheffield.ac.uk

ABSTRACT. The demand for advanced design method to accurately analyse fatigue damage of complex systems under multiaxial variable amplitude loading condition, in conjunction with the minimum safety factors due to more emphasis on lighter structures, saving materials and cost reduction has been extremely increasing. The correct prediction of fatigue lifetime under multiaxial cyclic loading seriously depends on the description of local elastoplastic stress-strain sequences at the critical point on a component [1]. Furthermore, it's universally agreed that in all engineering components local elastoplastic stress/strain will vary according to the geometrical features and degree of multiaxiality. Consequently, estimating these sequences will be more complicated by the presence of notch under multiaxial loads. Accordingly, calculating the local elastoplastic stress-strain properties with sufficient accuracy will result in a reliable and realistic fatigue assessment. However, procedural standards to plot the local elastoplastic stress-strain properties without performing experiment work are not yet available when the reversal stress/strains are involved. For the sake of accuracy, people come to believe that performing an experimental investigation is the best way to accurately estimate the local stress-strain response of components under multiaxial loading. In contrast, engineering designers argued that time and monetary requirements in the experimental investigation, in addition to the economic consideration or sometimes difficulty in accessing an accurate experimental testing machine parallel to the development of modern programing have increased attention on the use of numerical simulation model analysis. In the light of the above well-known fact, the present paper summarises an attempt to correctly formalise a novel model to be used to predict fatigue life time of unnotched components. The proposed elastoplastic model was analysed by using finite element (FE) program system ANSYS under reversed constant/variable amplitude uniaxial and torsion, as well as in-phase and out-of-phase multiaxial (tension-torsion) strain controlled loading at room temperature. From a reliability and safety point of view, a systematic validation exercise is followed by: First, using 38 experimental data sets from other technical literatures [6,7,8,9,10 &11] generated by testing 6 different materials under various loading conditions. Second, comparing the predicted local stress-strain properties with the result obtained from Jiang's model [2] that was built based on the material properties and constants obtained from the experimental test. To conclude, the local predicted hysteresis loops are compared with their experimentally determined counterparts and the results from Jiang's model. Such an extensive exercise showed that the proposed model has the capability of describing the local elastoplastic deformation features of materials under different cyclic loading. The overall scientific goal beyond this research is to formalise and verify a novel systematical study to simulate an accurate model, which can be used to estimate fatigue life time of notched metallic components under multiaxial variable amplitude loading case that will be outlined in the next steps of this research.

KEYWORDS. Elastoplastic model; Cyclic plasticity; Notched component; Variable amplitude.

INTRODUCTION

In general, engineering components are often exposed to a complex tension, torsion and combined constant/variable amplitude service load sequences resulting in a local multiaxial elastoplastic stress/strain state at the fatigue process zone. However, the stress-strain responses that are developed due to multiaxial loading conditions on notched components are much more complicated and exaggerated, particularly at the notch tip [3]. Different fatigue theories have been developed so far under different strategies, but a unique design methodology appropriate to investigate and estimate fatigue damage of notched components under variable amplitude multiaxial loading has not yet been agreed by the scientific community [4]. On the other hand, the engineeirng designers need sound methods mainly focus on multiaxial fatigue lifetime evaluation of stress raised components under variable amplitude loading conditions. Consequently, evaluation and assessment fatigue lifetime of such components have become an integral part of the design process and a complex problem that has to be addressed properly. It is universally agreed that in all engineering components, local elastoplastic stress/strain vary according to the geometrical features and degree of multiaxiality. Accordingly, fatigue problem is complicated in the presence of notches, and decreases structures lifetime. Strain based approach is recommended to perform low/medium fatigue assessment if the local elastoplastic sequences of material is correctly modeled and described [5]. This is attributed to the fact that the correct estimation of the local elastoplastic stress-strain relationship is important to accurately identify fatigue damage of a component. This paper aims at providing a systematical study to correctly model the elastoplastic stress-strain response of unnotched components under multiaxial variable amplitude cyclic loading. Due to extensive research investigation and well developed level of experimetnal fatigue assesment for unnotched components, the initail part of the research program as organised in this paper is focused on modeling and analysing unnotched component under a complex system of loading conditions, and the obtained results are compared with the experiementally performed work by others [6,7,8,9,10 & 11] as well as result from Jiang's model [2]. Further steps of the program will be focusing on the development of a reliable and theortical notched model based on the investigations from the initial part through deep insight into the fatigue mechanisms and behaviour of damged process zone under variable amplitude multiaxial loading.

Tensile Properties	304 Stainless Steel [6]	Stainless Steel [7]	SNCM630 Steel [8]	1% Cr-Mo-V [9]	45 Steel [10]	S45C [11]
E (GPa)	183	200	196	200	190	186
G (GPa)	82.8	77	77	76.9	79	70.6
v	0.3	0.3	0.273	0.3	0.202	0.28
σ_y (MPa)	325	365	951	707	370	496
σ_u (MPa)	650	----	1103	805	610	770
σ'_f (MPa)	1000	865	1272	987	843	923
b	-0.114	-0.097	-0.073	-0.071	-0.1047	-0.099
ε'_f	0.171	0.119	1.54	1.369	0.3269	0.359
c	-0.402	-0.359	-0.823	-0.802	-0.5458	-0.519
K' (MPa)	1660	1329	1056	1113	1258	1215
n'	0.287	0.244	0.054	0.11	0.208	0.217
Cyclic Torsional Properties:						
τ'_f (MPa)	709	500	858	570	559	685
b_o	-0.121	-0.097	-0.061	-0.071	-0.1078	-0.12
γ'_f	0.413	0.206	1.51	2.371	0.496	0.198
c_o	-0.353	-0.359	-0.706	-0.802	-0.469	-0.36
K'_o (MPa)	785	----	592	----	----	----
n'_o	0.296	----	0.05	----	----	----
Coefficient of Nonproportionality (Out-Of-Phase), $K'_{NP} = 1.25 K'$ and $n'_{NP} = n'$, [5]						
K'_{NP} (MPa)	2075	1661	1320	1391	1573	1519
n'_{NP}	0.287	0.244	0.054	0.11	0.208	0.217

Table 1: Material properties from the other technical experimental work

FORMULATING THE MODEL

A plain cylindrical shaft is considered with material properties described from the previous technical literature. Almost all elastoplastic properties and constants of the materials were taken from the original papers [6,7,8,9,10 & 11]. All data sets are listed in Tab. 1. The missed torsional fatigue data (cyclic torsional properties of the materials) that was not given in the original papers were described by using von Mises criterion [12]. An elastoplastic unnotched model is analysed. To perform a comprehensive investigation, various loading cases, paths and amplitudes are applied as shown in Fig. 1. Multiaxial constant/variable amplitude loading are considered in the analysis as summarised in Tab. 2 and 3. The equivalent cyclic stress-strain amplitudes were fitted by using Ramberg-Osgood relationship [13]. Finite element ANSYS program is used to perform the analysis [14]. The result showed all considered materials are plastically responded.
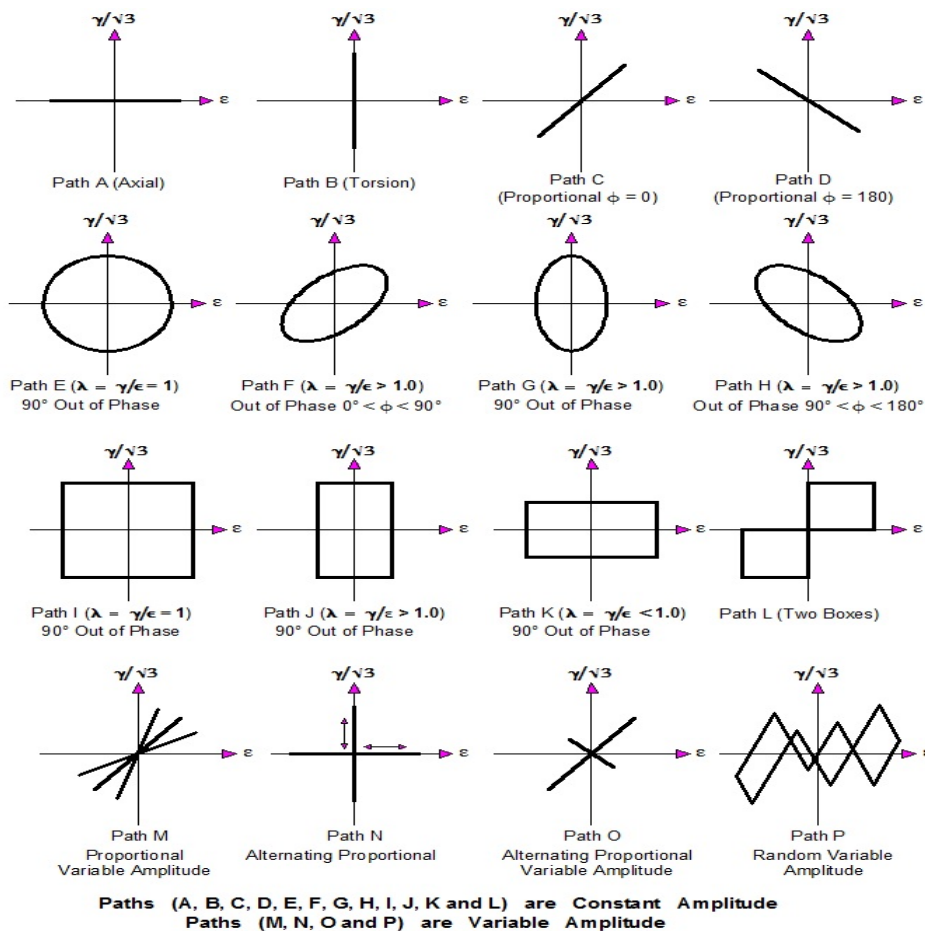

Figure 1: Schematics of strain paths (Constant and Variable Amplitudes).

RESULTS AND COMPARISON

In order to overview the accuracy and reliability of the proposed criterion, the formalised elastoplastic model has been analysed by using finite element program package ANSYS, the local elastoplastic stress-strains are estimated by post processing the developed model. A summary of predicted and experimentally reported of maximum axial stresses are illustrated in Fig. 2. Generally in the "identical" correlation of Fig. 2, all data points should lie along the 45 degree solid line, but in this paper the predicted stresses are within the factor-of-two scatter band figured by the dashed lines (Fig. 2). This correlation can be considered as a good agreement between the estimated and their experimentally reported counterparts.

References	Materials	Strain Path	Phase angle φ (deg)	λ = γa/εa	εa = Δε/2 (%)	γa = Δγ/2 (%)	σa = Δσ/2 (Mpa)	τa = Δτ/2 (Mpa)
[6]	304 Stainless Steel	Path A	----	----	0.25	----	184	----
		Path B	----	----	----	0.476	----	109
		Path C	0	2.0	0.25	0.476	184	109
		Path L	----	1.7	0.25	0.43	365	199
[7]	347 Stainless Steel	Path E	90	1.7	0.577	1.0	----	----
[8]	SNCM630 Steel	Path G	90	1.5	0.6	0.9	----	----
		Path K	90	0.45	0.576	0.262	----	----
[6]	1% Cr-Mo-V	Path C	0	4.0	0.51	2.05	288	314
		Path D	180	1.5	0.99	1.54	528	230
		Path F	45	1.5	1.01	1.55	634	360
		Path G	90	1.5	1.02	1.54	669	366
		Path G	90	4.0	0.51	2.07	625	366
		Path H	135	1.5	1.01	1.52	674	349

Table 2: Type of materials, loading paths with Stress and Strain value (Constant Strain Amplitude).

Ref.	Materials	Strain Path	Strain History						
[10]	45 Steel	Path C	εa = Δε/2 (%)	0	± 0.2	± 0.4	± 0.6	± 0.8	± 1	0
			γa = Δγ/2 (%)	0	±0.346	±0.693	±1.039	±1.386	±1.732	0
		Path E	εa = Δε/2 (%)	0	± 0.2	± 0.4	± 0.6	± 0.8	± 1	0
			γa = Δγ/2 (%)	0	±0.346	±0.693	±1.039	±1.386	±1.732	0
		Path F	εa = Δε/2 (%)	0	± 0.2	± 0.4	± 0.6	± 0.8	± 1	0
			γa = Δγ/2 (%)	0	±0.346	±0.693	±1.039	±1.386	±1.732	0
[11]	S45C	Path M	εa = Δε/2 (%)	-0.068	0.11	-0.15	0.15	-0.11	0.068	-0.068
			γa = Δγ/2 (%)	-0.80	0.61	-0.41	0.41	-0.61	0.80	-0.80
		Path N	εa = Δε/2 (%)	0	0.41	-0.41	0	0	0	0
			γa = Δγ/2 (%)	0	0	0	0	-1.26	1.26	0
		Path O	εa = Δε/2 (%)	0	0.68	-0.68	0	0.28	-0.24	0
			γa = Δγ/2 (%)	0	1.48	-1.38	0	-0.57	0.63	0
		Path P	εa = Δε/2 (%)	0.0	0.10	0.30	0.43	0.32	0.06	-.12*
			γa = Δγ/2 (%)	0.0	0.66	-0.66	0.27	1.0	-0.66	0.49*
			εa = Δε/2 (%)	-0.35	-0.43	-0.23	-0.05	0		
			γa = Δγ/2 (%)	-1.0	-0.47	0.84	-0.33	0		

* Continued in the following εa or γa line

Table 3: Type of materials, loading paths with Stress and Strain value (Variable Strain Amplitudes)
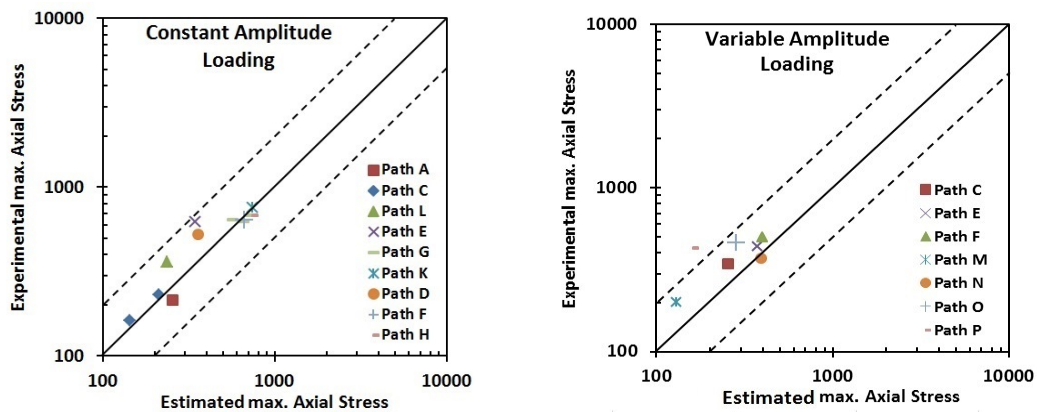

Figure 2: Error charts to compare the predicted local elastoplastic stresses with the experimentally reported.

According to the scenario described above, and based on the well-documented stress-strain paths of Fig. 3: first, all the local stress-strain sequences under different loading paths (constant amplitude) show the predicted curves agreed very well with the experimental investigation result and are located within a good manner. Second, for the applied variable amplitude multiaxial loading, the predicted local elastoplastic cyclic σ-ε and τ-γ plots are fully support and in very reasonable agreement with the experimental results as well as Jiang's model. To conclude, it can be pointed out that all results show that the formalized method is capable of predictions falling within accepted range and are proved to be most satisfactory.

However, a slight discrepancy can be observed between the predicted local stress-strain sequences and their experimental counterparts. These differences are mainly due to inconsistency in the microstructural features of materials [6] because Socie [6] proved that different materials show different sensitivities to additional hardening under multiaxial nonproportional loading and the amount depends on the microstructure and dislocation motion in the material during plastic deformation that can be determined from the laboratory test.
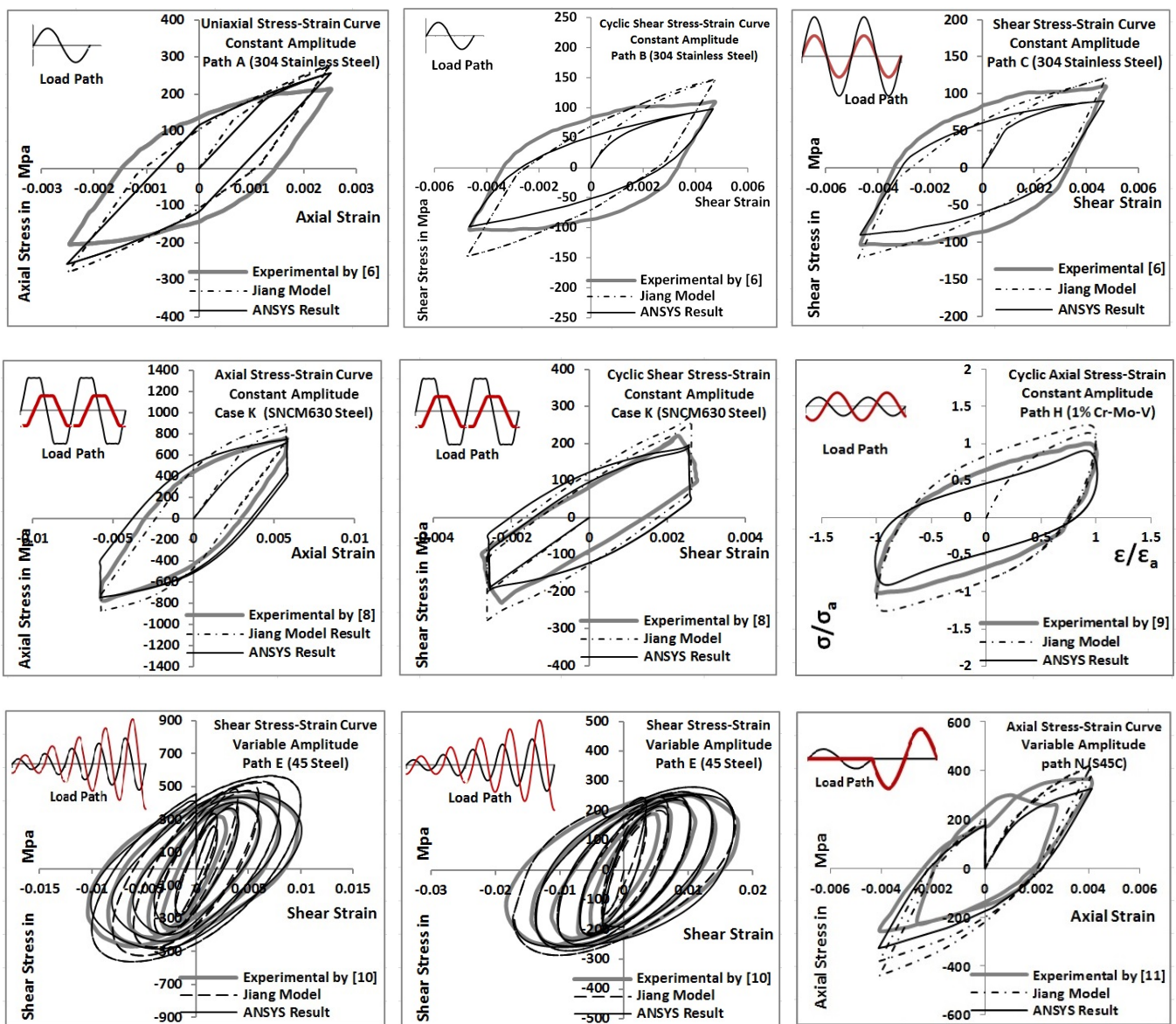

Figure 3: Compare the predicted Cyclic stress-strain relationship with the experimental reported and result of Jiang's Model

CONCLUSION

In this paper, various phenomena in relation to the elastoplastic stress-strain path of some materials under a complex system of cyclic loading has been modeled and studied particularly when the multiaxial displacement does not increase/decrease in a proportion (constant amplitude) but changes in a different manner (variable amplitude), the results are presented and discussed. The following conclusions can be drawn:

1. According to the comparison and exercise, it can be assumed that the predicted local stress-strain sequences are located within a closest range and a similar manner compared with their experimentally reported counterparts and Jiang's model. This is attributed to the fact that the formalised model is in a good agreement for all investigated loading paths and amplitudes.

2. A slight difference can be observed between the estimated curves and others under non-proportional loading case mainly probably due to non-proportional additional hardening. Socie [6] reported that materials have responded with additional hardening under nonproportional loading in contrast of proportional case, and the amount of additional hardening varies from none for some materials to more than double in some others based on the materials' microstructure [17].

3. The formalised model can be considered as a reliable relation with reasonable accuracy developed between monotonic tensile properties and uniaxial/multiaxial fatigue assessment of engineering materials. That serves to provide fast fatigue problem solution without involving time and cost in fatigue test. In contrast, Jiang's criteria require uniaxial and torsional fatigue data to determine material constants from experimental fatigue investigation.

4. The proposed elastoplastic models can be used to analyse and describe cyclic behavior of various metallic materials under different loading paths and amplitudes.

5. As briefly verified in the previous sections and in the light of accurate results and well agreements obtained from considering unnotched model, the subsequent target steps is extending into investigation of notched model and verify the accuracy and reliability of model with the data sets reported by technical literature [16].

6. Success in providing a model simulation to accurately estimate elastoplastic stress-strain property of materials, and by taking full advantage of the Modified Manson-Coffin Curves [5], fatigue lifetime of a component can be correctly estimated. That will be outlined in the next steps of this research program.

ACKNOWLEDGEMENTS

REFERENCES

[1] Shang, D.-G., Wang, D.-J., Yao, W.-X., A simple approach to the description of multiaxial cyclic stress-strain relationship. International journal of fatigue , 22(3) (2000) 251-56.

[2] Jiang, Y., Sehitoglu, H., Modeling of cyclic ratchetting plasticity, part I: development of constitutive relations. Journal of Applied Mechanics , 63(3) (1996) 720-25.

[3] Savaidis, A., Savaidis, G., Zhang, C., Elastic–plastic FE analysis of a notched shaft under multiaxial nonproportional synchronous cyclic loading. Theoretical and Applied Fracture Mechanics, 36(2) (2001) 87-97.

[4] Susmel, L., A simple and efficient numerical algorithm to determine the orientation of the critical plane in multiaxial fatigue problems. International Journal of Fatigue, 32(11) (2010) 1875-1883.

[5] Susmel, L., Multiaxial notch fatigue, Elsevier: Woodhead Publishing Limited (2009).

[6] Socie, D., Multiaxial Fatigue Damage Models. Journal of Engineering Materials and Technology, 109(4) (1987) 293-98.

[7] Hoffmeyer, J., Doring, R., Seeger, T., Vormwald, M., Deformation behaviour, short crack growth and fatigue livesunder multiaxial nonproportional loading. International journal of fatigue, 28(5) (2006) 508-520.

[8] Han, C., Chen, X., Kim, K.S., Evaluation of multiaxial fatigue criteria under irregular loading, International Journal of Fatigue, 24(9) (2002) 913-22.

[9] Kanazawa, K., Miller, K.J., Brown, M.W., Cyclic Deformation of 1% Cr-Mo-V Steel Under Out-Of-Phase Loads. Fatigue of Engineering Materials and Structures , 2(2) (1972) 217-28.

[10] Shang, D.-G., Sun, G.-Q., Deng, J., Yan, C.-L., Multiaxial fatigue damage parameter and life prediction for medium-carbon steel based on the critical plane approach, International Journal of Fatigue, 29(12) (2007) 2200-2207.

[11] Kim, K.S., Park, J.C., Lee, J.W., Multiaxial fatigue under variable amplitude loads. Journal of engineering materials and technology , 121(3) (1999) 286-293.

[12] Kim, K.S., Chen, X., Han, C., Lee, H., Estimation methods for fatigue properties of steels under axial and torsional loading. International journal of fatigue, 24(7) (2002) 783-793.

[13] Lee, Y.-L., Pan, J., Hathaway, R., Fatigue Testing And Analysis: Theory and Practice. Burlington: Elsevier, (2005).

[14] ANSYS, 2010. ANSYS. [Online] (13) Available at: "http://www.ansys.com" .

[15] Socie, D.F., Marquis, G.B., Multiaxial Fatigue. Warrendale: Society of Automotive Engineers, Inc. (2000).

[16] Susmel, L., Taylor, D., Estimating Lifetime of Notched Components Subjected to Variable Amplitude Fatigue Loading According to the elastoplastic Theory of Critical Distances. Journal of Engineering Materials and Technology, 137(1) (2015) 011008-1-15.

[17] Doring, R., Hoffmeyer, J., Seeger, T., Vormwald, M., A plasticity model for calculating stress–strain sequences under multiaxial nonproportional cyclic loading. Computational materials science, 28(3) (2003) 587-96.

A brief review of pond residence time studies

Mahshid Golzar
University of Sheffield
mgolzar1@sheffield.ac.ut.uk

ABSTRACT. Vegetation has a significant effect on the purifying processes in storm-water ponds. As pond hydrodynamics are also strongly affected by vegetation, it is necessary to understand flow and mixing processes in vegetated ponds for effective treatment design. In this paper the Residence Time Distribution (RTD) and related indices are discussed, and selected recent field and laboratory studies on vegetated ponds are reviewed. Selected RANS CFD (Reynolds-averaged Navier–Stokes Computational Fluid Dynamics) studies, which investigate pond geometry, are outlined. Those studies which investigate the effects of vegetation are divided into two types, first those which consider it as bed roughness or a retarding force, and second, those which consider it as a flow zone. The conclusions from the first approach are that it is sufficient to predict average hydraulic features for flood studies but insufficient for investigating mixing effects of vegetation. Recent publications have suggested that the second approach, i.e. considering vegetation as a porous media, may be more suitable. However, the most recent study highlighted certain limitations, as well as providing some preliminary suggestions for overcoming them. This discussion reinforces the need for further comprehensive research into this, and alternative, approaches.

KEYWORDS. Pond; Vegetation; RTD; CFD; Tracer Study.

INTRODUCTION

Storm-water runoff typically contains a wide range of pollutants that can potentially impose negative impacts on the environment. Ponds, often supplemented with wetland plantings, are installed to treat storm-water. These ponds have short retention times, typically just a few days, and provide peak attenuation and enhancement of storm-water quality [18]. Well-designed storm-water ponds moderate negative environmental impacts and reduce the level of pollutants to below the regulatory limit. Vegetation provides the appropriate environment for bacteria, and so enhances the treatment. The flow path, dead zones and shear layers that form in ponds, i.e. the hydrodynamics, are also highly affected by vegetation. To design a pond for effective treatment requires an understanding of flow patterns through vegetated and open parts, as well as the interaction between them.

A considerable number of studies have been done on quantifying and understanding the hydrodynamics of ponds with and without considering the effects of vegetation. These studies are predominantly based on the application of 2D and 3D Reynolds-averaged Navier-Stokes (RANS) Computational Fluid Dynamics (CFD) models, with some laboratory and field

monitoring programmes. The aim of this paper is to review the most significant achievements related to residence time studies in irregular shaped ponds and wetlands; constructed wetlands are not considered in this study.

THE RESIDENCE TIME DISTRIBUTION (RTD) AND RELATED METRICS

A convenient way to investigate the hydrodynamic behaviour of a pond, wetland or any tank with inlet and outlet is to study the time that the fluid spends in it. The Residence Time Distribution (RTD) shows the distribution of travel times in response to an instantaneous injection; the area under the curve equals unity by definition. The curve of dye concentration at the outlet versus time is identical to a frequency distribution of residence time [1]. Typical types of RTDs and Cumulative RTDs are shown in Fig. 1.
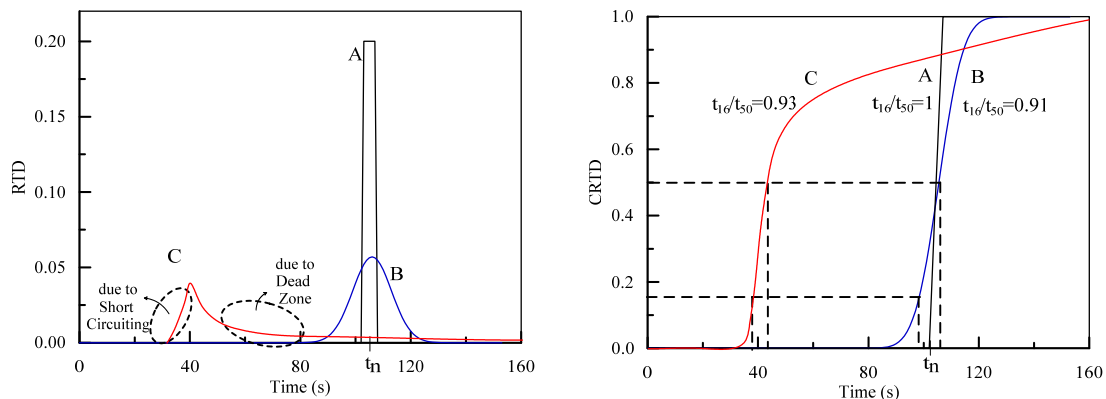

Figure 1: Typical RTDs, & CRTDs, A) plug flow, B) Gaussian spread and C) arbitrary mixing.

Several parameters have been defined to quantify pond performance. The Nominal Residence Time (t_n) [18, 1] is calculated as the ratio of pond volume to inlet discharge, assuming that flow moves through the pond as plug flow, i.e. all the inlet flow is distributed evenly over the width of the pond and all the flow travels at a similar velocity (Fig. 1, case A). However, the assumption of plug flow is not valid in most real situations, because as mentioned by Thackston et al. [1] "the concept of plug flow assumes that there is no mixing or diffusion as the wastewater moves through the pond". Unsteady flow rates, wind, inlet and outlet geometry effects and shear stresses due to boundary roughness at the sides and bottom, all act to cause dispersion in natural ponds. Dispersion causes a proportion of water to exit earlier than t_n and some to exit later, deviating from plug flow. The spread of the base of the RTD is a manifestation of dispersion, Fig. 1. cases B and C. Spread or dispersion can be quantified by the standard deviation.

One factor which causes deviation from plug flow is the presence of dead zones (also known as stagnation and recirculation zones). Thackston et al. [1] explained that any flow entering dead zones would be recirculated due to recirculation currents and have less than average velocities towards the outlet and hence a longer residence time. Although a high percentage of suspended solids may be removed in these locations, they have an adverse effect on treatment efficiency as their volume is unavailable to the mean flow and hence the mean residence time for most of the inflow decreases. Dead zones usually occur in hydraulically rough areas, corners, behind baffles or obstructions.

The reverse of the dead zone is short-circuiting, which has no precise technical definition [1] but which causes a significant part of flow to exit much earlier than t_{mean} or t_n. Ta and Brignal [3] used the ratio of t_{16} over t_{50} as a measure of short-circuiting ($S=t_{16}/t_{50}$), where smaller values of S suggest less occurrence of short-circuiting. But, as is discussed by Stovin et al. [4], in the case of plug flow S would be equal to one despite the fact that there can be no short-circuiting in this condition (Fig. 1). Persson [5] suggested using t_{mean} instead of t_{50} in this formula, whereas Stovin et al. [4] proposed t_{50}/t_n. Case C in Fig. 1 demonstrates the effects of both short-circuiting (first arrival times $<< t_n$) and dead zones (a long tail on the RTD with some residence times well in excess of t_n).

All the above mentioned features of imperfect hydrodynamic behaviour [6] cause the actual travel time to deviate from the nominal travel time. To quantify the degree of imperfection of flow, several authors have tried to provide an efficiency index which in essence compares the actual and the nominal travel times, e.g. Thackston et al. [1] defined t_{mean}/t_n as the hydraulic efficiency where Persson et al. [2] named this ratio as the effective volume and developed another index for the hydraulic efficiency as the ratio of t_p (time of peak concentration occurrence) over t_n.

The aim of the current research project is to use CFD to accurately characterise the RTDs of real storm-water ponds, and – in particular – to focus on properly representing the effects of vegetation. The following review highlights the key CFD studies relating to pond residence times, most of which have focused on pond geometry and neglected vegetation. As the development of a CFD-based modelling methodology that includes vegetation effects needs to be underpinned by a good understanding of the physical processes, relevant field and laboratory studies are briefly introduced; in particular, those that might provide suitable data for model development and validation are highlighted. The CFD studies to be discussed here are RANS models; other CFD approaches such as lattice Boltzmann and Large Eddy Simulation may also be relevant, but do not appear to have been practically implemented in pond studies to date.

FIELD AND LABORATORY STUDIES

A tracer study on a 7 ha vegetated maturation pond was done by Espinoza and Rengel (cited by Alvarado et al.) [7, 8]. The latter developed a 3D CFD RANS model with k-ε closure in ANSYS Fluent 6.3, using the former's field data for validation. The maturation pond was part of the largest wastewater facility in Ecuador. The total surface area of the system was 45 ha with a nominal residence time of 12 days. In the tracer study the RTD was produced by injecting a pulse of Rhodamine WT and the fluorescence concentration was measured for 30 days. It was seen that the majority of the tracer left the pond in the first 30 minutes, making a short circuit between the inlet and the outlet, which were both placed on the same side of the pond. A minor but visible quantity of tracer remained in the corner closest to the inlet pipe, indicating a stagnant zone. There were two peaks in the tracer record at the 2nd and the 4th hour of recording. An unsteady CFD model using the transient flow equation (species transport model) was run to simulate the first three days of the field tracer study. The main short-circuiting effects were reproduced well. However, there was no effort to model the vegetation and this may account for some discrepancies between the CFD and experimental data.

Tsavdaris et al. [9] studied a vegetated pond receiving road runoff with an area of 51×26 m² and the capacity of 304 m³ comprising two basins with a raised berm between them. The basins were planted with two types of emergent plants: (i) Phragmites australis (P.A) and (ii) Typha latifolia (T.L). Seven storm events were monitored with the highest Q=0.064 m³/s. Vegetation cover was measured in 0.5 m² quadrats and plant diameters of 0.01 and 0.035 m were measured for (P.A) and (T.L) respectively. A laboratory study in a 6×0.29 m flume with a slope of 0.004 with two discharges of 0.0077 and 0.0174 m³/s was also done. Emergent vegetation was simulated using stiff bamboo sticks with identical diameters to those observed and surveyed in the field study. They used the lab data to validate a CFD model (explained later under Tsavdaris et al. [10]) which used porous media to model the vegetation.

Shucksmith [11] investigated flow within emergent and submerged Carex grown for a period of 7 and 26 weeks in a 14.48×0.6 laboratory channel with a slope of 0.00123. Tracer studies were done at 5 flow rates ranging from 0.00919 to 0.02942 m³/s. The compiled data from this study was used subsequently by other researchers to validate CFD models. Hart et al. [12] is another source of potentially-useful experimental and field data.

GEOMETRY EFFECTS IN CFD STUDIES

Several 2D CFD modelling studies have been done to investigate different pond geometries. In these studies the vegetation was typically not considered, indeed the ponds were modelled as empty tanks. As an example, Persson et al. [2] provided a reasonably comprehensive review of geometry effects. They assessed the hydraulic efficiency of 13 pond geometries, with 2D models using Mike 21, a RANS CFD model with k-ε turbulence closure. They found that elongated and baffled systems provided very high hydraulic efficiency, i.e. close to plug flow. They also demonstrated the significant effect of a subsurface berm or an island which could improve the hydraulic performance by decreasing short-circuiting [5].

MODELLING VEGETATION IN CFD STUDIES

In order to take in to account the effect of vegetation on the flow field, different approaches can be found in the literature. Some have simply defined a roughness factor and others have used more complicated models, which are going to be discussed in this section.

Vegetation as a Boundary Condition

Some researchers have considered vegetation only as a bed roughness effect and tried to model it by assigning very high friction factors like Manning's *n*. Manning equation is a 1D open channel steady uniform flow equation, determining average hydraulic characteristics of flow based on an estimated friction factor, Eq. (1).

$$v = \frac{1}{n} R_b^{2/3} s^{1/2}$$ (1)

in which, *n* is Manning's factor, *v* is the average velocity, R_b is the hydraulic radius and *s* is the slope of the channel. It appears that the first efforts to estimate the value of n for vegetated channels were reported by Chow [19], assigning values between 0.005 to 0.1 for low to very high density of vegetation.

Somes et al. [13] gathered vegetation distribution, basin bathymetry, and measurements of flow velocities of the Monash University Research Wetland (MURW), an irregular constructed wetland with emergent macrophytes on its fringes. Tracer studies were not done due to recirculating of water from the outflow. A 2D Mike 21 model was used and different values of Manning's *n* (from 0.05 to 1.0) were allocated to each vegetation type. The *n* values were calibrated by visually comparing the measured and recorded flow vectors and the flow patterns they formed. Testing different friction values they concluded that the model was relatively insensitive to changes in friction, and this was attributed to the fact that the low velocities create small friction forces. In fact they assumed both submerged and emergent vegetation could be represented using different bed roughness values. This approach could be sufficient for specific purposes such as flood studies to predict the flow depth, but in order to predict mixing processes it is necessary to investigate the flow behaviour within the vegetation. It should be mentioned that the field part of this study may represent the most comprehensive study done to date to map a pond's internal flow field.

Vegetation as an Obstacle

Another approach to model the effect of vegetation is to consider it as an obstacle which exerts a retarding drag force on flow. There are some studies trying to find drag coefficient or to define a mathematical model based on drag coefficient to represent the effect of vegetation as a block in front of flow. Kadlec [14] assessed a number of proposed relations for taking to account the effect of vegetation and concluded that for emergent vegetation, open channel equations such as Manning's should not be used because they apply to situations where bottom drag is controlling. Instead he proposed to use drag force to represent the effect of emergent vegetation where vegetated drag controls. Although this study clarified the important effects of vegetation on flow field, the proposed 'solid block' approach does not help in terms of clarifying mixing effects within the vegetation.

Vegetation as a Flow Zone

Flow behaviour within the vegetated parts is considerably different from its behaviour through open parts, in such a way that cannot be expressed only by friction or retarding force. Features such as residence time, short-circuiting, dead zone and also all the mixing coefficients cannot be estimated unless the vegetation can be modelled as a different flow zone from open parts of the pond. A new approach has emerged in recent years, which considers the vegetation as a porous media. The porous media concept allows for flow movement within the vegetation and the resulting mixing effects may potentially be modelled and investigated.

Saggiori [15], using 2D and 3D k-ε RANS CFD models in ANSYS Fluent 12, modelled vegetation as a "Porous Zone". In this approach an additional source term is added to the Navier-Stokes equation Eq. (2). This additional source is a force representing the effects of porosity in the flow direction. This force is computed by Eq. (3), consisting of viscous and inertial parts, where *ρ* is density, *μ* is dynamic viscosity, u is velocity in the x direction and *α* and C_2 are estimated based on Eq. (4) and Eq. (5) respectively (Ergun [16]).

$$\frac{\partial \rho u u}{\partial x} + \frac{\partial \rho v u}{\partial y} = -\frac{\partial p}{\partial x} + \frac{\partial \tau_{xx}}{\partial x} + \frac{\partial \tau_{xy}}{\partial y} + F_x$$ (2)

$$F_x = -\left(\frac{\mu}{\alpha} u + C_2 \left(\frac{1}{2} \rho u |u| \right) \right)$$ (3)

$$\alpha = \frac{d^2}{150} \frac{\phi^3}{(1-\phi)^2}$$ (4)

$$C_2 = \frac{3.5}{d}\frac{(1-\phi)}{\phi^3}$$
(5)

These models were validated with experimental data from Shucksmith [11] and showed that the porous media approach resulted in velocity profiles which were consistent with experimental ones, see Fig.2. In addition, simulated RTDs, representing preliminary concentration profile predictions, showed promising comparability with the laboratory measurements.
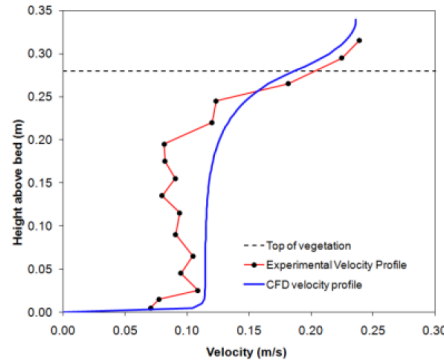

Figure 2: Comparison between experimental data and CFD data, 26 weeks; Q=29.5 l/s (from Saggiori [15])

Tsavdaris et al. [10] used two strategies for the CFD modelling of vegetation in ponds, (i) directly replicating individual vegetation elements within the computational domain, and (ii) using porous media. By comparing the velocity profiles resulting from laboratory study and modelled in ANSYS Fluent 12.1, they concluded that the first approach was much more accurate than the porous configurations in predicting turbulent flow within the vegetation. However, it should be noted that the direct representation of individual vegetation elements is too computationally expensive to scale up for application to real pond systems. Tracer studies were not done in this research.

Sonnenwald et al. [17] undertook a sensitivity analysis of the porous media approach using ANSYS Fluent 14.5. They showed that the results were highly sensitive to C_2 and insensitive to $1/\alpha$. CFD model was validated using Shucksmith's [11] laboratory data. Comparing particle tracking results with experimental solute traces showed that using the Ergun equation to estimate $1/\alpha$ and C_2 may not be suitable, instead estimating C_2 by balancing gravity and drag forces was suggested. They explained that turbulence around vegetation is generated by two factors: (i) the shear layer at the boundary between the vegetated and open flow; and (ii) by wake effects of water passing the stems. By assessing the submerged vegetation model, they concluded the shear layer part (which is a result of velocity difference) was correctly modelled but the wake effect was not. This was attributed to the lack of a source of turbulence within the porous zone. Their suggestion was to manually set the k and ε values for the porous zone to simulate the additional turbulence. They stated that it might be possible to empirically estimate these values based on vegetation characteristics.

DISCUSSION

Velocities produced in real ponds are usually much smaller than those considered in most of the laboratory investigations. This can make the conclusions unrepresentative of what is exactly happening in the ponds. Also, in most of the CFD modelling research, k-ε models are used in order to model the produced turbulence within the vegetation; these models assume that the Reynolds stress is the same in all the three dimensions. This assumption may not be true for some conditions, particularly for vegetation. In addition, a porous media approach may not be appropriate to model all different vegetation patterns, as there are many different vegetation patterns grown in ponds and also they tend to change from one season to another.

The present research is at a very early stage. Many relevant literature sources have not been discussed here. In addition, it is acknowledged that alternative model frameworks, such as lattice Boltzmann (which can potentially provide detailed information about flow behaviours e.g. wake effects associated with vegetative flows), need to be considered in the next phase of this study.

CONCLUSIONS

An RTD describes and quantifies flow patterns and mixing processes within vegetated ponds. Most ponds do not have ideal plug flow; instead they are characterised by complex mixing processes, for example dead zones and short-circuiting. A range of field, lab and CFD studies, from simple 2D ones to comprehensive investigations of flow within the vegetation, were reviewed. Among different approaches for modelling vegetated ponds, using porous media has been introduced as the most appropriate approach to date. This approach makes it possible to predict RTD indices and hydrodynamic flow features including velocity profiles. However, further investigation is needed to produce a general model which can completely represent the turbulence generation and other hydrodynamic characteristics of flow within the vegetation.

REFERENCES

[1] Thackston E. L., Douglas Shields. F., Schroeder, P. R., Residence time distributions of shallow basins, Journal of Environmental Engineering, 113(6) (1987) 1319-1332.

[2] Persson J., Somes, N. L. G., Wong, T. H. F., Hydraulics efficiency of constructed wetlands and ponds, Water science and technology, 40(3) (1999) 291-300.

[3] TA, C. T., Brignal, W. J., Application of computational fluid dynamics technique to storage reservoir studies, Water science and technology, 37(2) (1998) 219-226.

[4] Stovin, V. R., Grimm, J.P., Lau, S.-T. D., Solute transport modelling for urban drainage structures, Journal of Environmental Engineering, 134(8) (2008) 640-650.

[5] Persson, J., The hydraulic performance of ponds of various layouts, Urban Water, 2(3) (2000) 243-250.

[6] Persson, J., Wittgren, H. B., How hydrological and hydraulic conditions affect performance of ponds, Ecological Engineering, 21(4) (2003) 259-269.

[7] Sreepriya, V., Durazno, G., Nopens, I., Hydraulic assessment of waste stabilization ponds: Comparison of computational fluid dynamics simulations against tracer data, MASKANA, 2(1) (2011) 81-89.

[8] Alvarado, A., Sreepriya, V., Goethals, P., Nopens, I., A compartmental model to describe hydraulics in a full-scale waste stabilization pond, Water research, 46(2) (2012) 521-530.

[9] Tsavdaris, A., Mitchell, S., Williams, B.J., Computational fluid dynamics modelling of different detention pond configurations in the interest of sustainable flow regimes and gravity sedimentation potential, Water and Environment Journal, (2014).

[10] Tsavdaris, A., Mitchell, S., Williams, B. J., Use of CFD to model emergent vegetation in detention ponds, ARPN J. Eng. Appl. Sci., 8(7) (2013) 495-503.

[11] Shucksmith, J., Impact of vegetation in open channels on flow resistance and solute mixing, PhD Thesis University of Sheffield, (2008).

[12] Hart, R., Tiev, V., Stovin, V., Lacoursière, O., Guymer, I., The effects of vegetation on the hydraulic residence time of stormwater ponds, 19th IAHR-APD Congress, (2014).

[13] Somes, N., Warwick, L.G., Bishop, A., Wong, T. H. F., Numerical simulation of wetland hydrodynamics, Environment International, 25(6) (1999) 773-779.

[14] Kadlec, R. H., Overland flow in wetlands: vegetation resistance, Journal of Hydraulic Engineering, 116(5) (1990) 691-706.

[15] Saggiori, S., CFD modelling of solute transport in vegetated flow, Master's thesis University of Sheffield, (2010)

[16] Ergun, S., Fluid flow through packed columns, Chem Eng. Prog, 48 (1952) 89-94.

[17] Sonnenwald, F., Stovin, V., Guymer, I., Fesibility of the porous zone approach to modelling vegetation in CFD (Submitted to ISH34, Poland).

[18] Shilton, A., Pond Treatment Technology, first ed., IWA, London, (2006).

[19] Chow, V. T., Open Channel Hydraulics, first ed, McGraw-Hill Book Company,Inc; New York (1959).

Modelling Split-Hopkinson pressure bar tests on quartz sand

A. D. Barr, S. D. Clarke, M. Petkovski, S. E. Rigby
The University of Sheffield
a.barr@sheffield.ac.uk

ABSTRACT. FE modelling of a confined split Hopkinson pressure bar (SHPB) test on dry quartz sand was carried out using LS-DYNA in order to assess whether Material Model 5 could replicate experimental results, which would enable a more detailed investigation of the stress state in SHPB specimen. Quasi-static test data was used to select the material model input, and the model SHPB was set up to replicate the experimental conditions. The results show that Material Model 5 replicates the volumetric response provided as input data, but fails to predict the shear response observed in the quasi-static experiments. This was found to be due to the model treating the shear modulus as a constant rather than it increasing with strain, a feature which makes the Material Model 5 unsuitable for modelling SHPB tests on sand.

KEYWORDS. LS-DYNA; Sand; One-dimensional compression; Strain rate.

INTRODUCTION

This research forms part of the Dstl-sponsored and QinetiQ-led Force Protection Engineering (FPE) research programme, which investigates protective materials and structures that can be used by military fortifications designers [1]. The underpinning research element of this programme aims to enhance the understanding of how materials used in FPE perform under a wide range of loading conditions. In order to make accurate predictions of the response of soils to blast and impact events, it is vital to have an understanding of the soil behaviour at very high pressures, and over a wide range of strain rates and ground conditions.

In previous work, the effect of strain rate on the behaviour of dry and partially-saturated sand was investigated at high stresses, seeking to clarify the existence of a strain-rate dependence [2]. Quasi-static one-dimensional compression tests on a fine quartz sand were carried out to axial stresses of 800MPa using the mac^{2T} multi-axial test rig at The University of Sheffield, alongside dynamic tests to 400MPa using a split Hopkinson pressure bar. Specimens were laterally confined using a steel loading box or steel ring to ensure one-dimensional test conditions, and lateral stresses were recorded to allow the three-dimensional stress state of the specimens to be analysed. Between strain rates of 10^{-3} s^{-1} and 10^{3} s^{-1} it was found that constrained modulus increased with strain rate, but little change in bulk modulus occurred: while the axial stress increased with strain rate, the radial stress measured at the specimen surface decreased. This was attributed to radial inertia within the specimen during the high-strain-rate split-Hopkinson pressure bar (SHPB) tests, which would indicate that the increase in stiffness was a structural effect rather than a strain-rate dependence in the sand. It is desirable to quantify this inertial effect, but this requires knowledge of the evolving stress state within the specimen during the SHPB test, which is very difficult to achieve experimentally. In this paper the Finite Element (FE) code LS-DYNA is used to

simulate a SHPB test on dry sand to investigate whether a simple soil material model can sufficiently model the soil behaviour to make analysis of the inertial effects possible.

FINITE-ELEMENT MODELLING OF SOILS

Modelling soils using FE methods usually involves treating the soil as a continuum with uniform bulk properties. In the last decade there has been a great increase in the use of Discrete Element Modelling (DEM), as originally proposed by Cundall and Strack [3], which considers the movement and behaviour of individual particles in the soil, and explicitly models the contacts between the particles [4]. These properties give DEM the potential to be used to research fundamental soil behaviour, but a detailed understanding of the inter-particle friction and particle fracture is also required to obtain accurate results, and computational limitations currently restrict its use to modelling small numbers of particles.

Since particles are not modelled explicitly in a continuum model, it relies on the material model to capture the important bulk properties, which can usually be attained using standard geotechnical tests. LS-DYNA has a number of built-in material models which can be used to model the behaviour of soil, varying from the simple definition of a compressibility curve and yield surface to more complex models incorporating pore water effects, strain softening and hardening and strain-rate effects [5]. Most studies in the open literature which involve soil modelling are related to buried explosive events [6-8], but LS-DYNA has also been used to model aircraft and spacecraft crashworthiness [9] and to assess DEM models of soil systems [10]. Most of these studies are not directly comparable, but it can be seen that models with a rigorously-defined soil material model are more likely to accurately predict the soil response, while models with less evidence of characterisation can be made to match a final deflection or a peak pressure, for example, but cannot accurately predict the response over the whole time or volume of interest.

To ensure that the sand material model used in this study is based on experimental results of soil behaviour, data from high-pressure quasi-static tests on the dry sand will be used to select the parameters used in an LS-DYNA material model. The material model will be used in a simulation of a SHPB test on the sand, and the predicted response compared with the experimental data. If the model and experimental data matches well, the model data can be investigated further with some confidence. If it does not, the model cannot be simply adapted to fit, instead another model will be selected which more closely captures the behaviour of the sand.

Variable	Description
ro	Initial density. [kg/m^3]
g	Elastic shear modulus. [Pa]
bulk	Bulk modulus, used to define the unloading response. [Pa]
pc	Tensile pressure cut off (< 0). [Pa]
eps1–eps10	Volumetric strain values corresponding to pressures p1–p10. Volumetric strain is given by the natural logarithm of relative volume. Negative in compression.
p1–p10	Pressure values corresponding to volumetric strains eps1–eps10. Positive in compression. [Pa]
a1, a2, a3	Constants used to create a quadratic fit yield function in J$_2$–P space.
vcr	Volumetric crushing option (boolean): 0: unloading dependent on unloading bulk modulus; 1: loading and unloading defined by the pressure-strain curve.

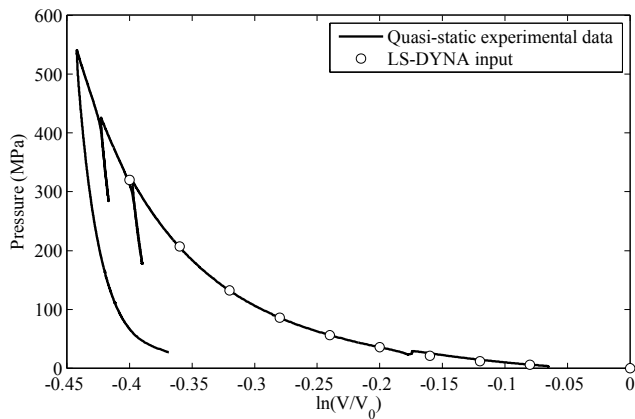Table 1: LS-DYNA Material Model 5 variables, in current model units.

Figure 1: Sand pressure–volumetric strain relationship used in LS-DYNA, derived from experimental quasi-static data.
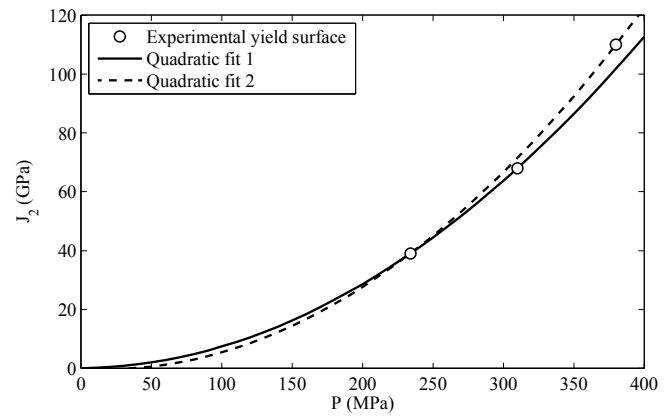

Figure 2: Shear strength relationship used in LS-DYNA, derived from triaxial tests on dry sand.

MATERIAL MODEL 5

LS-DYNA's Material Model 5 (*MAT_SOIL_AND_FOAM) is a simple pressure-dependent model designed for foams and soils which are confined within a structure [5]. Definition of the material requires the variables in Tab. 1, comprising of a compressibility curve, a shear strength function, shear and bulk moduli and a tensile cut-off. Material Model 5 has been used to successfully simulate contingency landings of the Orion capsule onto sand [9], and so it is worthwhile considering it before moving on to more complex models.

Compressibility

The variables `rho`, `p1–p10` and `eps1–eps10` define the compressibility of the soil, and were determined using the pressure–volumetric strain relationship from quasi-static one-dimensional compression tests on the dry sand. The sand was prepared at a dry density `rho` = 1500 kg/m³ and loaded to a pressure of 550 MPa using the mac²ᵀ test rig [2]. Ten pressure and volumetric strain pairs can be provided to the model, and these were chosen to describe the experimental curve to the maximum pressures experienced in the SHPB test, as shown in Fig. 1. The unloading bulk modulus `bulk` and the elastic shear modulus `g` can also be obtained from the one-dimensional compression tests, where the bulk modulus is the slope of the pressure-volumetric strain curve during unloading, and the elastic shear modulus can be calculated using the relationship

$$G = \frac{M(1-2\nu)}{2(1-\nu)} \tag{1}$$

where G is the shear modulus, M is the constrained modulus and ν is Poisson's ratio. Tests performed on dry FPE Sand provided values for the bulk and shear moduli of 22GPa and 13MPa respectively, using a Poisson's ratio of 0.3.

Shear strength

The variables `a0`, `a1` and `a2` are coefficients in the deviatoric perfectly-plastic function φ, which is defined as

$$\varphi = J_2 - \left(a_0 + a_1 P + a_2 P^2\right) \tag{2}$$

where J_2 is the second deviatoric invariant and P is pressure. This function can be fitted to experimental triaxial data by plotting a strength envelope in J_2–P space, as shown in Fig. 2. In these high-pressure triaxial tests the sand was loaded one-dimensionally in the mac²ᵀ rig, and then the lateral stresses were reduced to move the stress state towards the yield surface. Two possible quadratic fits are shown for the data, which use three known points on the yield surface and the origin, as the sand is cohesionless. 'Quadratic 1' was chosen to represent the surface, as it best represents the stress range in the SHPB tests, leading to the coefficients `a0` = 0, `a1` = 4.51 and `a2` = 0.693.

The tensile cutoff `pc` is required to be non-zero, so while the sand is cohesionless it is provided with a very small tensile strength `pc` = 0.001 Pa.
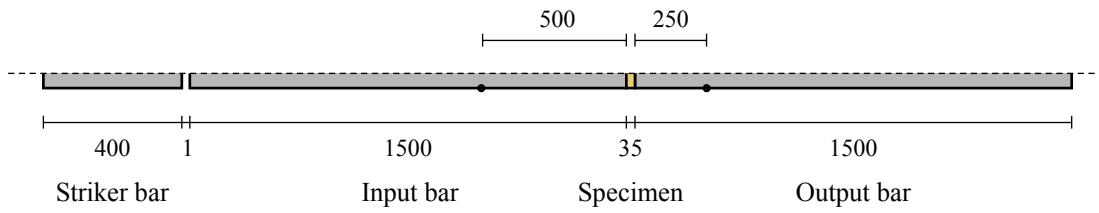
Figure 3: LS-DYNA model geometry and locations of strain gauge recordings.

SHPB MODEL

An axisymmetric FE model was set up to replicate the geometry of the SHPB test, as shown in Fig. 3. The stainless steel striker, incident and transmitter bars all have a diameter of 25 mm, a density of 7850 kg/m³, a Young's modulus of 168 GPa and Poisson's ratio 0.29, and are modelled using the material model `*MAT_ELASTIC`. The strain gauge readings from the physical experiment were used to assess the performance of the model, and so their positions are also noted on Fig. 3. The striker bar was given an initial velocity of 22.4 m/s to match the incident pulses experienced in the physical tests, and the sand specimen set up with an initial length of 35 mm. In the physical test the sand specimen is confined laterally by a steel ring, and so this is approximated here by restricting the nodes on the surface of the sand specimen from displacing laterally.

PERFORMANCE OF THE MODEL

The output of the model is first presented in terms of the axial stress–density behaviour of the sand specimen, as this is the main output of the physical tests. As shown in Fig. 4, the modelled sand has a much lower stiffness than both the quasi-static and dynamic specimens, indicating that it does not represent the sand behaviour well. The compressibility of the modelled sand (Fig. 5) shows that, while the input curve is followed closely, the maximum pressure in the sand exceeds the defined range, so that the compressibility is extrapolated linearly. The pressures generated in the model (400 MPa) far exceed the experimentally measured pressures (< 250 MPa), which suggests that the material is behaving in a fluid-like manner, with insufficient resistance to shear forces. This is confirmed by Fig. 6, which shows that the modelled sand deviates from the experimental response at low mean stresses and generates very little shear resistance, despite being far from the yield surface. Further investigation reveals that the shear modulus defined in the model does not increase as the soil compacts, as is expected, but remains constant throughout the test, as shown in Fig. 7. This causes the unrealistic shear behaviour observed in the modelled sand, and the associated error increases as the soil becomes compressed and the bulk modulus increases. As a result Material Model 5 is clearly not suitable for modelling a SHPB test on soil, and an alternative will have to be found which models the variation of shear modulus.
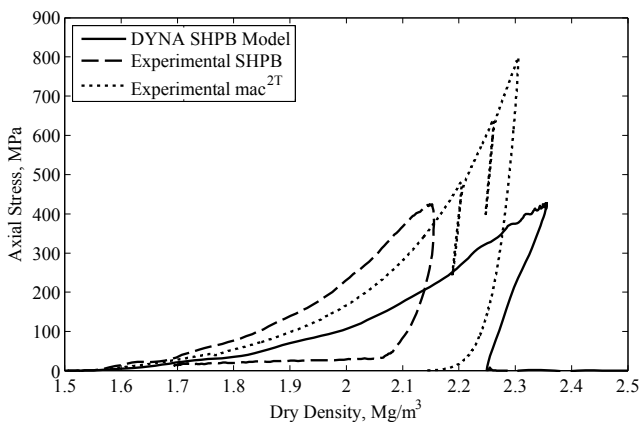

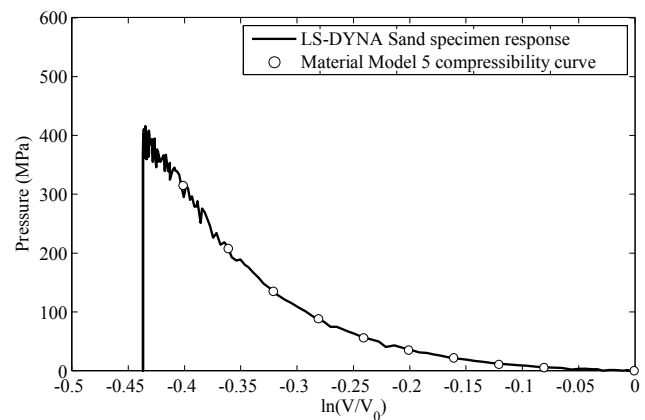Figure 4: Axial stress–density response of LS-DYNA specimen compared to experimental data.

Figure 5: Sand pressure–volumetric strain relationship as modelled by LS DYNA.
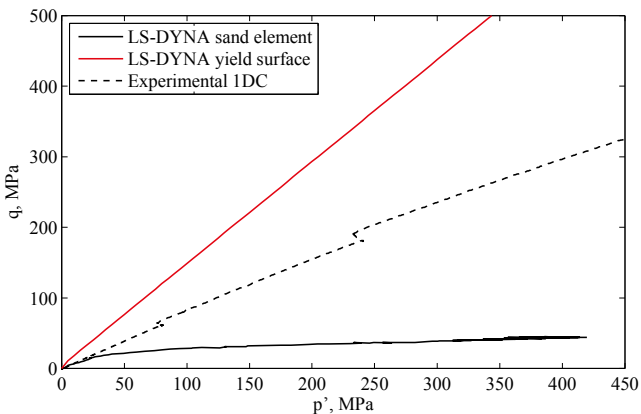
Figure 6: The shear response of the LS-DYNA specimen compared to experimental data and the model yield surface.
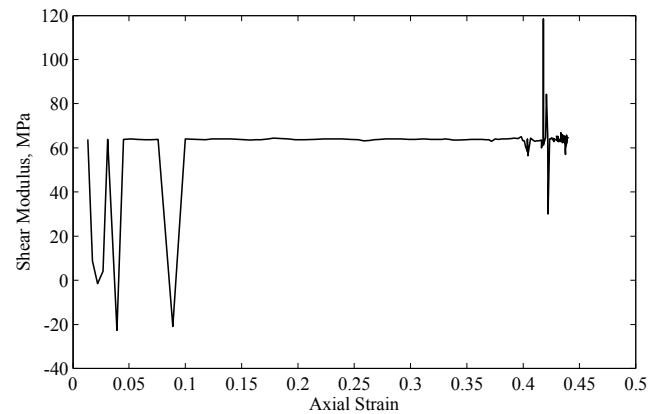

Figure 7: Variation of shear modulus with axial strain.

CONCLUSIONS

Finite Element modelling of a SHPB test on fine quartz sand was carried out using LS-DYNA in order to assess whether Material Model 5 could replicate the results from experimental tests, which would enable a more detailed investigation of the stress state in the sand specimen. Quasi-static test data was used to select the input data for the material model, and the model SHPB was set up to replicate the experimental conditions. The results show that Material Model 5 replicates the volumetric response provided as input data, but fails to predict the shear response observed in the quasi-static experiments. This was found to be due to the model treating the shear modulus as a constant rather than it increasing with strain, a feature which makes the Material Model 5 unsuitable for modelling SHPB tests on sand.

REFERENCES

[1] Warren, J., et al., Briefing: UK Ministry of Defence Force Protection Engineering Programme. Proceedings of the ICE - Engineering and Computational Mechanics, 166(3) (2013) 119-123.

[2] Barr, A.D., et al. Quasi-static and high-strain-rate experiments on sand under one-dimensional compression. in Hopkinson Centenary Conference. Cambridge, UK: Fraunhofer EMI. (2014).

[3] Cundall, P.A. and O.D. Strack, A discrete numerical model for granular assemblies. Geotechnique, 29(1) (1979) 47-65.

[4] O'Sullivan, C. Advancing geomechanics using DEM. in Geomechnanics from Micro to Macro. Cambridge, UK: Taylor & Francis Group, London. (2014).

[5] Hallquist, J.O., LS-DYNA keyword user's manual, in Livermore Software Technology Corporation (2007).

[6] Wang, J., Simulation of landmine explosion using LS-DYNA3D software: benchmark work of simulation of explosion in soil and air, , DTIC Document (2001).

[7] An, J., et al., Simulation of soil behavior under blast loading. International Journal of Geomechanics, 11(4) (2011) 323-334.

[8] Jayasinghe, L.B., et al., Computer simulation of underground blast response of pile in saturated soil. Computers & Structures, 120 (2013) 86-95.

[9] Heymsfield, E., et al., Assessment of soil modeling capability for orion contingency land landing. Journal of Aerospace Engineering, 25(1) (2010) 125-131.

[10] Fang, Q., et al., An algorithm for the grain-level modelling of a dry sand particulate system. Modelling and Simulation in Materials Science and Engineering, 22(5) (2014) 055021.

Seismic investigation of multi-storey RC frames retrofitted using a friction panel with different slip load distributions

N. Nabid, I. Hajirasouliha, M. Petkovski
University of Sheffield
nnabid1@sheffield.ac.uk, i.hajirasouliha@sheffield.ac.uk, m.petkovski@sheffield.ac.uk

ABSTRACT. The research focuses on the seismic performance of moment resisting reinforced concrete frames, retrofitted using friction-based passive control systems. To conduct the research, five different RC frames with different storeys (3, 5, 10, 15 and 20) were selected and their seismic responses with and without friction panels were investigated using non-linear dynamic analyses performed by DRAIN-2DX software. Selected frames were analyzed under six real and one synthetic spectrum compatible earthquake. The ratios of the inter-storey drift and roof displacement of the controlled system to the corresponding values in the bare frame were calculated for each case. To assess the overall behaviour of the proposed friction panels, two energy dissipation parameters, which are the main indicators of the efficiency of the system, were considered. In this study, five different lateral load patterns, including uniform, cantilever, triangular, inverted triangular, and storey strength proportional distribution were applied to the friction devices. To achieve the optimum design of friction panels, optimum values of slip load ratio (the ratio of the slip load to the storey strength) have been determined. The results indicated that, in general, up to a particular point increasing the slip load improves the behaviour of the controlled system, while further increase may reduce the efficiency of the proposed passive control system. It was shown that uniform and triangular distributions of the slip load were more effective than other distribution patterns in controlling the seismic responses of the selected RC frames. Using friction panels in RC frames has been proved to be an effective solution in terms of reducing the inter-storey drift and roof displacement regardless the size of the frame and seismic excitation characteristics.

KEYWORDS. Friction panels; Slip load; Distribution patterns; RC frames; Energy dissipation.

INTRODUCTION

P assive energy dissipaters have been considered as one of the most efficient and cost effective solutions in terms of concentrating damage in non-structural elements. In other words, the major part of the seismic energy input is damped through passive dampers, without any serious defects in the structural members. Passive dampers, which slip independently from any external sources of energy, are considered as displacement-dependent elements, and they can be easily replaced after severe earthquakes. Based on previous studies on different types of passive control systems, passive dampers are categorized in six major groups, including 1) Viscous fluid dampers, 2) Viscoelastic dampers, 3)

Metallic yield devices, 4) Tuned Mass Dampers (TMD), 5) Tuned Liquid Dampers (TLD), and 6) Friction dampers [1, 2, 3].

In general, Friction dampers are the most appropriate compared to the others in terms of damping capacity, which is used to improve the seismic performance of substandard systems. In other words, friction dampers have shown sustained performance under large number of cycles, which leads to rectangular hysteretic loops, and higher energy dissipation compared to other passive control devices. However, self-centering or energy dissipating damper is the only exception to this trend (Fig.1). In addition, friction devices are superior to other passive dampers in terms of being velocity and temperature-independent, low cost, ease of construction, and ability to be tuned to the characteristic of the structure.
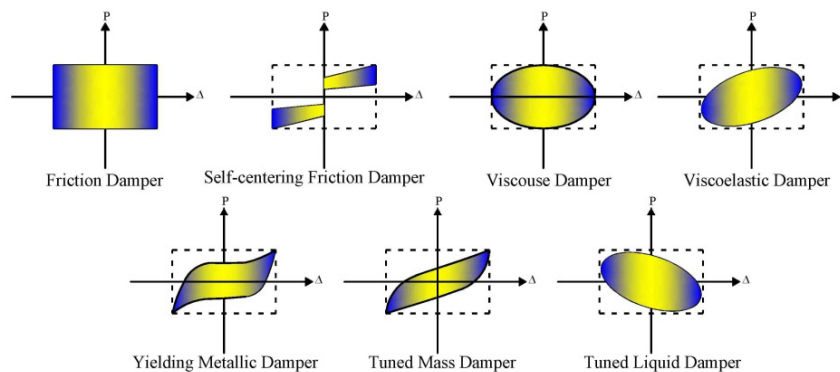

Figure 1: Force-displacement diagrams for passive control devices [4, 5, 6]

Friction-based control systems are classified as 1) Pall friction dampers, 2) Sumitomo dampers, 3) Slotted Bolted Connections (SBC) 4) Energy Dissipating Restraint (EDR) or self-centering dampers, 5) Limited Slip Bolted joints (LSB). Taking advantage from friction brake pads in automotive and mechanical engineering, Dr. Avtar Pall (1979) first proposed Pall friction dampers, which are appropriate for slender X brace steel frames, single diagonal and chevron bracing [7, 4]. Pall friction devices comprise of a series of steel plates clamped together using high strength bolts, which prevent compression bending at braces, and slip under predetermined load. Pall dampers have been proved to dissipate almost 80% of the input earthquake energy [8]. Later, an improved model of Pall dampers equipped by a T-section core plate was suggested by Wu (2005). The improved model made the first model cheaper and easier to be analysed because of simplicity of the construction [9]. Sumitomo metal industry proposed a uniaxial friction device made of stainless steel casing with pre-compressed internal springs and friction pads, which has been developed by Aiken and Kelly in 1990 in Japan. Results of testing a ¼ scaled-down 9-storey building controlled with these dampers showed a consistent and ideal Cloumb behaviour accompanied by 60% dissipated input earthquake energy. Afterwards, Constantinou and Reinhorn (1991) applied Sumitomo devices to seismic isolation systems of bridges to form the sliding interface [10]. The other friction devices, which apply Slotted Bolted Connections (SBC) in concentric braced frames, were proposed by Fitzgerald in 1989. The friction was defined based on steel sliding interface, however, a more stable steel-brass frictional behaviour was introduced by Grigorian and Popov (1993) [11, 1].

Flour Daniel Corp. proposed a more sophisticated friction device named Energy Dissipation Restraint (EDR) with self-centering capabilities provided by internal springs and end gap similar to Sumitomo devices [10]. EDRs are the only exception in friction-based control systems without a rectangular hysteresis loops. Their hysteretic behaviour depends on the characteristics of the device such as spring constant, gap size, core configuration and initial slip force [11, 1]. Pall and Marsh (1980) invented Limited Slip Bolted (LSB) joints based on brake lining pads for seismic controlling of large panel concrete structures. LSB joints are embedded in the contact lines of precast concrete walls in which they move relative to each other during earthquake, and the energy is dissipated through friction joints [12].

Concrete wall panels were first proposed by Nabih Youssef and Associates in order to seismic retrofit of a Rivera Library at the University of California at Riverside (UCR) [13]. Each precast concrete wall was connected to the lower beam with the bolted steel connectors and to the beam of the upper floor by three dampers bolted at the top of the panel. The energy was dissipated through the relative displacement of the adjacent floors due to seismic excitation. Afterwards, more valuable research was performed by Petkovski (2001) and Sasani and Popov (1997) on lightweight concrete panel equipped with friction dampers. Petkovski assessed the effectiveness of the friction panels on reducing some seismic responses of the controlled structures with different panel's characteristics (with opening, without opening and different thicknesses). In addition, he has proposed an optimum range for the ratio of the slip forces in the connections to the storey shear strength of the base frames [14, 15].

The intended goals of the current studies are to investigate the most appropriate slip load distribution pattern in terms of improving seismic behaviour, and to ascertain the optimum ranges for slip load ratios applied to 3, 5, 10, 15, and 20-storey RC frames. Studied frames are subjected to six real earthquake records including El-Centro, Imperial Valley, Cape Mendocino, Loma Prieta, Duzce, Northridge and one synthetic IBC spectrum compatible earthquake. For non-linear dynamic analyses using DRAIN-2DX software, three different element types, including inelastic beam and column (type 2), friction connection (type 4), and elastic panel (type 6) have been considered. Panel element is assumed to have eight displacement degrees of freedom, which account for five uncoupled deformation modes, and three rigid body modes at its four nodes [16]. The seismic responses, optimum range of slip load ratio, and the most appropriate slip force distribution pattern in terms of improving the seismic behaviour of the 10-storey RC frame with the characteristics shown in Fig.2 have been discussed in this research.
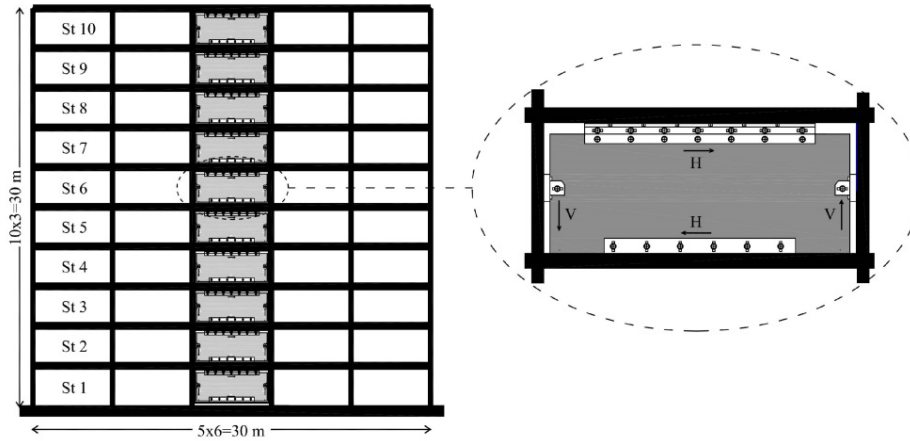

Figure 2: 10-storey RC frame with friction panels

FRICTION PANEL MECHANISM

As shown in Fig.3, friction damper consist of a concrete panel with four connections at its four sides. The friction mechanism is a simple panel-to-frame connection. It consists of two steel plates bolted at the top of the panel (external plates) and clamped together over a slotted steel plate anchored in the beam (central plate). Brass plates used at the friction surface (between the external plates and the central plate) were chosen on the basis of experimental evidence. A better slip/friction performance is obtained by steel-to-brass contact than by steel-to-steel [14]. The other panel-to-frame connections were designed to prevent both vertical and lateral movement of the panel with respect to the floor. Vertical support of the panel was provided by panel-to-column connections with horizontal slots, while horizontal support was supplied by connections between the panel and the floor. The latter connections have vertical slots to secure the movement in the friction connection, which is equal to the inter-storey drift [14].
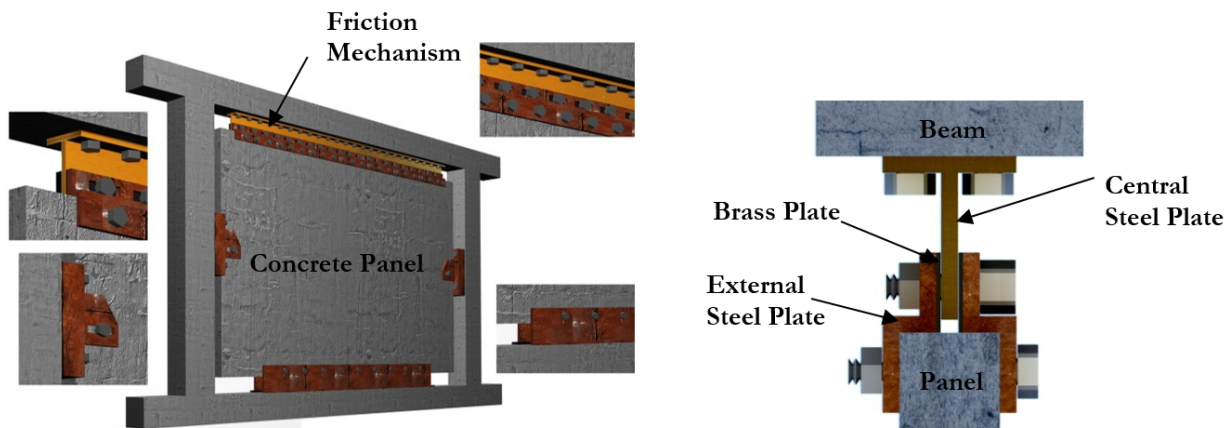

Figure 3: Friction panel and friction mechanism detailing.

SLIP LOAD DISTRIBUTION PATTERNS

S lip force in friction connections (Fs) is a main parameter that can be adjusted and tuned independently for each storey by controlling the clamping force in bolts. Such capability provides the possibility of different patterns for slip load distributions along the height of structures. For the case of cantilever distribution, an identical slip load threshold was considered in all stories, while for other patterns the values varied from one storey to the other. For uniform, triangular, and inverted triangular distributions, the loads increased from the top storey to the bottom based on a cumulative rule. However, for the storey strength proportional pattern, the slip load in each level was a constant coefficient of the same storey strength. Fig. 4 shows the different slip load distribution patterns used in this study.
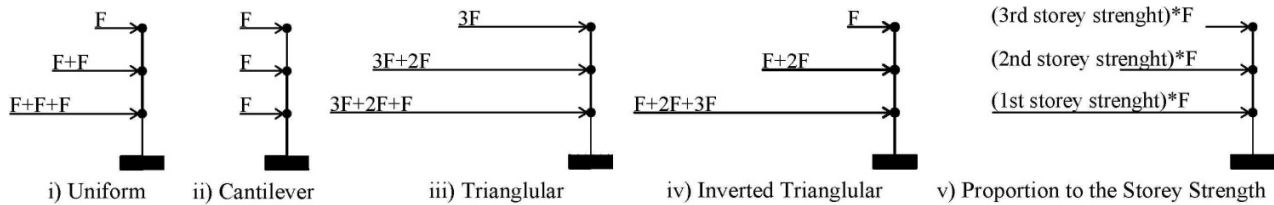

Figure 4: Schematic model of slip load distribution patterns

MAXIMUM INTER-STOREY DRIFT AND ROOF DISPLACEMENT RATIO

T he maximum drift ratio is defined as the ratio of the maximum drift in a frame with friction panels to the maximum drift in a bare frame with no panels. Therefore, the ratio starts from one for no slip load case (Fs=0), and reduces gradually by increasing the slip load until it remains steady or increases slightly as shown in Fig. 5. Such result was found to be independent from the seismic excitation characteristics, and the overall trend was similar for all seven earthquake records. It was observed that the reduction was more significant up to a certain slip force limit, and after that increasing the slip force did not have a considerable effect. Fig. 5 indicates that, for the 10-storey frame, the maximum decrease in drift ratio (up to 38% decrease) was relevant to the uniform and triangle distribution patterns, which occurred in the slip load ratio between 0.8 and 1.5. Among all, the inverted triangular distribution had the least impact on improving the structural responses of the frame. Similar results were obtained for 3, 5, 15, and 20-storey frames. The maximum roof displacement ratios also decreased considerably for all distribution patterns (up to around 42%) by increasing the slip force.
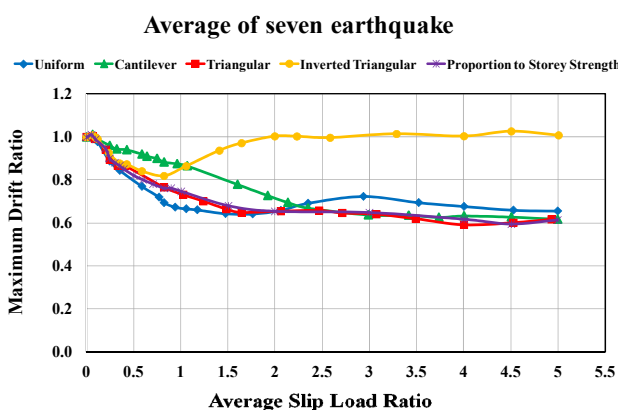
Figure 5: Variation of maximum inter-storey drift ratio
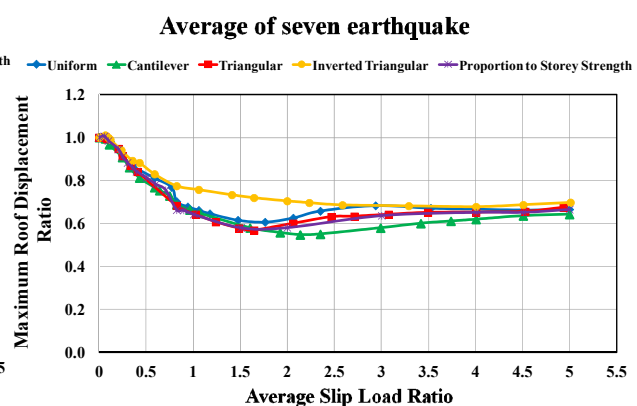
Figure 6: Variation of maximum roof displacement ratio

Fig. 6 illustrates that the most reduction in the 10-storey frame was observed for slip load range of 1.3 to 1.6. In addition, it is depicted that frames designed with the triangle and proportion to the storey strength slip load distributions performed better than others. Although after this slip load ratio range (1.3-1.6) cantilever pattern lead to more reduction, the most effective patterns are those which have the most impact within the optimum range. The overall trend of each seismic

response (maximum inter-storey drift and roof displacement) was similar for all size of the buildings and seismic excitations.

ENERGY DISSIPATED IN THE STRUCTURAL ELEMENTS (Rw1)

Rw1, the first energy dissipation parameter, is the ratio between the statistic work in the frame structural members equipped with friction dampers to the work in the members of the corresponding bare frame [14, 15]. This parameter represents the energy dissipation in the structural elements. The results indicate that Rw1 starts from one (for Fs=0) and reduces up to an average slip load ratio between 0.8 and 1.4, then it goes up by increasing the slip load and remains almost steady (Fig. 7). This trend implies the fact that the work in the frame elements first decreases by increasing the dissipated energy in friction panel, and it has been observed to be the same for all models regardless the slip load distribution and input earthquake excitation. The maximum drop was usually observed for triangle and uniform distribution (more than 60% drop). Besides, it is clear that proportional to the storey strength pattern has the same effect as the triangular one. Fig. 7 also shows that increasing the slip load ratio more than a limit (here around 1.0) would not lead to a better seismic performance. Although the range of optimum slip load ratio differs for different frame heights (for example, an optimum slip load range of 1.7-2.5 for 5-storey and 0.4-0.8 for 15-storey), similar trend were observed for all frames.

ENERGY DISSIPATED IN THE FRICTION CONNECTION (Rw2)

The second parameter, Rw2, is the ratio between statistic work of the friction loads in the upper supports of the panel, and the work carried out by damaging of the main structural members in the controlled structure [14, 15]. The Rw2 factor shows the energy dissipation level in the friction panels. Therefore, maximum Rw2 represents the optimum design solution. Fig. 8 illustrates that the Rw2 factor tends to zero for very low and very high slip forces (i.e. non-active dampers). The results imply that according to the different distribution patterns used for the 10-storey frame, Rw2 factor reaches its maximum value for a slip load ratio range of 0.8-1.4, which considered as the most effective domain to obtain the best control action. Also, Fig. 8 shows that the maximum energy dissipation of friction connections was observed in the frame designed with triangle and uniform distributions, which was in agreement with the previous response parameters (Fig. 5 and Fig. 6). The peaks of the Rw2 ratio indicated that friction connections dissipate the earthquake energy almost 6 or 7 times greater than main structural elements. In other words, friction panels account for increasing the energy dissipation capacity of the structure and, consequently, decreasing damage to the structural elements.
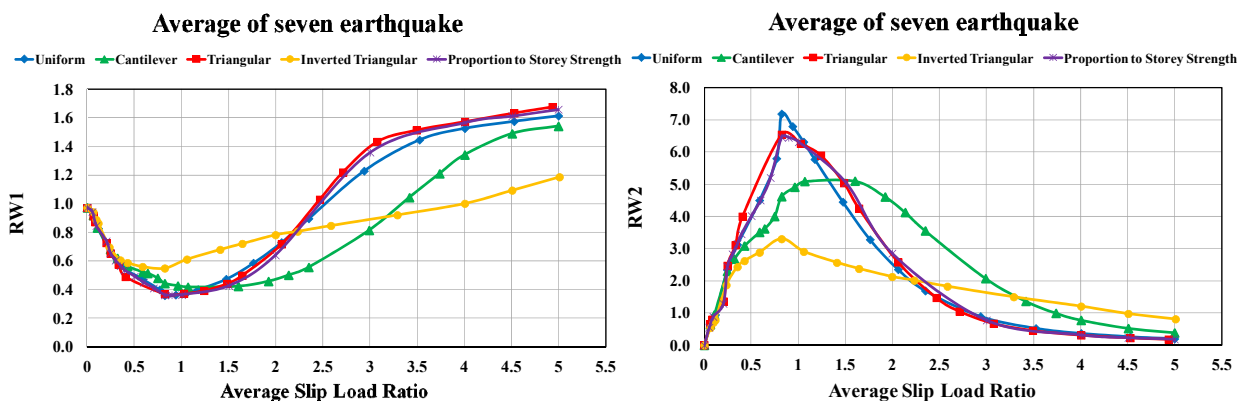

Figure 7: Energy dissipation RW1 for different slip load patterns

Figure 8: Energy dissipation RW2 for different slip load patterns

The results of this study, in general, show that the optimum designed friction-wall panels can significantly improve the seismic behaviour of deficient RC frames.

CONCLUSION

Using friction panels can lead to a significant improvement in some seismic responses (inter-storey drift and roof displacement) of the studied RC frames (3, 5, 10, 15, and 20-storey) by increasing the energy dissipation capacity of the systems. It was shown that, on average, friction panels can decrease the maximum inter-storey drift and maximum roof displacement of the 10-storey frame by up to 38% and 42%, respectively.

The overall results of all seismic responses, including the inter-storey drift and roof displacement for all studied frames indicated that uniform and triangle distribution patterns, in general, would lead to a considerably better seismic performance compared to the others. Triangle and proportional to the storey strength patterns have been observed to have the same effects on the structural responses. Inverted triangular pattern has shown as the least effective one on the seismic improvement. It was confirmed that, there is an optimum design range for the slip load ratios, which result in higher energy dissipation in the friction panels. This range was ascertained to be between 0.8 and 1.4 for a 10-storey friction-based controlled frame. However, the range would be decreased by increasing the height of the frame (for example, an optimum slip load range of 1.7-2.5 for 5-storey and 0.75-1.0 for 15-storey).

REFERENCES

[1] Sadek, F., Mohraz, B., Taylor, A. W., Chung, R. M., Passive Energy Dissipation Devices for Seismic Applications, Maryland, (1996).

[2] Moreschi, L. M., Seismic Design of Energy Dissipation Systems for Optimal Structural Performance, Virginia Polytechnic Institute and State University, (2000) 1–192.

[3] Soong, T. T., Dargush, G. F., Passive Energy Dissipation and Active Control, Structural Engineering Handbook, (1999).

[4] Chandra, R., Masand, M., Nandi, S. K., Tripathi, C. P., Pall, R., Pall, A.. Friction-Dampers for Seismic Control of La Gardenia Towers, 12th World Conference on Earthquake Engineering, (2000) 1–8.

[5] Dorothy. R., Investigation of Tuned Liquid Dampers Under Large Amplitude Excitation, 124(4) (1998) 405–413.

[6] Sgobba, S., Marano, G. C., Optimum design of linear tuned mass dampers for structures with nonlinear behaviour, Mech. Syst. Signal Process., 24(6) (2010) 1739–1755.

[7] Pall, A. S., Marsh, C., Response of friction damped braced frames, J. Struct. Div., ASCE, 108 (1982) 1313–1323.

[8] Pall, A. S., Pall, R. T., Performance-Based Design Using Pall Friction Dampers - an Economical Design Solution, 13th World Conference on Earthquake Engineering, (2004).

[9] Wu, B., Zhang, J., Williams, M. S., Ou, J., Hysteretic Behavior of Improved Pall-typed Frictional Dampers, Eng. Struct., 27 (2005) 1258–1267.

[10] Reinhorn, C. L. A.M., Use of Supplemental Damping Devices for Seismic Strengthening of Lightly Reinforced Concrete Frames, NY, (1995).

[11] Marko, J., Influence of Damping Systems on Building Structures Subject to Seismic Effects, Queensland University of Technology, (2006).

[12] Eduardo, L., Seismic Interstory Drift Demands in Steel Friction Damped Braced Buildings Seismic Interstory Drift Demands in Steel Friction, Texas A&M University, 2009.

[13] Sasani, M., Popov, E. P., Experimental and Analitical Studies on the Seismic Behaviour of Lightweight Concrete Panels with Friction Energy Dissipators, (1997).

[14] Petkovski, M., Waldron, P., Optimum Friction Forces for Passive Control of the Seismic Response of Multi-storey Buildings, In: 40 years of European Earthquake Engineering SE40EEE, (2003).

[15] Petkovski, M., Friction Based Passive Control of the Seismic Response of Multi-Storey Reinforced Concrete Frames, University of Sheffield, (2001).

[16] Powell, G. H., DRAIN-2DX Element description and user guide, (1993) 1–35.

Neural network modelling of naturally ventilated spaces

J. S. Sykes, E. A. Hathway, P. Rockett
University of Sheffield
josh.sykes@sheffield.ac.uk, a.hathway@sheffield.ac.uk, p.rockett@sheffield.ac.uk

Primary Supervisor: Dr **A. Hathway** – e-mail: a.hathway@sheffield.ac.uk
Secondary Supervisor: Dr **P. Rockett** – e-mail: p.rockett@sheffield.ac.uk

ABSTRACT. During operation, buildings consume a large amount of energy, in developed countries around 40% of total final energy use. A major challenge is to reduce the amount of energy used while still providing a comfortable environment for building occupants. The use of passive techniques, such as natural ventilation, is promoted in certain climates to provide low energy cooling and ventilation. However, controlling natural ventilation in an effective manner to maintain occupant comfort can be a difficult task, particularly during warm periods. One area which has been identified as having the potential for reducing energy consumption while maintaining occupant comfort is the use of more advanced control techniques and a move towards "intelligent" buildings. A technique which has been much explored in recent years for application in mechanically ventilated buildings is Model Predictive Control (MPC). The essential component of an MPC strategy is the predictive model of the building's thermal dynamics. In this paper a data driven, neural network approach to system modelling is taken to model internal temperatures. Building data from a recently built naturally ventilated school and an office building are used to train multilayer perceptron neural network models and the resulting models performance are examined. The models developed were found to have good prediction capabilities over reasonable prediction horizons; however the effect of the control input was not captured.

KEYWORDS. MPC; Neural Networks; Ventilation.

INTRODUCTION

Energy costs, climate change, mounting political and social pressure are examples of some of the drivers for the increasing attempts to reduce energy consumption. Buildings account for around 40% of total final energy consumption in developed countries [1], and in European countries around 76% of the energy consumed by buildings is used for comfort control, i.e. heating, ventilation and air conditioning (HVAC) [2]. Reducing the amount of energy required by HVAC systems can be approached in a number of ways, for example increasing airtightness, better insulation, increasing appliance efficiency, passive ventilation techniques etc. In addition to energy concerns, there has been a growing awareness of the impact of indoor environmental quality (IEQ) upon occupants' wellbeing [3]. IEQ refers to the quality of a building's environment in relation to the health and wellbeing of those who occupy the space [4]. There is a number of factors which contribute to IEQ including air quality, temperature, lighting, contaminants etc.

Natural ventilation is the process of supplying and removing air to an indoor space without the aid of mechanical systems. Natural Ventilation is driven by pressure differences caused by wind or temperature differences. As natural ventilation is

affected by a number of factors such as external temperature, wind speed, wind direction, internal temperatures etc. It can be hard to predict the consequence of opening a window or vent. This makes control of naturally ventilated spaces more challenging than mechanically ventilated or air-conditioned spaces [5]. In this paper we propose a control method which has the potential to reduce energy consumption and optimise occupant comfort in naturally ventilated spaces. Model Predictive Control (MPC) is a control method which originated in process industries [6]. MPC utilises a system model to optimise future outputs based upon possible inputs over a finite receding horizon. At each time step a minimisation of some objective function is carried out in order to determine the optimal control signals over a finite horizon. At each iteration only the first step of the control strategy is then implemented. The control horizon is then shifted one step forward and the process is repeated [6].

PROBLEM DESCRIPTION

Modelling Strategy

In order for MPC to be successful, an accurate model of the system is required. The model should be as simple as possible and have good prediction characteristics over the control horizon [7, 8]. There are two main approaches to system modelling which can be taken when applying MPC to HVAC systems. One approach is the use of first-principles models, typically multizone-network models such as EnergyPlus, TRNSYS etc. These models are based upon our knowledge of the physical processes taking place within the building.

The alternative to the first-principles models is the use of black-box data-driven models. These models are typically less computationally intensive to use and once a suitable workflow has been devised, relatively simple to create. Empirical models have the advantage of modelling the processes which are actually happening within a space without including the assumptions which are necessary with a first-principles model. For example, with a simulation tool, such as EnergyPlus, it is possible to include detailed occupancy and activity schedules but it will be hard to fully capture the stochastic manner in which occupants interact with the building and their effect upon the building's thermal environment. Additionally, as we move towards "smart buildings", there are an increasing amount of data available about how buildings are actually running, which have the potential to drive a data-driven approach.

In this paper, we take a data driven approach using multilayer perceptron (MLP) neural networks to predict zone temperatures in naturally ventilated spaces. Neural Networks have been used in previous studies for control of HVAC systems [9] and automated window blinds [10]. The Neural Network Toolbox within MATLAB was used to train and test the networks using the workflow shown in Fig. 1.
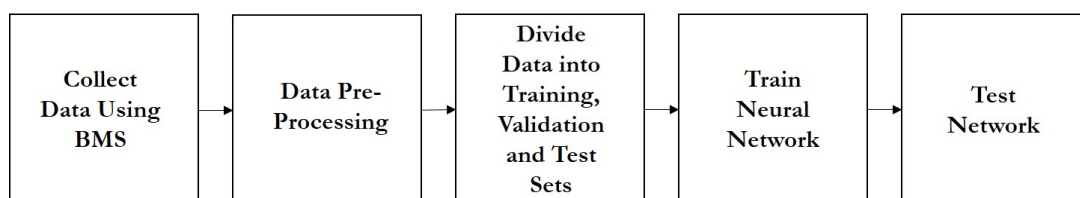

Figure 1: Workflow for Neural Network modelling strategy.

Building Descriptions

The essential component in the empirical approach taken in this paper are the building data with which a model can be trained. Obtaining suitable data was found to be challenging. There were two main problems experienced when attempting to obtain real building data for this project. Firstly, convincing building managers, owners and other stakeholders to give access to data which could highlight poor performance in their buildings. In cases where this initial hurdle was overcome there are practical difficulties related to gathering building data. While most building management systems (BMS) are capable of recording data they are not typically designed to store large amounts of data over prolonged periods. It was additionally quite common that there were gaps in the data and erroneous sensor readings. This had implications for the amount of pre-processing which was required before the models could be trained.

The building data used in this project comes from two sources: a recently-built school, and an office building in the north of England. Both are naturally ventilated and have a range of single-sided, cross and buoyancy ventilated spaces. The windows are a combination of occupant-controlled manual windows, and automated windows and vents. Data are available for the opening position of the automated windows in both buildings, however due to the lack of sensors on the

manual occupant-operated windows, there is no information available. For this reason the manual windows can be treated as a disturbance which will affect the models. A total of eight zones within each building were studied. Data was collected for a full year and sampled at 10 minute intervals.

SYSTEM IDENTIFICATION

The first stage in system identification is pre-processing. In this study there were two distinct phases in the pre-processing. First was the processing carried out to extract and clean the data recorded by the BMS. This included linearly interpolating to replace missing data points and removing any obvious outliers. Outlier removal was carried out by calculating the standard score for each variable and then removing all values which fell outside of an expected range. The second phase of pre-processing was carried out to improve network training. This included normalization to prevent saturation of the sigmoid transfer units in the network and to adjust the magnitudes of the various inputs. Typically, it is beneficial for network performance if inputs to have a similar magnitude unless there is intentional weighting being applied.

Following the initial data cleaning and pre-processing, the data were divided into three subsets using three contiguous blocks of the original data set. The first set is used for model training, the second for validation (this set is used to prevent over-fitting) and the final set is withheld from model training and used as an unseen test set.

For the control of natural ventilation we want to model internal zone temperatures based upon the previous zone temperatures and the effect of other inputs shown in Tab. 1. These are all inputs that were collected using the building management system. This is essentially a non-linear autoregressive with exogenous external inputs (NARX) model. The defining equation for a NARX model is given by:

$$y(t) = f\left(y(t-1), y(t-2),..., y(t-n_y), \mathrm{u}(t-1), \mathrm{u}(t-2),..., \mathrm{u}(t-n_u) \right) \tag{1}$$

where the target (y) is a function of previous values of itself and of other inputs (u). In a NARX network the target can be considered to be an estimation of the true output of the system being modelled. During training of the network, the true output is available. This allows a series-parallel or "open-loop" architecture to be used (as shown on the left in Fig. 2). There are two key advantages to a series-parallel architecture. Firstly, the input to the network is more accurate and hence the resulting network tends to have a greater performance. Secondly, the network has a purely feedforward architecture allowing static backpropagation to be used in training [11]. This means that training is less computationally intensive.

Series-Parallel Architecture   **Parallel Architecture**
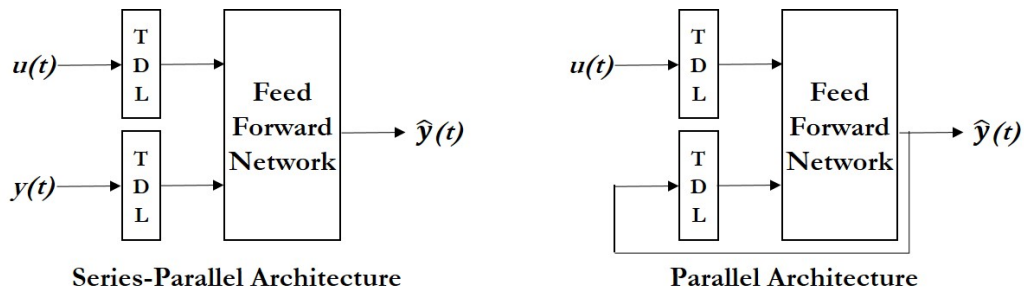
Figure 2: Feed forward network architectures for NARX networks. On the left is the series-parallel or open-loop configuration ideal for one-step-ahead prediction and on the right is the parallel or closed loop configuration. In a parallel architecture model predictions are fed back into the network through a tapped delay line (TDL) allowing for multi-step-ahead predictions. Adapted from Beale et al. [11].

However by training the network using a series-parallel form, training has been optimized for one-step-ahead prediction. While this is a good starting point, multi-step-ahead prediction is required for MPC. One possible approach is to train the network using a series-parallel architecture and then close the loop to create a parallel architecture. However as the training has been carried-out using actual values of the network output and then tested with predicted values, performance is not optimal. However, it is undesirable to train the network in a closed-loop form from the outset due to the time and computational effort required. In order to achieve an accurate final model without a large computation requirement, the workflow shown in Fig. 3 was utilised. By carrying-out the training initially using a series-parallel architecture and then

using the resulting weights and biases as the starting point for the closed loop network, a 46% reduction in training time was observed (based upon a study using data from 5 zones and repeating training 10 times per zone).

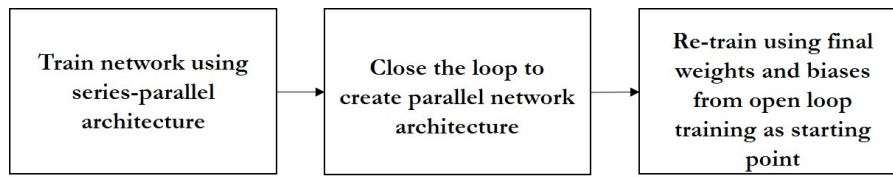| Train network using series-parallel architecture | → | Close the loop to create parallel network architecture | → | Re-train using final weights and biases from open loop training as starting point |

Figure 3: Optimal workflow for training neural network models.

The structure of neural network models is in some respects determined by the system being modelled (number of input and output nodes), however it is up to the user to determine the optimum number of hidden layers and hidden nodes contained within them. Although there is some guidance in the literature, this can often be contradictory [12, 13, 14]. Therefore, determining the optimum structure for a particular problem and set of data is largely a process of trial and error. In addition to training networks with a range of architectures a number of combinations of inputs and input delays were also tested.

Variable	Type	Notes
Zone Temperature	Output	
Outdoor Temperature	Input	
Wind Speed	Input	
Wind Direction	Input	
Window Opening Percentage	Input	Only available for automatic windows
Heating Status	Input	Boolean value showing heating on/off state

Table 1: Variables used for system identification.

RESULTS

The models developed in this paper were found to perform well upon the unseen test data. The first models generated were for one-step-ahead prediction. As can be seen in Fig. 4 the one-step-ahead models almost perfectly track the target temperatures, typical mean squared errors (MSE) were in the range of 0.1-0.2. This performance is good, however the prediction horizon of 10mins is very short. When the models were trained in a parallel architecture the multi-step-ahead prediction capabilities were also found to be good; as can be seen in Fig. 4. When predicting the zone temperature at twenty-steps-ahead (n=20, i.e. 200mins in the future) the typical MSE was approximately 0.5. MSE was used as an initial metric by which to judge model performance as it was the performance function minimised during network training [11]. Other measures of model performance such as the standard deviation and mean absolute percentage error were also calculated and used for model selection [15]. However, for analyzing results a visual comparison of model outputs and targets was found to give the best insight into how the model performed. It can be seen in Fig. 4 that the model outputs closely track the target temperatures for the unseen test data. Upon closer inspection it was observed that model performance was poorer during unoccupied periods. Fig. 4 shows test data for a week in one of the zones within the school. It can be seen that at the end of the week and during the nights the predictions stray further from the target temperatures. This seems to indicate that occupancy can have a high impact upon the models. Potentially this could be overcome by creating two models for each zone; one for occupied periods and one for unoccupied. This is likely to improve accuracy, however the degree to which this would impact upon the control performance may not justify the extra complexity.

While the initial results appeared very promising, upon closer inspection there were clear inadequacies with the models developed. During training of the models a number of different combinations of the inputs shown in Tab. 1 were used. The addition of further information to the model did not improve performance over a purely autoregressive model based

upon previous values of zone temperature. This suggests that previous values for zone temperature are a good enough predictor without additional weather data. While being able to discard weather inputs could have potential benefits in reducing model complexity, it is essential that the influence of control inputs (window opening positions) are captured by the model. It was confirmed by carrying out a sensitivity analysis that the window position had no impact upon the output temperature. This would prevent the models from being suitable for an MPC application.
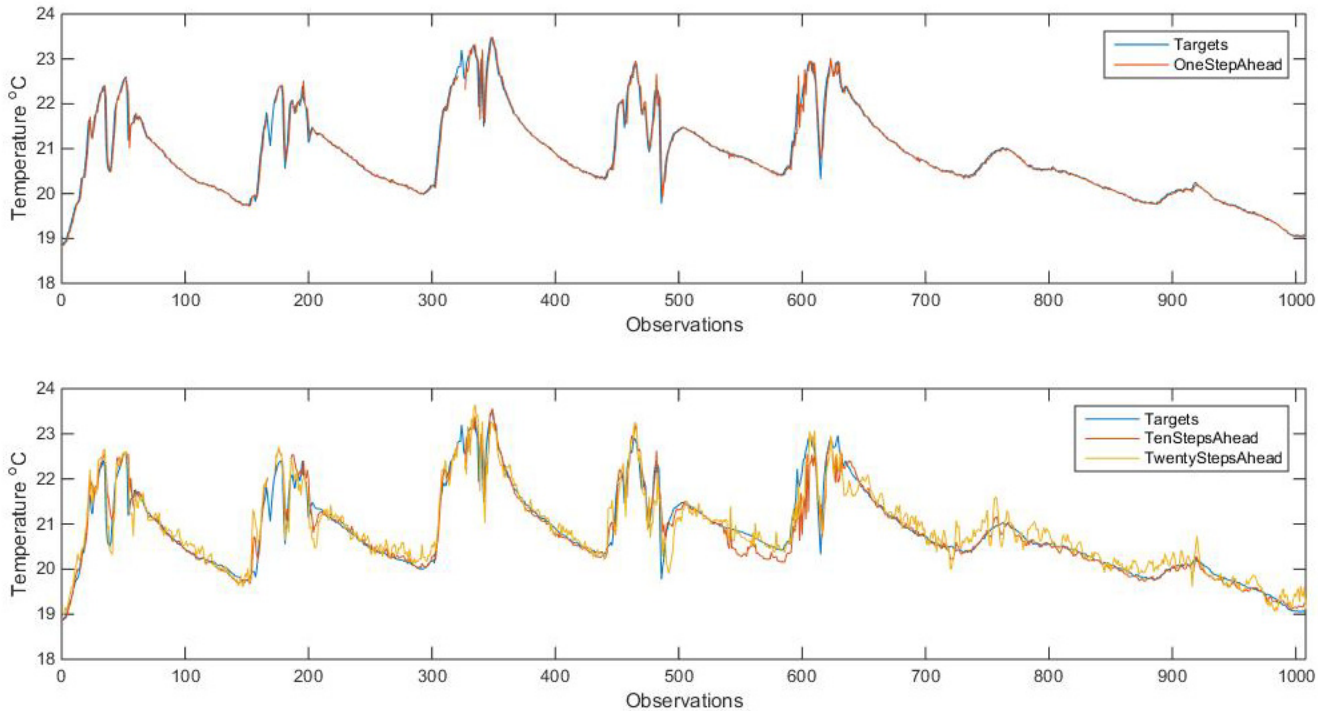

Figure 4: Comparison of model output temperatures and observed temperature for unseen test data. The top graph shows the one-step-ahead performance and the bottom shows n=10 and n=20 (10 minute time step).

DISCUSSION

The models developed were able to predict internal temperature over a reasonable prediction horizon. However the effect of the window opening percentage was not captured by the models. This would make them unsuitable for the MPC approach to ventilation control proposed in this paper. The inability of the models to capture the effect of the control input is most likely due to lack of sufficient input excitation and is one of the common drawbacks when using data driven models [7, 8]. Buildings are typically operated within a tight range and the input is not persistently excited [16, 17]. This can lead to models which while providing reasonable prediction capability, are lacking in essential physical relationships. The inability of the models generated to capture the effect of the control input is most likely due to this issue. This could potentially be overcome by carrying out an identification experiment where more complex signals are used to excite the system over a greater range.

Carrying out-an identification experiment on a real building during occupation has the potential to cause disruption. In some cases it would be possible to carry out identification experiments during periods of low occupancy such as those experienced in schools and other academic institutions [17] or in the case of new buildings it could take place during commissioning.

CONCLUSIONS

Although the models developed are unsuitable for the purpose of MPC, there are other potential uses for accurate data driven models such as those developed in this project. Previous studies have used empirical models for fault diagnosis [18, 19] and to investigate potential overheating [20]. There could also be potential to incorporate a

future temperature prediction within a traditional rule based control strategy.

Further Work

In order to determine if the inability of the developed models to capture the effect of window opening is caused by lack of input excitation, an identification experiment is proposed. Due to the high costs involved this will not be performed in a real building or experimental mock up but through the use of computer generated data using a multizone building simulation tool such as EnergyPlus. This experiment is not proposed to increase the accuracy of the model predictions but to generate a model which better represents the physical processes occurring and is suitable for the MPC application.

ACKNOWLEDGEMENTS

REFERENCES

[1] Perez-Lombard, L., Ortiz, J., Pout, C., A review on buildings energy consumption information, Energy and Buildings, 40(3) (2008) 394-398.

[2] International Energy Agency, Energy Efficiency Requirements in Building Codes, Energy Efficiency Policies for New Buildings (2008).

[3] Anon, ASHRAE Handbook – Fundamentals, Chapter 11: Indoor Environmental Health, ASHRAE, Atlanta (2013).

[4] http://www.cdc.gov/niosh/topics/indoorenv/, (2015).

[5] Thomas, R., Environmental Design: An Introduction for Architects and Engineers, third ed., Taylor and Francis, New York (2006).

[6] Comacho, E. F., Bordons, C., Model Predictive Control, second ed., Springer, London (2007).

[7] [7] Shook, D., Mohtadi, C., Shah, S., A control-relevant identification strategy for GPC, IEEE Transactions on Automatic Control, Volume 37 Issue 7 (2002) 975-980.

[8] Lauri, D., Salcedo, J., Garcia-Nieto, S., Martinez, M., Model predictive control relevant identification: multiple input multiple output against multiple input single output, Control Theory & Applications, IET, 4(9) (2010) 1756-1766.

[9] Kusaik, A., Xu, G., Modeling and optimization of HVAC systems using a dynamic neural network, 8th World Energy System Conference, 42 (2012) 241-250.

[10] Chen, Y., Li, H., Chen, X., Venetian blind control system based on fuzzy neural network for indoor daylighting, Computer and Electrical Engineering, 2nd International Conference on, 2 (2009) 269-273.

[11] Beale, M. H., Hagan, M. T., Demuth, H. B., Neural Network Toolbox User's Guide, Mathworks (2014).

[12] Blum, A., Neural Networks in C++, Wiley (1992).

[13] Swingler, K., Applying Neural Networks: A Practical Guide, Academic Press, London (1996).

[14] Boger, Z., Guterman, H., Knowledge extraction from artificial neural network models, Man and Cybernetics Conference, Orlando Florida (1997).

[15] Kusaik, A., Tang, F., Xu, G., Multi-objective optimization of HVAC system with an evolutionary computation algorithm, Energy, 36 (2011) 2440-2449.

[16] Privara, S., Vana, Z., Gyalistra, D, Cigler, J., Sagersching, C., Morari, M, Ferkl, L., Modelling and identification of a large multi-zone office building, Control Applications (CCA), 2011 IEEE International Conference on, (2011) 55-60.

[17] Cigler, J., Privara, S., Subspace identification and model predictive control for buildings, Control Automation Robotics & Vision (ICARCV), 2010 11th International Conference on, (2010) 750-755.

[18] Lee, W. L., House, J. M., Kyong, N. H., Subsystem level fault diagnosis of a building's air-handling unit using general regression neural networks, Applied Energy, 77(2) (2004) 153-170.

[19] Katipamula, S., Brambley, M. R., Methods for fault detection, diagnosis, and prognostics for building systems – a review, part I, HVAC&R Research, 11(1) (2005) 3-25.

[20] Iddon, C. R., Mills, T. C., Girirdharan, R., Lomas, K. J., The influence of hospital ward design on resilience to heat waves: An Exploration using distributed lag models, Energy and Buildings, 86 (2015) 573-588.

Experimental investigation of the buckling interaction between individual components of a built-up steel stub column

F. Meza, J. Becque
The University of Sheffield
fjmezaortiz1@sheffield.ac.uk, j.becque@sheffield.ac.uk

Primary Supervisor:	Dr **J. Becque** – e-mail: j.becque@sheffield.ac.uk
Secondary Supervisor:	Prof. **J.B. Davison** – e-mail: j.davison@sheffield.ac.uk

ABSTRACT. This paper describes an experimental program carried out at The University of Sheffield on built-up cold-formed steel columns. The columns were constructed from individual channels and plate sections with nominal thicknesses of 1.4 mm and 2.5 mm, respectively. The columns were tested with three different connector spacing and were designed to exclude global instabilities. All the test specimens were compressed between fixed supports and each test was repeated. Therefore, a total of six built-up columns were tested. Coupon tests were extracted from the corners and the flat portions of the sections in order to determine their material properties, and detailed measurements of the out-of-plane imperfections of each specimen were recorded with a laser sensor. These data will be used for the future development of an FE model.

The experiment revealed a pronounced extent of restraint and interaction between the individual components of the section while buckling, with the connector spacing having a significant effect on the observed buckling modes and, to a lesser extent, on the cross-sectional capacity.

KEYWORDS. Built-up column; Experiment; Cold-formed steel; Stability; Buckling; Imperfection measurements.

INTRODUCTION

Cold-formed steel sections have traditionally been used as secondary steelwork in industrial buildings. Common examples are purlins and cladding rails made of lipped channels, sigma or zed sections with thicknesses ranging between 0.5 mm to 6 mm [1]. Depending on the quantity, length and complexity of the sections, they can be produced by roll forming or brake pressing.

The reduced wall thickness of cold-formed steel sections allows for an efficient use of the material, leading to a high strength-to-weight ratio. In addition, due to their shape, they can usually be stacked efficiently, reducing the cost of transportation. They are also easily handled, with single members and sub-frames being easily put in place by operators [1]. All these reasons are leading to an increasing use of cold-formed steel, not just as secondary members, but also as primary load-bearing members, driving the cold-formed steel industry to produce section that can provide larger spans and resist higher loads. Examples of this trend are low-rise multi-storey buildings and cold-formed steel portal frames constructed entirely out of cold-formed steel [2, 3].

On the other hand, the reduced wall thickness of cold-formed steel sections makes them more prone to being affected by cross-sectional instabilities such as local or distortional buckling. These cross-sectional instabilities originate in addition to the global instabilities that are common to the traditionally used hot-rolled sections. Moreover, due to the nature of the fabrication process, the cross sectional shapes that can be cold-formed are commonly mono-symmetric or point-symmetric, with double symmetry difficult to obtain. A logical solution to increase the load carrying capacity of cold-formed steel

members is joining two or more sections together to form a built-up section. Thus, double-symmetric cross sections can be easily constructed with the currently available single shapes. Also, a wider range of cross sectional shapes can be tailored to meet specific requirements.

Despite the benefits built-up sections can offer, the current design codes [4, 5] do not provide any tailored guidance for the design of built-up members. Designing a built-up section requires a careful consideration of various factors, such as the type of connector used, the spacing between the connectors, the degree to which the individual components work as one cross-section, and the occurrence of individual as well as coupled instabilities. A number of experimental tests have previously been carried out on built-up sections. In [6, 7] a series of compressive tests were carried out on closed and open built-up columns made up of two sigma sections connected with screws. The typical I-section made up of two lipped channels connected back-to-back has been extensively studied in [8, 9] where the components were connected using sheet metal screws, and in [10–12] where the channels were welded together. It should be noted that all these tests have only accounted for built-up sections made of two identical components, in which both components buckle at the same time.

The experimental program described in this paper consisted of concentric compression tests on six built-up stub columns. The specimens were assembled by bolting four individual sections together. The program sought to investigate the various instabilities in the members, the interaction between the cross-sectional components during buckling and the effect of the connector spacing on the buckling modes and ultimate capacity of the columns. All columns were tested between fixed supports and were sufficiently short to exclude global instabilities. The specimens were tested with three different connector spacings, and each test was repeated.

SPECIMEN GEOMETRY AND LABELLING

The test specimens were constructed by connecting the flanges of the channels to two plate sections using M6 bolts, as illustrated in Fig. 1. The sections were manufactured from pre-galvanized steel plates with a nominal yield stress of 450 MPa and with a 0.04 mm Z275 zinc coating applied to both sides. All columns had a length of 1100 mm and were designed with 2, 3 or 5 equally spaced connectors. The channels had a nominal thickness of 1.4 mm and the plate sections had a nominal thickness of 2.5 mm. The label used in this paper to refer to each of the built-up specimens consists of the letters 'SC' followed by a hyphen and the number of rows of intermediate connectors in the built-up column. As each test was repeated, the letters 'a' and 'b' indicate whether the specimen was the first or the second of twin columns tested.
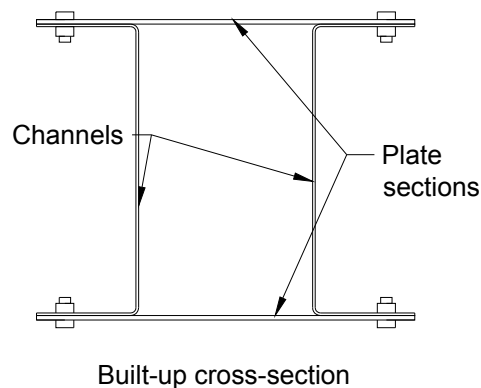

Figure 1: Built-up cross-sectional geometry and individual components

The cross-sectional dimensions of all the individual sections were measured prior to assembling them, and their relative position within the built-up section was recorded. All reported measurements relate to outside dimensions. Tab. 1 lists the measured dimensions and the relative position of the components with reference to Fig. 1, as well as the spacing between connectors of each test specimen.

Both ends of each built-up specimen were manually filed to correct the slight relative difference in length of the individual components. Endplates with dimensions of 250x300 mm² and a thickness of 20 mm were attached at both ends of the column using a 2-part thixotropic epoxy resin. In addition to hand filing the ends, this provided a second means to ensure a uniform introduction of the load into all components.

Column	Channel			Plate		Connector spacing (mm)
	location	Web (mm)	Flange (mm)	location	Width (mm)	
SC-2a	Left	154.00	53.92	Top	199.73	333
	Right	154.23	53.62	Bottom	199.83	
SC-2b	Left	154.13	53.85	Top	199.83	333
	Right	154.13	53.45	Bottom	199.67	
SC-3a	Left	154.23	53.75	Top	199.53	250
	Right	154.10	53.67	Bottom	199.27	
SC-3b	Left	154.17	53.43	Top	199.43	250
	Right	154.10	53.75	Bottom	200.40	
SC-5a	Left	154.17	53.60	Top	200.10	167
	Right	154.17	53.63	Bottom	199.47	
SC-5b	Left	154.13	53.37	Top	198.93	167
	Right	154.23	53.62	Bottom	198.73	
Average		154.15	53.64		199.58	-
St. Dev.		0.07	0.17		0.46	-

Table 1: Measured dimensions of the components and connector spacing

MATERIAL PROPERTIES

Six tensile coupon tests were used to determine the material properties of the individual sections. The coupons were taken in the longitudinal direction, and from spare sections belonging to the same batch as those used in the test. Two identical coupons were taken along the centre line of the plate. In the case of the channels, two identical coupons were extracted from the centre line of the web and other two from the web-flange junction, as the material properties of the channels were expected to differ significantly in the folded region of the cross-section due to plastic deformations induced during the forming process. All coupons were tested following the specification given in the European standard [13]. Tab. 2 lists the average values of the Young's modulus (E), the 0.2% stress ($\sigma_{0.2\%}$) and the tensile strength (σ_u) obtained from each pair of twin coupons.

Type	Section	E (GPa)	$\sigma_{0.2\%}$ (MPa)	σ_u (MPa)
Flat	Plate	195	437	519
Flat	Channel	207	609	704
Corner	Channel	235	609	730

Table 2: Coupon test results.

IMPERFECTION MEASUREMENTS

The stability of thin-walled steel members may be significantly affected by the presence of imperfections. In stub columns, these imperfections are mainly present in the form of out-of-plane deviations of the plates of the sections. Therefore, the imperfections of the most slender plate of each individual component were recorded before testing. Measurements were performed after the built-up columns were assembled into their final configurations, as joining the single sections together might somewhat modify their geometric imperfections.

The equipment used to carry out the measurements consisted of a steel table, a traverse system powered by electric motors and a laser displacement sensor. The arrangement used is shown in Fig. 2. The flat table was guaranteed to be grade 3, providing a flat surface with a deviation from flatness of less than 0.06 mm [14].
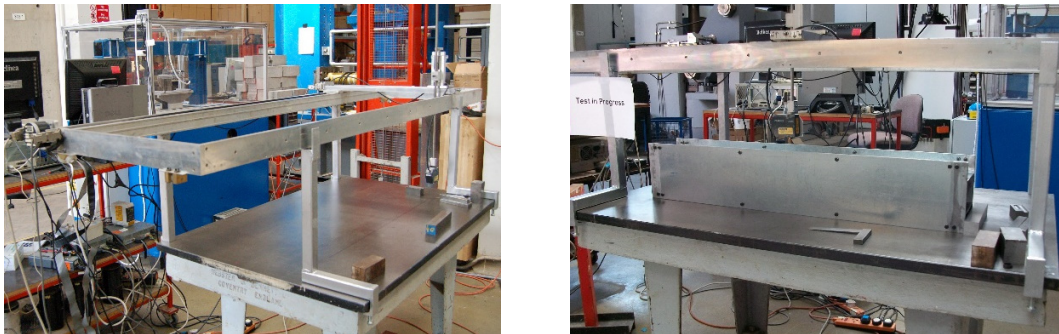

Figure 2: Set-up used to measure the out-of-plane imperfections

To measure the imperfections of the specimens, the traverse system was used to move the laser head along three longitudinal lines on each face of the built-up column at a pre-determined constant speed. Measurements of the imperfections of the plates as well as of the web of the channels were recorded. To correct for the out-of-straightness of the guiding bars along which the laser head was moved, measurements of the table itself were also recorded. Therefore, the accuracy of the measurements was determined by the flatness of the table and can be expected to be of the order of 0.06 mm.

TEST SET-UP

All the specimens were tested between fixed end supports. The specimens were tested in an EHS universal testing machine with a capacity of 1000 kN. The tests were carried out by applying a strain rate of $1.7 \times 10-6$ /s, resulting in a displacement rate of 0.11 mm/min.
To capture the axial deformations of the specimens and the out-of-plane deformations of their components, 14 LVDTs were employed. Twelve of them were used to measure the out-of-plane deformations of the component sections, and they were placed at mid-distance between connectors. They consisted of two sets of six LVDTs placed at different heights along the column in an attempt to capture the localization of the deformations. The other two LVDTs were placed on each side of the column to measure its axial deformation. The set-up is shown in Fig. 3.

TEST RESULTS

Deformed shape and critical stresses

All test specimens failed due to the interaction of a global-type flexural buckling of the individual plate sections between connectors and local buckling of the channels, as shown in Fig. 3. The presence of the webs of the channels forced the plate sections to buckle mainly outward in all the columns. This may have been accompanied by some slippage in the connectors, as the plates were observed to remain mostly straight in the fields adjacent to the field where the plates buckled outward. The plate sections buckled with a half-wave length larger than half the distance between connectors in all the columns. This implies that the flanges of the channels, at the location of the connectors, had to undergo a certain rotation and translation in order to accommodate the buckling pattern of the plate sections. It is noted that the 'natural' half-wave length of the individual (and unrestrained) channels is 170 mm. By comparing this half-wave length with the actual half-wave length of the channels, observed in the test specimens, it can be concluded that the channels tried to buckle with a half-wave length as close as possible to the 'natural' one, insofar as this buckling configuration was permitted by the buckling pattern of the other components. In the case of columns SC-2 and SC-3, the spacing between connectors was large enough (333 mm and 250 mm respectively) for the channels to accommodate two buckling half-wave between connectors (Fig. 3a and Fig. 3b, respectively). However, in columns SC-5, the spacing between connectors was much shorter and the channels buckled with only one half-wave length between connectors. In these columns, the buckling half-wave length of

the plates coincided with the buckling half-wave length of the channels, which resulted in the flanges of the channels buckling outward in almost perfect sympathy with the plate sections (Fig. 3c).

The critical buckling stresses, of each of the individual sections, obtained from the test were compared with the theoretical values, which were calculated assuming no interaction between the components and using the buckling half-wave lengths observed during the test. In the case of the channels, this buckling half-wave length corresponded to either the distance between connectors or half the distance between connectors. In the case of the plate sections, the buckling half-wave length could not be determined accurately from the experiment and therefore, a lower and upper bound were calculated theoretically, corresponding to assuming that the plate sections buckled with one or two half-waves in between the connectors, respectively. The experimental buckling stresses of the various components were estimated from the LVDT readings. Initially, up to the point of first buckling, the load was transmitted uniformly to all the components. In columns SC-2, the plate sections buckled in a flexural mode before buckling of the channel sections occurred, while simultaneous buckling of the channels and plate sections was observed in columns SC-3 and SC-5. As the plate sections buckled in a flexural mode, it is reasonably assumed that they had no post-buckling capacity and therefore, any further increase of load past the point of buckling was entirely resisted by the channels.
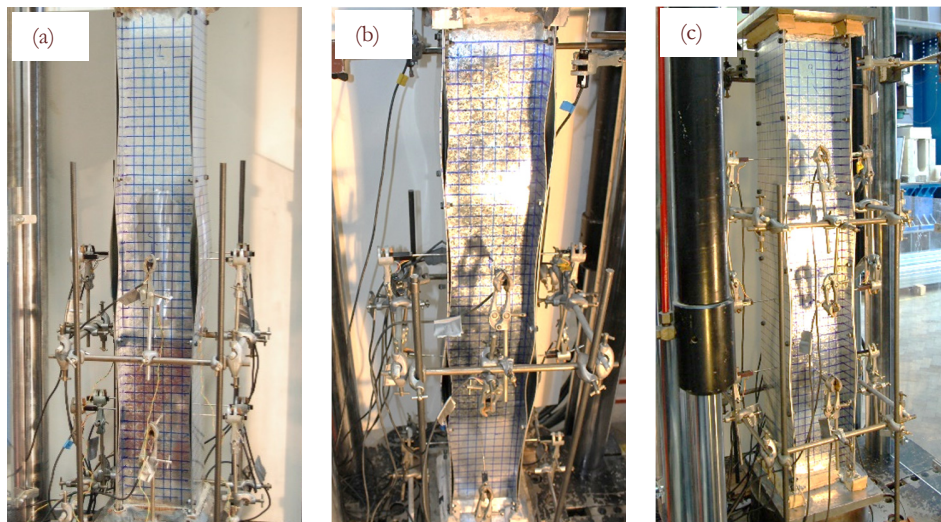

Figure 3: Deformed shape in columns a) SC-2a, b) SC-3a and c) SC-5a.

Column	Theoretical buckling stress (MPa)			Buckling stress from test (MPa)	
	Channel	Plate		Channel	Plate
		Lower	Upper		
SC-2a	63	10	41	52	41
SC-2b	63	10	41	52	41
SC-3a	67	18	73	58	57
SC-3b	67	18	73	56	56
SC-5a	63	41	165	81	81
SC-5b	63	41	165	83	83

Table 3: Theoretical and experimental buckling stresses of the individual sections.

Tab. 3 shows that for columns SC-2 (columns were the plate sections buckled before the channels) the stresses at which the plate sections buckled coincided with the theoretical upper bound, indicating that the channel in its pre-buckled state provided a significant amount of restraint to the plates. The channels, on the other hand, buckled at a stress somewhat lower than the theoretically predicted value. In columns SC-3, simultaneous buckling of the channel and plate sections was experimentally observed. The experimentally derived buckling stress of the channels is slightly lower than the theoretically

predicted value, while the measured buckling stress in the plates is about 23% lower than the theoretical upper bound. In columns SC-5, the channels and the plates sections were also seen to buckle at the same time in the experiment. In this case, the plate sections buckled at a stress well below the theoretical upper bound value, while the channels clearly benefitted from the extra restraint provided by the plate sections and buckled at a stress well above the theoretical value. This is indicative of the fact that the plate and channel sections strongly interacted with each other in these columns and buckled sympathetically with roughly the same half-wave length.

Ultimate load

The ultimate loads obtained for all test specimens, as well as the average values for each set of twin columns, are shown in Tab. 4. Twin columns showed a maximum difference in ultimate load of 8.97% (obtained for columns SC-2). The tests also showed an increase of the ultimate load of the built-up columns as the spacing between connectors was reduced. More specifically, halving the spacing between connectors from 333 mm to 167 mm produced an increase in the ultimate load of 10.81%.

Column	Ultimate load (kN)	Avg. Ultimate load (kN)
SC-2a	183.97	
SC-2b	168.17	176.07
SC-3a	183.01	
SC-3b	175.86	179.44
SC-5a	201.72	
SC-5b	188.50	195.11

Table 4: Ultimate load for test specimens

CONCLUSIONS

Compression tests on six built-up cold-formed stub columns between fixed supports were performed. The investigation included determining the material properties of the specimens through coupons tests, and measuring the specimen out-of-plane imperfections.
The experimental program showed that the different components in the built-up column mutually restrain each other while buckling. This restraint was reflected in the deformed shape which each individual component displayed and in the difference between their theoretical unrestrained and experimentally observed buckling stresses. The restraini was observed to be highly dependent on the connector spacing. However, the impact of the connector spacing on the ultimate capacity of the cross-section was observed to be of lesser importance in these particular cross-sections..

REFERENCES

[1] Dubina, D., Ungureanu, V., Landolfo, R., Design of Cold-Formed Steel Structures – Eurocode 3: Design of Steel Structures Part 1-3; Design of Cold-Formed Steel Structures, ECCS – European Convention for Constructional Steelwork, first ed, Timisoara Romania, (2012).

[2] Li, Y., Shen, Z., Yao, X., Ma, R., Liu, F., Experimental investigation and design method research on low-rise cold-formed thin-walled steel framing buildings, J. Struct. Eng., 139 (2013) 818-836.

[3] Dundu, M., Design approach of cold-formed steel portal frames, Int. J. Steel Structures, 11 (2011) 259-273.

[4] BS EN 1993-1-3, Eurocode 3 – Design of steel structures – Part 1-3: General rules –Supplementary rules for cold-formed members and sheeting, British Standard Institution, (2006).

[5] AISI, Commentary on North American Specification for the design of Cold-Formed Steel Structural Members, (2007).

[6] Young, B,. Chen, J., Design of cold-formed steel built-up closed sections with intermediate stiffeners, J. Struct. Eng., 134 (2008) 727-737.

[7] Zhang, J,H., Young, B., Compression tests of cold-formed steel I-shaped open sections with edge and web stiffeners, Thin-Walled Structures, 52 (2012) 1-11.

[8] Lau, H.H., Ting, T.C.H., An investigation of the compressive strength of cold-formed steel built-up I sections, Proceedings of the Sixth International Conference on Advances in Steel Structures. ICASS'09, (2009) 441-449.

[9] Stone, T.A., LaBoube, R.A., Behavior of cold-formed steel built-up I-sections, Thin-Walled Structures, 43 (2005) 1805-1817.

[10] Whittle, J., Ramseyer, C., Buckling capacities of axially loaded, cold-formed, built-up C-channels, Thin-Walled Structures, 47 (2009) 190-201.

[11] Piyawat, K., Ramseyer, C., Kang, T.H., Development of an axial load capacity equation for doubly symmetric built-up cold-formed sections, J. Struct. Eng. 139 (2013) 1-13.

[12] Weng, C.C., Pekoz, T., compression tests of cold-formed steel columns, Ninth International Specialty Conference on Cold-Formed Steel Structures, (1988).

[13] BS EN ISO 6892-1, Metallic materials – Tensile testing Part 1: Method of test at ambient temperature, British Standard Institution, (2009).

[14] BS 817, Specification for surface plates, British Standard Institution, (2008).